UNIVERSITÀ
DEGLI STUDI
FIRENZE

DOTTORATO DI RICERCA IN ENERGETICA E TECNOLOGIE INDUSTRIALI E AMBIENTALI INNOVATIVE

CICLO XXXIII
COORDINATORE Prof. Giampaolo Manfrida

CFD Strategy for the Aerodynamic and Aeromechanic Design and Verification of Axial Compressor for Gas Turbine Engines

Settore scientifico disciplinare ING-IND/08

PhD Candidate
Eng. Corrado Burberi

Tutor
Prof. Andrea Arnone

Co-ordinatore
Prof. Giampaolo Manfrida

Firenze 2017/2020

UNIVERSITÀ
DEGLI STUDI
FIRENZE

DOTTORATO DI RICERCA IN ENERGETICA E TECNOLOGIE INDUSTRIALI E AMBIENTALI INNOVATIVE

CICLO XXXIII

COORDINATORE Prof. Giampaolo Manfrida

CFD Strategy for the Aerodynamic and Aeromechanic Design and Verification of Axial Compressor for Gas Turbine Engines

Settore scientifico disciplinare ING-IND/08

PhD Candidate
Eng. Corrado Burberi
Department og Industrial Engineering, Univerity of Florence

Tutor
Prof. Andrea Arnone
Department of Industrial Engineering, Univerity of Florence

Co-Tutor
Prof. Michele Marconcini
Department og Industrial Engineering, Univerity of Florence

Co-Tutor
Dr. Eng. Alberto Scotti del Greco
Gas Turbine Aerodynamics Manager, Baker Hughes

Firenze 2017/2020

A Chiara e Libero

«*I vecchi già lo sanno il perché e anche gli alberghi tristi, che il troppo è per poco, e non basta ancora, ed è una volta sola. E ancora proteggi la grazia del mio cuore*»

Vinicio Capossela

Contents

Abstract iv

Nomenclature vi

1 Introduction 1

1.1 Thesis objectives and outline 10

2 Fundamentals of axial compressor 13

2.1 Aerodynamic design 13

2.1.1 Compressor stage 14

2.1.1.1 Velocity triangles 14

2.1.1.2 Blade loading and diffusion factor 16

2.1.1.3 Thermodynamics and losses 21

2.1.2 Characteristic curve 28

2.1.3 Stage matching 34

2.2 Aeromechanical design 37

2.2.1 Blade row modeshape and mode families 38

2.2.2 Flutter 42

2.2.2.1 Aerodynamic damping estimation 43

2.2.3 Forced response 45

2.2.3.1 Campbell and Interference diagram 47

2.2.3.2 Forcing circumferential decomposition 52

2.2.3.2.1 Test on reduced domain 58

2.2.3.3 Improved use of the Interference diagram 63

2.2.3.4 Modal work 66

2.2.3.5 HCF life assessment 68

3 Numerical methods 71
3.1 CFD design strategy 71
3.2 TRAF code 75
3.3 Discretization 81
3.4 Aerodynamics computational setup 84
3.4.1 Steady analysis 85
3.4.2 Unsteady analysis 86
3.5 Aerodamping computational setup 88
4 Aerodynamic validation 93
4.1 Test rig 93
4.2 Measured and predicted stage-by-stage speedlines 95
4.2.1 The spanwise profiles and their impact on stage matching 100
4.2.2 Non-dimensional speedlines 105
4.2.3 The impact of unsteadiness 108
4.2.4 Single stage steady approach for design 114
5 Aeromechanical validation 121
5.1 Overall compressor results 121
5.2 Forced responce test case 124
5.3 R7 FEM model 127
5.4 R7 results 129
5.4.1 Classical crossing results 132
5.4.2 Tyler-Sofrin crossing 133
5.4.3 Reduced domain 135

5.5 Clocking effect on aerodynamic forcing 137
5.5.1 Numerical test case 138
5.5.2 Clocking results 141
5.5.2.1 Impact on performance 141
5.5.2.2 Case A - R11 clocking 143
5.5.2.2.1 Nominal speed (100%) 144
5.5.2.2.2 Off-design speed (90%) 149
5.5.2.3 Case B - R11 clocking 153
5.5.2.4 Case C - R11 clocking 160
5.5.2.5 Case B - S11 clocking 164
6 Conclusion 170

Abstract

The axial compressor is one of the most critical modules in a gas turbine engine for propulsion, power generation and mechanical drive. The adverse pressure gradient in the flow stream direction is the main issue that makes the aerodynamic design of this component extremely complex and challenging. Moreover, the high stage count, the low blade aspect ratio and the clearance regions lead to intense secondary flows. Axial compressors evolved through large number of experimental tests to overcome the difficulties that numerical methods, from classical throughflow to Reynolds-averaged Navier-Stokes (RANS) CFD, encounter when predicting speed-lines and stall margin.

This thesis proposes a CFD strategy for the aerodynamic and aeromechanic design and verification of axial compressor for gas turbine engines characterized by a combined use of steady and unsteady numerical simulations in order to significantly increase the design accuracy keeping industrial design time requirements. In particular, the stall margin prediction and the forced response assessment are the key aspects of this procedure. An unsteady analysis of the whole compressor is capable of predicting a stall margin comparable to the measured one and, at the same time, of evaluating the complete blade forcing spectrum on each row from the unsteady solution. The spatial decomposition theory, explained in this thesis, applied to the overall unsteady aerodynamic forcing allows to separate the contributions of the different nodal diameters. The proposed improved use of the Interference Diagram is able to detect additional possible resonances in the operating range of turbomachines trying to avoid many

unexpected vibrations during compressor validation tests. The activities have been carried out in the framework of the collaboration between the university research group led by Professor Arnone of the University of Florence and the industrial partner Baker Hughes.

The first part of the thesis presents a general description of the axial compressor design parameters. In this part, the spatial decomposition theory and the improved use of the Interference Diagram are presented in detail. The second part of the work focuses on the description of the proposed CFD strategy. This is followed by the description of the CFD tool (TRAF) used for all the numerical simulations together with the computational setup of each type of analysis. The third part concentrates on the validation of the numerical design strategy by the comparison with a large set of measurement coming from an experimental campaign on an 11-stage industrial axial compressor, dealing first with the aerodynamic results and then with the aeromechanical ones. Finally, an extensive numerical study aimed to evaluate the impact of rotor-rotor and stator-stator clocking on the forced response results taking advantage of the spatial decomposition theory is reported.

The numerical design strategy has been validated and it can be considered ready and suitable for axial compressor design.

Nomenclature

A	Cross-sectional area
ADP	Aero Design Point
BPF	Blade Passing Frequency
c	speed of sound
C	Velocity
C_{ax}	Axial chord
C_{ex}	Blade row exit velocity
C_m	Through flow velocity
CFD	Computational fluid dynamics
CFL	Courant-Friedrichs-Lewy number
c_p	Specific heat at constant pressure
DES	Detached Eddy Simulation
DFT	Discrete Fourier transform
E	Total internal specific energy
E_{kin}	Kinetic energy
EO	Engine Order
F	Flow function
F	Forcing
F_{red}	Reduced frequency
FEM	Finite Element Method
HDGT	Heavy duty gas turbine
h	Enthalpy
H	Total enthalpy
i	Incidence angle
ICASE	Institute for Computer Applications in Science and Engineering
ICOMP	Institute for Computational Mechanics in Propulsion

IGV	Inlet guide vanes
k	Thermal conductivity/turbulent kinetic energy
k	Harmonic or scattering index
L	Aerodynamic work
LES	Large eddy simulation
$\dot{m}$	Mass-flow
m	Circumferential order
M	Mach number
M	Momentum variation
n	Normal vector
N	Blade Number
N	Newton
NASA	National Aeronautics and Space Administration
Nc	Corrected speed
ND	Nodal Diameter
NRBC	Non-reflecting boundary conditions
OGV	Outlet guide vanes
p	Pressure
Pr	Prandtl number
PR	Pressure ratio
PS	Pressure side
Q	Residual/Amplification factor
R	Rotor
RANS	Reynolds-averaged Navier-Stokes
RBC	Reflecting boundary conditions
s	Row pitch/Entropy
S	Stator
SS	Suction Side
T	Temperature
t	Time
U	Rotational speed
u	Peripheral velocity

URANS	Unsteady Reynolds-averaged Navier-Stokes
v	Relative velocity/y velocity component
w	z velocity component
W	Relative velocity
W	Specific work
Wc	Corrected mass flow rate
x	Axial coordinate
y^+	Non dimensional wall distance

Greek

α	Absolute pitch flow angle
β	Relative pitch flow angle
γ	Specific heats ratio/ Absolute yaw flow angle
δ	Deviation angle/Displacement
η	Efficiency
θ	Circumferential direction/clocking position
μ	Dynamic viscosity
ξ	Stagger angle/loss coefficient/damping
ρ	Density
σ	Row solidity
ϕ	Flow coefficient
χ	Metal angle
ψ	Work coefficient
ν	Vibration frequency
ω	angular frequency/Turbulence frequency
Ω	Rotational speed

Subscripts

0	Stagnation quantity
aero	Aerodynamic
c	Convective
d	Diffusive

is/ss	Isentropic transformation
m	modal
p	Polytropic/profile
R	Radial direction/rotor
ref	Reference quantity
rel	Relative quantity
S	Stator
t	Turbulent
tt	Total-to-total

1 Introduction

This thesis deals with the design of axial compressors. Without discounting the importance of other components, the axial compressor is one of the most critical module in a gas turbine engine for propulsion, power generation and mechanical drive as it dictates the operability range and requires demanding aerodynamic and aeromechanical design efforts. This first chapter focuses on an in-depth study of the literature concerning the aerodynamics and aeromechanics design of axial compressors.

Axial compressors evolved through large number of tests to overcome the difficulties that numerical methods, from mean-line and throughflow approaches to Reynolds-averaged Navier-Stokes (RANS) CFD, may encounter in predicting speedlines and, most importantly, the stall point. Smith [1] described the evolution of axial compressor design and technology. In the paper, Smith described the fundamentals of the design process, from the selection of the vector diagram to the expected performance. In their milestone paper, Koch and Smith [2] were among the first to investigate how losses evolve in axial compressors. Their theoretical approach identified four classes of losses: profile, end-wall, shock, and part-span shroud that are the basis of well-established performance correlations that are still essential in early design phases. Wadia and Beacher [3] described the evolution from a simple mean-line approach to a more sophisticated throughflow method supplemented by 2D and 3D Euler analyses to assess the performance impact of three-dimensional profile features. While concentrating on the design point, they demonstrated a good match with test data.

The throughflow approach is still used in the design community, as witnessed by Righi et al. [4] who describe an evolution of this method for the successful prediction of the reverse flow and rotating stall characteristic of a multistage axial compressor. Wadia et al. [5] studied front rotors sweep at design and off design conditions. They once again concentrated on three-dimensional features impact on the front stages by testing several designs and comparing with viscous CFD predictions. Ng and Epstein [6] were among the first to investigate how the unsteadiness may affect the evolution of losses by performing unsteady measurements in an axial compressor test rig. They were able to discern between core flow and wake mixing contribution to the overall loss of adiabatic efficiency. While loss analyses and advanced three-dimensional design mostly focused on design point performance, Koch [7] used a low-speed research compressor facility (see Wisler [8]) to determine the stall margin of axial compressor blading by the introduction of a corrected pressure rise coefficient that mimics the fundamental diffuser studies of Sovran and Klomp [9]. Koch demonstrated a good correlation between the blading diffusion length and the static pressure rise coefficient at stall. The dedicated low-speed test facility described by Wisler [8] allowed to complete a fairly large number of tests required to validate the approach.

Correlations are still the primary design and verification tool for axial compressors due to well-known and documented difficulties to directly predict performance and stall point. Cornelius et al. [10] used a commercial code to perform steady and unsteady simulations of a 6-stage compressor for which a detailed experimental data base was available. The unsteady simulations showed an improved fit with measurements with respect to the steady results, both in terms of overall speed-line and spanwise inter-row profiles, although some mismatch still existed. More

recently Cozzi et al. [11] completed steady and unsteady simulations of a 15-stage axial compressor. The results showed how the predicted stage loading changes in the time-resolved simulation, that resulted in different predicted efficiencies and pressure ratio. Importantly, they also observed how the unsteady simulations predicted a smoother stagnation temperature profile at exit as compared with steady results, although they were unable to determine the accuracy of their simulation due to the lack of measurements. The insufficient spanwise mixing of stagnation temperature is a known weakness of the steady multistage CFD, and it was addressed by Adkins and Smith [12] who exploited measured temperature profiles to develop a specific spanwise mixing model to be used in through-flow calculations. With their CFD simulations of a five-stage compressor using a two-equation turbulence model, Cozzi et al. [13] demonstrated that the lack of spanwise mixing is partly responsible for the inaccurate multistage predictions. They also observed that such inaccuracy is caused by the so-called mixing-plane approach used to filter out the unsteadiness and streamwise vorticity associated with the stator-rotor interaction. The mixing plane approach was ultimately responsible for a stage mismatch that deviates from the measured performance, while unsteady simulations predicted smoother profiles, in line with what observed in [12]. On top of its impact on performance and operability, Hewkin-Smith et al. [14] showed how unsteadiness affects the tip leakage flow and the stall mechanism. In [14] a very detailed aerodynamic analysis was instrumental to understand how unsteady flow in the tip clearance region may limit compressor operability. Li et al. [15] performed a detailed experimental campaign on a single and a three-stage axial compressor to investigate the propagation of unsteady tip clearance flows. Their analysis suggests way to stabilize the tip flow and delay spike-type

stall with appropriate flow injections. Taylor and Miller [16] used CFD to investigate how 3D geometrical features may strengthen the endwall flow and mitigate stall risk. In their analysis the authors had to switch to unsteady CFD to improve the accuracy of the near stall predictions. More recently, Leggett et al. [17] used highly resolved LES to investigate the loss production mechanism in an axial compressor profile. The analysis revealed a different loss breakdown predicted by URANS and LES, and it also suggested that incoming wakes may delay stall at midspan. Other authors, [18], [19], used very computationally demanding multi-stage LES and DES to investigate stall mechanism and propagation of separated regions. The motivation to switch from a more conventional URANS to scale resolved simulations was that in presence of large unsteady separated regions two-equation models may not be accurate, as also discussed by Laskowski et al. [20]. Still, as witnessed by [21], URANS may be reasonably accurate up to the stall point, as also witnessed by the detailed experimental and URANS investigation of a single stage axial compressor described by Wang et al. [22]. Their analysis reveals how URANS was capable of predicting the measured speed-line, while RANS predicted an early rotating instability not present in the data. Wang et al. [23] used URANS to capture the unsteady tip clearance flow in a transonic compressor rotor. The unsteady flow pattern revealed by URANS showed a multi-passage structure that impacted the growth of local instabilities and local stall. In an attempt to reduce the computational effort, Gourdain et al. [24] described the successful application of a quasi-3D URANS to the prediction of a single stage compressor stall mechanism and determine the fundamental destabilizing mechanism. Sun et al. [25] describes a valid alternative to URANS, which is based on an extension of the harmonic balance method to high off-design conditions (e.g.

near stall condition) and capable of handling massive flow reversal. This method compares well with measured surge cycles. Another interesting alternative to the simple mixing plane approach are the deterministic stresses that could, in principle, be adequate to address the effects of the deterministic unsteadiness on the time-averaged flowfield. However, its application has shown how an actual improvement over the mixing-plane method for both speedlines and blade loading predictions is possible only when the deterministic stresses are extracted from a precursor URANS simulations (see Stollenwerk and Kuegeler [26]). It is undeniable that scale-resolved simulations have an accuracy advantage with respect to RANS and URANS. Nevertheless, despite the increase in computational power and improvement in algorithm efficiency, LES and DES as well, still require a computational effort inconceivable for design applications.

Compressor design must also include the accurate verification of the aeromechanical risks. The so-called Campbell diagram, originally explained and introduced in 1924, verifies if natural and aerodynamic forcing frequencies overlap, with a potential destructive result, while the Goodman diagram, introduced in 1899, addresses the companion fatigue risk evaluation. The Campbell diagram alone is not enough to make design decisions as it can indicate more potential problems than issues that actually exist. There exists a vast literature that addresses the complex physic behind the unsteady fluid-structure interaction in gas turbine engines. Among these, Barankiewicz and Hathaway [27] investigated the fundamental aerodynamic stator-rotor interaction by using a four-stage low speed axial compressor. The authors observed that stator-stator with unequal blade count may produce azimuthal distortions that do require to survey across more than one blade row pitch, as confirmed by the

circumferential changes of the pressure coefficient amplitudes that may interact with the corresponding nodal diameters. The authors also scrutinized clocking effects on performance, observing little impact on efficiency. Vahdati et al. [28] employed full 3D unsteady multi-passage and multirow CFD coupled with structural elements to investigate forced response in a 2.5 stage axial compressor. They revealed the shortcomings of calculations performed on reduced number of rows and, among their most important results, the authors discovered that the excitation of a rotor blade associated to low-engine orders, that appear when two consecutive stator or rotor rows have a small count difference, may produce high response. Obviously, this is not a risk in presence of clockable consecutive stators. Still, clocking is a double-edge knife as it may offer limited performance improvement opportunities, but it may also result in a performance shortfall in case the selected relative position is incorrect. Terstegen et al. [29] measured the aerodynamic excitation in a 2.5 stage axial compressor. The authors described the physics of Tyler-Sofrin [30] modes and supported their conclusions with CFD simulations with both a linearized and harmonic balance version solver by Frey et al. [31] capable of an excellent match with data also in terms of vibrational stresses and pressure amplitudes and spectra. The measurements revealed spinning azimuthal modes as well as the scattering of these modes due to the interactions with blade rows. The authors also mention that manufacturing deviations cause systematic discrepancies in the measured pressure amplitudes and concluded that acoustic multirow interaction is essential for the accurate prediction of the compressor vibrational stresses. In part II of the same paper, Sanders et al. [32] investigated the impact of CFD modeling choices, like turbulence and transition model and grid convergence, on the predictions. It turned out that the single row linearized approach was unable to get the right answer in terms of

response when acoustic modes were a major source of excitation, while the non-linear harmonic method guaranteed a better match with data. The computations also revealed the need of a reliable transition model to guarantee a good match with data. The complex aero-mechanical coupling across the operability range of axial compressors have been investigated by Baumgartner et al. [33] who analysed the high vibrations in the first rotor of a high-pressure compressor. The vibrations were caused by a rotating flow instability, similar to a rotating stall induced pressure fluctuations, the frequency of which did not match with harmonics of the rotor speed. The comparison between the pressure/velocity fluctuations and the blade vibration confirmed the excitation source. This paper reveals that different source of excitation may arise while moving across the compressor speedline, and this needs to be addressed by extending the aeromechanical check to off-design conditions. More recently Figaschewsky et al. [34] used a 4.5-stage research axial compressor to investigate the effect of Tyler–Sofrin modes on forced vibration responses. The analysis was supported by unsteady CFD, although with a simplified quasi-2D approach of the full circumference. Both measurements and simulations suggest that mistuning effects may be amplified by the presence of Tyler-Sofrin modes. The paper tackles two operating conditions with different sets of variable stator vanes (VSV) and investigates how damping and modal shapes affect the structural coupling concluding that the computational model provides a fair representation of the physics.

As already mentioned, stator/rotor count and clocking are another fundamental aspect of the compressor design because they affect both performance and operability of axial compressors as described in the open literature. Gundy-Burlet and Dorney [35] were among the first to use two-dimensional CFD to

investigate the impact of airfoil count and clocking on axial compressor. The authors observed not only changes in efficiency, but also on excitation amplitudes in a 2.5 stage axial compressor. They measured the highest loss with clocking positions that caused the largest unsteadiness. Dorney et al. [36] applied a quasi-3D CFD approach to the clocking analysis of a 1.5 stage high-speed compressor. They observed a complex interaction driven by the concurrent impact of wakes and pressure waves worth 0.5 points of efficiency at maximum. Layachi and Bolcs [37] used a single stage low aspect-ratio compressor rig with IGVs to test different combinations of IGV to stator clocking and rotor-stator spacing. The combination of clocking and spacing was worth 3% stage efficiency, as already suggested by Smith [1]. The best clocking position appeared to change along the span, as already observed in [38] and [39] for low-pressure-turbines. Cizmas and Dorney [40], in contrast with what reported in [1], concluded that large pressure fluctuation amplitudes on airfoils were associated with best efficiency, due to a positive resonance between two consecutive stator rows that energizes boundary layers. Arnone et al. [38] showed that while low unsteadiness levels are usually associated with better turbine performance, high leading edge unsteadiness corresponds to the best clocking position for every radius. Huang et al. [41] discussed how clocking affects wakes and pressure driven potential effects and how this alters the performance in a low speed research compressor with cylindrical flow path. They investigated eight clocking positions worth 1 point of efficiency maximum, while their predictions suggested only half of the measured delta, the majority of which attributed to stator clocking. Walker et al. [42] used a 1.5 stage compressor to determine the beneficial IGV-to-stator clocking effect on operability by delaying separation. Chen et al. [43] investigated how a 3D stator can shape the wake to optimize its impact on the corresponding

downstream stator, revealing a concurrent clocking and wake shape effect worth up to 2% when the upstream stator wake impinges the leading edge of the downstream one. A combined experimental and numerical investigation on a four-stage low-speed axial compressor with equal stator count [44], [45] , revealed large variations of the pressure fluctuation with different clocking positions. Like in [40], the authors observed the best performance when pressure fluctuations were high, although the absolute effect was small. The stator wake position controlled by clocking did not correlate with the unsteady loading of both stator and rotor, and losses of the rotor embedded between two corresponding stators were controlled by the superimposition of the upstream stator wakes with the downstream stator potential effect. Manwaring and Wisler [46] were among the first to shift focus on gust response to address aeromechanic issues. While not investigating clocking, the authors reviewed various methods to predict unsteady loads and compared with data coming from a low-speed research compressor similar to the one adopted in [44] and [45], and with a companion turbine facility. They focused on a 1.5 stage low aspect ratio axial compressor, and on a high aspect ratio two-stage axial turbine. The authors investigated a range of operating points and concluded that unsteady forcing changes significantly with running conditions. Their analysis showed that simple linear methods, capable of resolving both vortex and potential effects, could predict pressure and suctions side pressure fluctuations in terms of amplitude and phase. Hsu and Wo [47] investigated clocking effects on aerodynamic forcing in a two-stage axial compressor rig. The authors analyzed two rotor clocking positions that had a large impact on the unsteady forcing and forced response of the in-between stator. The differences were both in terms of amplitude and chordwise distribution of the unsteady load. The authors, who

claimed this was the first time that clocking was demonstrated to be capable of reducing unsteady load, suggested it might be possible to find a clocking position in which distinct sources of disturbance cancel out by appropriately selecting their phase shift. They investigated axial spacing to confirm that smaller spacing is good for performance due to the wake diffusion (see [48]), but dangerous for aeromechanics. Along the same line, Salontay et al. [49] performed a joint experimental and numerical investigation on the response of a rotor blade embedded in clocked stator rows. The authors concentrated on both design point and high loading and concluded that it was not possible to find a stator-stator clocking capable of minimizing the rotor excitation valid for multiple operating points. They also concluded that the position of stator 1 wake with respect to stator 2 leading edge had little impact on the response of the embedded rotor. Rather, what mattered was the phase between the incoming vorticity generated by stator 1 and the downstream potential forcing due to pressure waves. When the maximum incoming vorticity and the minimum downstream potential gust interacted with the rotor at the same time the measurements showed the minimum rotor response.

This introduction clearly highlights many aerodynamic and aeromechanic issues that make the design of axial compressors still very challenging. The development of reliable numerical tools capable of providing an accurate prediction of the overall compressor performance is a topic of a great interest to both the scientific community and the industry.

1.1 Thesis objectives and outline

This thesis proposes a CFD strategy for the aerodynamic and aeromechanic design and verification of axial compressor for gas turbine engines characterized by a combined use of steady and

unsteady simulations in order to significantly increase the design accuracy keeping industrial design time requirements. This procedure not only improves the prediction of aerodynamic performance, also in terms of stall margin, but also introduces new important aspects concerning the forced response assessment (circumferential decomposition theory). An improved use of the Interference Diagram capable of detecting additional possible resonances in the operating range of turbomachines is presented. It takes advantage of the spatial decomposition theory applied to the overall unsteady aerodynamic forcing which allows to separate the contributions at different nodal diameters.

Chapter 2 provides a general introduction on the main design aspects regarding the aerodynamic and aeromechanical issues of axial compressors. The spatial decomposition theory and the improved used of the interference diagram will be described in detail. Moreover, the CFD strategy, including the computational setups, is reported in chapter 3. Finally, the aerodynamic and aeromechanic validation of the numerical design procedure is discussed in the two final chapters. The availability of a reliable data set of a 11-stage axial compressor that incorporates high-performance features suited for both propulsion and heavy-duty gas turbine was instrumental to assess the complete procedure. Chapter 4 shows the validation in terms of accuracy of CFD steady, unsteady, and single stage results, in the challenging speedline prediction. The aeromechanic results based on the spatial decomposition of the unsteady forcing is reported in chapter 5 and the methodology is fully validated by the good agreement between experimental data and numerical predictions of the forced response. The final part focuses on the impact of clocking on forced response assessment taking into consideration also the additional exciting forcing evaluated through the spatial decomposition.

2 Fundamentals of axial compressor

The axial compressor is one of the most critical component in a gas turbine engine as, while it contributes to the overall engine efficiency, it dictates the operability range and requires demanding aerodynamics and aeromechanics design efforts. The adverse pressure gradient in the flow stream direction is the main issue that makes the aerodynamic design of this component complex and challenging. The aeromechanical design efforts are aimed at preventing vibration issues that may compromise blade integrity thus leading to premature failures.

In the first part of this chapter the main aerodynamic design aspects of an axial compressor will be discussed in detail. The second part will cover aeromechanical design, with particular focus to the new themes and approaches introduced during this work.

2.1 Aerodynamic design

The first step of the aerodynamic design usually consists in the "meanline analysis". This approach studies the 2D flow development through the machine on the meanline radius. This performance evaluation method does not consider three-dimensional effects that are fundamental for an accurate prediction. The following step is the throughflow approach that is a quasi-three-dimensional CFD method that solves axi-symmetric flow in the meridional plane. Besides traditional methodologies based on streamline curvature or stream function methods, Computational Fluid Dynamics (CFD)-based throughflow approaches are becoming more and more popular in modern turbomachinery design systems [50] [51] [52]. They are important for the prelim-

inary design and often they can be used for re-assessing the machine performance after relevant design change. The Computational Fluid Dynamics is currently the focus of axial compressor stage design. Regarding axial compressors that are characterized by huge computational domain, the most widely used approach is the RANS computations.

After this brief introduction on the method commonly used for compressor design, the following chapters will illustrate the main aerodynamic parameters of axial compressors.

2.1.1 Compressor stage

The stage of a compressor is composed by a rotor blade row followed by a stator blade row. The blades of the rotor row are mounted on the rotor drum while the stator blades are fixed to the machine outer casing.

2.1.1.1 Velocity triangles

The interactions between stators (fixed rows) and rotors (rotating rows) through the axial compressor generate a flow field that is characterized by strong unsteadiness. Despite this, during the preliminary design, the unsteadiness can initially be ignored, and the flow can be simply analysed using the frame of reference fixed with the investigated row. A rotating frame of reference (relative frame) is used to describe the flow through rotor row, while a stationary frame of reference (absolute frame) is used to describe the flow through stator row. Given the change of reference system, it is useful to introduce the concept of a velocity triangle. The inlet absolute velocity C_1 at the rotor inlet section can be obtained adding vectorially the inlet relative velocity W_1 and the blade rotational speed $U = R\Omega$ (see Figure 2.1). The velocity W_1 is the one that determines the incidence on the rotor row. The angle β_1, called inlet relative flow angle, corresponds

to the angle between the relative flow velocity and the axial flow direction, while the angle α_1, called inlet absolute flow angle, corresponds to the angle between the absolute velocity and the axial flow direction. Throughout this thesis the velocity and the angle in the absolute frame of reference will be denoted by C and α respectively, and in the relative frame of reference by W and β. The inlet absolute flow velocity of an industrial axial compressor stage is, in general, not axial, even for the first stage, due to the presence of Inlet Guide Vanes (IGV) which provide a pre-rotation of the fluid. The relative flow is subjected to diffusion across the rotor, which means that the magnitude is decreased, and the direction is deflected to β_2. The rotational speed is considered to be constant across one stage since no relevant radial changes of the channel are present through the meridional direction, so as a result the absolute velocity increases from C_1 to C_2. The stator works the opposite. The absolute velocity is decreased to obtain a pressure increase. The absolute flow is deflected towards the axis to an outlet absolute flow angle α_3, thus achieving at the same time an increase in tangential component of the relative velocity at the inlet of next rotor. The compressor velocity triangles are characterized by having a high relative tangential component at the inlet of the rotor row and a low absolute tangential component at the outlet of the stator row.

Except for the first stages, the multi-stage axial compressor is designed using the repeating stage concept where the absolute velocity at the inlet and at the outlet section presents the same magnitude and the same direction. In each compressor stage, both the relative velocity in the rotor and the absolute velocity in the stator decrease. The flow deflection, defined as the difference between the outlet and the inlet flow angle across a blade row, is limited due to adverse pressure gradient on the blade

surface that generates an increase of the boundary layer thickness and can bring to separations and consequently an early stall of the blade row.

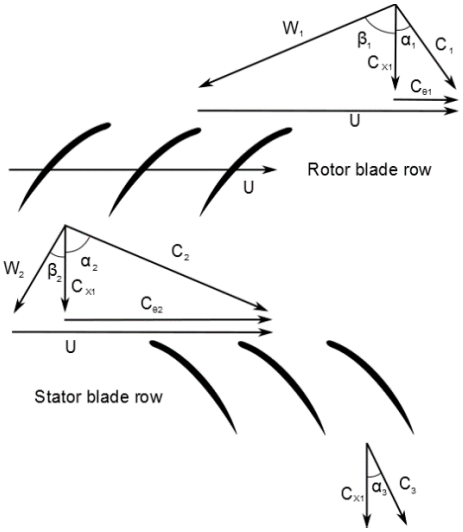

Figure 2.1- Velocity triangles of axial compressor stage

2.1.1.2 Blade loading and diffusion factor

The blade load is given by the integral distribution of the pressure on the blade profile. The shear stresses usually are considered negligible. The pressure distribution is strictly related to the camber line shape and the thickness distribution. The blade loading is usually assessed using two design criteria introduced by Lieblein: the diffusion factor DF [53] and the diffusion ratio DR [54]. The two parameters are defined as follow:

$$DF = \left[1 - \frac{c_2}{c_1}\right] + \frac{\Delta c_\vartheta}{2\sigma c_1} \qquad (1)$$

$$DR = \frac{c_{max}}{c_2} \tag{2}$$

where the σ is the compressor row solidity, defined as the ratio between the chord and pitch, while Δc_ϑ is the tangential velocity variation across the row. The row solidity σ is a non-dimensional parameter that represents how well the flow is guided by the blades. The diffusion factor, see equation (1), can be divided in two contributes:

1. $\left[1 - \frac{c_2}{c_1}\right]$; the first contribute is related to the mean deceleration of the flow
2. $\frac{\Delta c_\vartheta}{2\sigma c_1}$; the second contribute is related to the flow turning

The diffusion factor highlights the fact that to obtain high stage loads (decreasing c_2 and/or increasing Δc_ϑ), the row solidity must be increased to maintain an acceptable level of diffusion and avoid flow separation. The increment of σ can be obtained by increasing the blade chord or the row blade number and it produces consequently higher profile losses. Lieblein [54] showed that the loss in a blade row increases rapidly as the flow starts to separate, and this occurs when the diffusion factor exceeds about 0.6. Typically, a well-designed blade with moderate loading will operate with a diffusion factor around 0.45. The diffusion ratio adds another parameter to check and this is the maximum isentropic velocity on the blade suction side. Figure 2.2 shows a typical isentropic velocity distribution on a compressor blade profile and it represents the blade loading. It is useful to understand graphically the two design criteria.

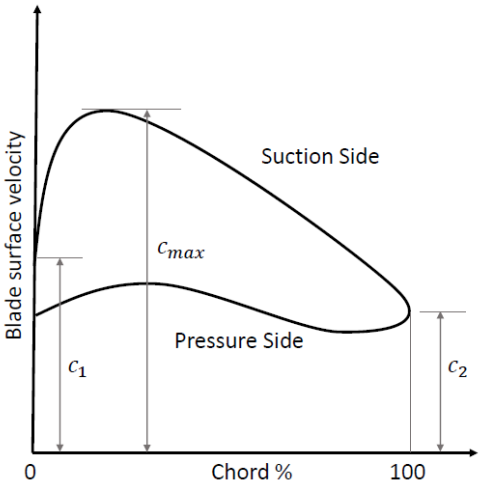

Figure 2.2 - Isentropic velocity distribution on the blade surface

The diffusion ratio is important because it is directly related to the amount of diffusion on the suction surface, and it is not taken into consideration in the diffusion factor. Indeed, once c_2 is fixed, the pressure gradient depends on the amplitude and the position of the maximum value of isentropic velocity. Another criterion to consider during the design of compressor blade loading is the De Haller's rule [55]. It is based on the De Haller number, c_2/c_1, that is a measure of the overall amount of diffusion through a compressor blade row. This parameter is still often used to limit the maximum pressure rise across a compressor blade row. De Haller's rule recommends that:

$$\frac{c_2}{c_1} \geq 0.72 \tag{3}$$

The blade load determines the momentum variation across a blade row. As already mentioned before, the momentum variation is linked to the flow velocity and the flow angle variation. The change in flow velocity depends on the pressure raise between the inlet and the outlet section but it is limited by the diffusion process on the blade surface that can bring to elevated losses and stall issue. The change in flow angle velocity depends on the inlet and the outlet flow angle. The relative outlet flow angle varies with operating conditions change but in a reduced range. As a result, the load on the blade is defined substantially by the inlet flow angle, in particular by the incidence, defined as the difference between the inlet flow angle α_1 and the blade inlet angle χ_1 (see Figure 2.3):

$$i = \alpha_1 - \chi_1 \tag{4}$$

Figure 2.3 reports the main geometrical parameters of a compressor blade profile including incidence and the blade inlet angle

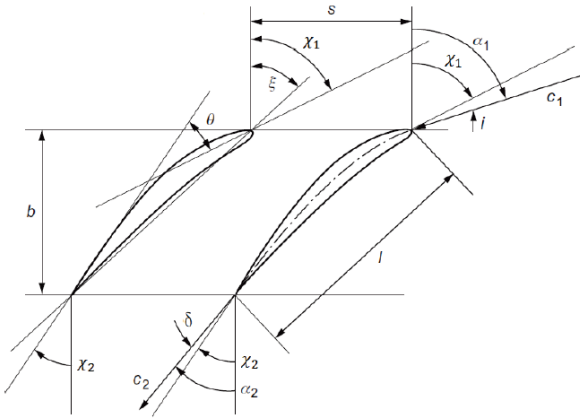

Figure 2.3 – Geometrical parameters of axial compressor blade profile

Given that the velocity variation is limited by separation issues, it follows that the incidence, which is the parameter related to the angle variation, has a very significant effect on the blade load. At the design condition, the incidence is slightly positive but very close to zero. The inlet flow angle and the inlet blade angle are almost the same. The flow deflection is due to the camber of the blade. During the off-design conditions the incidence can change significantly. If the incidence is positive, the flow at the leading edge impinges on the pressure side. The flow on the suction surface present a prompt acceleration around the leading edge. The velocity peak on the pressure side increases and it produces a very high local diffusion close to the front of the blade. The boundary layer development is affected by the increment of the pressure gradient and can lead, in addition to higher blade losses, to a separation or even to stall. Regarding the flow deflection, the contribution of the incidence is added to that of the camber and leads to a flow deflection increment [56]. If the incidence is negative, the flow at the leading edge impinges on the suction side. The flow on the suction surface present a lower acceleration around the leading edge and the velocity peak decreases. The diffusion is lower but also the flow deflection decreases and consequently the blade loading. The negative incidence leads to an acceleration of the flow around the leading edge on the pressure side. The pressure side the flow accelerates around the leading edge and there is an increment of the diffusion on pressure blade surface. The pressure distributions on the front of the suction and pressure surfaces swap and in this case the diffusion increases on the pressure surface. If the diffusion becomes too high, the flow can separate on the pressure surface.

As already mentioned, the incidence varies during off-design condition, when the mass-flow rate or the rotating speed are different from the aero design point. So, it is fundamental to

know the blade tolerance respect to the incidence in order to determine the operating limits. Typically, the variation range of the incidence that a blade needed to tolerate is around $\pm 5^{0}$ but the effective value depends on the application. The inlet Mach number has a large impact on the tolerance range, in particular the lower the inlet Mach is, the greater the incidence that the blade is able to tolerate.

Another aspect that must be taken into consideration during the blade load design is the real outlet flow angle. The outlet blade angle and the outlet flow angle are not coincident and their difference between the two ones is called deviation (see Figure 2.3):

$$\delta = \alpha_2 - \chi_2 \tag{5}$$

The difference between these two angles is due to many factors all related to potential effects. The diffusion within the blade passages is associated with diverging streamlines and therefore the flow is not moving in a single direction. Another contribute is given by the spacing between the blades. The axial dimension of the uncovered part of the meridional channel has an impact on the amount of the deviation because of the blades do not guided the flow in that area. The deviation is also affected by the development of the endwall boundary layers along the compressor, which increase the blockage and thus change the actual shape of the blade.

2.1.1.3 Thermodynamics and losses

The angular momentum variation through a rotor blade, whose velocity triangles are reported in Figure 2.1, is given by:

$$M = \dot{m}(r_2 c_{\vartheta 2} - r_1 c_{\vartheta 1}) \tag{6}$$

The specific work done by the rotor on the fluid, assuming adiabatic and stationary flow, is:

$$\Delta W = \frac{\Omega M}{\dot{m}} = u_2 c_{\vartheta 2} - u_1 c_{\vartheta 1} \tag{7}$$

Replacing the expression of the specific work in the energy equation, we obtain:

$$h_{01} - h_{02} = u_1 c_{\vartheta 1} - u_2 c_{\vartheta 2} \tag{8}$$

$$h_2 + {c_2^2}/{2} - u_2 c_{\vartheta 2} = h_1 + {c_1^2}/{2} - u_1 c_{\vartheta 1} \tag{9}$$

Considering that $c_\vartheta = u_2 - w_\vartheta$, the equation (9) become

$$h_2 + {w_2^2}/{2} - {u_2^2}/{2} = h_1 + {w_1^2}/{2} - {u_1^2}/{2} \tag{10}$$

This quantity is called rothalpy. For a typical rotor of the axial compressor, there is no radial shift of the streamline across the rotor, that corresponds to impose $u_1 = u_2$. The equation (10) can be rewritten as follows:

$$h_2 + {w_2^2}/{2} = h_1 + {w_1^2}/{2} \tag{11}$$

The total relative enthalpy is therefore constant across a rotor row. Considering a stator row, the same process can be applied and the quantity that is conserved is the absolute total enthalpy:

$$h_2 + {c_2^2}/{2} = h_1 + {c_1^2}/{2} \tag{12}$$

The Figure 2.4 reports the diagram h-s, better known as Mollier diagram, that describes the thermodynamic transformations across a compressor stage.

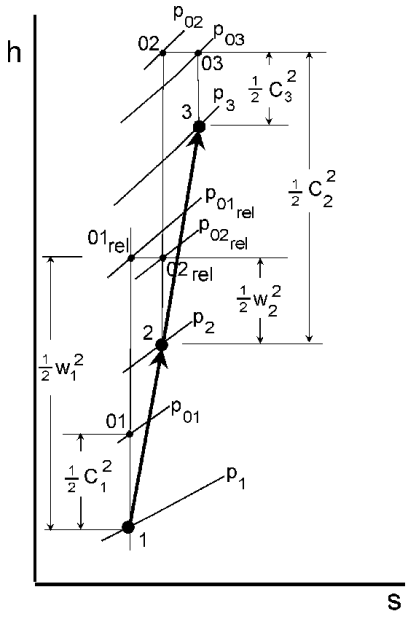

Figure 2.4 - Mollier diagram for a compressor stage

The Mollier diagram shows both isentropic ideal and real irreversible enthalpy rise across rotor row (from point 1 to point 2) and stator row (from point 1 to point 2).

The actual work performed by the stage on unit mass, obtained by combining equation (7) and (8), is:

$$\Delta W = h_{03} - h_{01} \tag{13}$$

The reversible or minimum work required to attain the same final stagnation pressure as the real process, considering the temperature rise across a stage negligible, is:

$$\Delta W_{min} = h_{03ss} - h_{01} = (h_{03} - h_{01}) - (h_{03} - h_{03ss}) \quad (14)$$

Starting from this specific work definition there are two possible definitions of the isentropic efficiency. The two definitions depend on how the exit kinetic energy is considered. Indeed, the exit kinetic energy can be useful if the current stage is followed by another stage that use that outcoming energy. But if we consider the final stage of an axial compressor the exit kinetic energy is not exploited. Consequently, it is possible to define the total-to-total stage efficiency and the static-to-total stage efficiency:

$$\eta_{tt} = \frac{\Delta W_{min}}{\Delta W} = \frac{h_{03ss} - h_{01}}{h_{03} - h_{01}} \quad (15)$$

$$\eta_{ts} = \frac{h_{3ss} - h_{01}}{h_{03} - h_{01}} \quad (16)$$

In the first one (15) the ideal compression is to the total pressure as usual. In the second one (16) the ideal compression is to the same static pressure as the actual process, with zero exit kinetic energy. The total-to-total and the static-to-total efficiency can be used to compare different point of the same axial compressor, but not for compressor that operates with different overall pressure ratio. The polytropic efficiency can be applied to overcome this issue as an axial compressor is usually composed by large number of stages. In case of perfect gas, the polytropic efficiency corresponds to the adiabatic efficiency for the small stage:

$$\eta_p = \frac{dh_{is}}{dh} = \frac{dp/\rho}{C_p dT} = \frac{\gamma - 1}{\gamma} \frac{dp/p}{dT/T} \quad (17)$$

Integrating across all the compression transformation, we can obtain:

$$\frac{T_2}{T_1} = \left(\frac{p_2}{p_1}\right)^{(\gamma-1)/\eta_p \gamma} \tag{18}$$

Hence, the polytrophic efficiency is given by:

$$\eta_p = \frac{\gamma - 1}{\gamma} \frac{\ln(p_2/p_1)}{\ln(T_2/T_1)} \tag{19}$$

Stages with equal polytropic efficiency do not have the same isentropic efficiency. In detail, the one with the lower pressure ratio will have the higher isentropic efficiency, and this highlights the fact that the isentropic efficiency could be misleading to compare stages with different loads.

The aerodynamic losses across a compressor stage are another important issue that is strictly related to the stage efficiency. Several parameters have been defined to assess it. The stator and rotor loss coefficients reported in this thesis are the following:

$$\xi_{rotor} = \frac{p_{01,rot} - p_{02,rot}}{p_{01,rel} - p_1} \quad ; \quad \xi_{stator} = \frac{p_{02} - p_{03}}{p_{02} - p_2} \tag{20}$$

which are based upon the ratio between the drop of absolute or rothalpy-based stagnation pressure across the row and the discharge absolute or relative isentropic dynamic pressure for the stator and rotor respectively. Other definition can be used to take into account the radius variation of the streamlines or the Mach number contribute.

The loss source that causing the entropy increase across the compressor blades can be divided into the following categories:

- Profile losses
- Endwall losses

- Secondary flows
- Leakage flows

Denton [21] presents an in-depth explanation of each listed loss source. Despite this categorization, the loss sources are strictly dependent one to each other.

The profile losses are mainly due to the boundary layer development on the blade surface. The shear stresses determine an entropy generation. The profile losses include:

- Trailing edge losses
- Wake mixing losses
- Shock wave losses

The trailing edge thickness causes the flow separation on both sides of the blade and the consequent downstream wake mixing process. The boundary layer and the trailing edge losses cannot be avoided but they can be controlled through the blade profile shape because they strongly depend on blade surface pressure distribution. In addition, a well-design blade profile avoids flow separation on the blade surface at the design condition that would lead to a relevant entropy rise. Transonic blades are characterized by having additional losses due to shock waves. The shock waves, in addition of being an entropy source, interact with the boundary layer and this interaction produce further losses. In transonic compressors, in operating conditions close to stall, the shock wave can cause the complete separation of boundary layer on the suction surface.

The endwall, the secondary flows and the leakage flow losses are strictly related. The endwall losses are due to the shear stresses inside the boundary layer on the endwall surface that grows rapidly along the hub and casing of a compressor. The low-energy fluid in the endwall boundary layers interacts with the

pressure gradient between the pressure and the suction surfaces and generates complex swirling flow structures. These secondary flows cause an entropy increase due to the mixing with the mainstream flow. In addition, they interact with the boundary layers on the blade surfaces, potentially causing further loss. Koch and Smith [1] provide a method to predict the loss associated with these phenomena. The leakage losses are associated with the clearance flows coming from the gap above the rotor blade tip and below the stator blade hub. Mixing and shear losses are generated by the interaction of leakage flows with endwall and the primary flow. Moreover, the leakage flow causes blockage, reducing the overall flow capacity of the compressor stage and the stable operating range [57]. Loss reduction and stability range increment can be obtained by minimizing the clearance gap, but the minimum value is normally established by manufacturing and mechanical considerations.

Leakage flows can also be found at the hub section of stator rows, if they are built with a cantilever configuration, that is used to minimize the weight and to relieve the high diffusion at stator hub section. At the same time this layout determines an increased blockage and further loss. In addition, leakage flows arise from any gaps or seals that are present in the real geometry of a compressor, such as shroud cavities.

The 3D flow structures just described reduce the flow capacity due to the additional blockage, decrease work input, and limit the operating range. They need to be accounted during the preliminary design to maximise the compressor aerodynamic efficiency.

2.1.2 Characteristic curve

The design of an axial compressor starting from the first definition of the main parameters must consider not only the performance of design point but also the stable operating field. Usually, the operating range of the compressor is described through a series of characteristic curves called speedlines (see Figure 2.5).

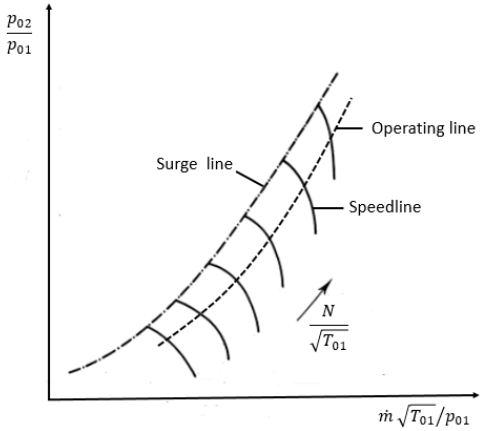

Figure 2.5 – Axial compressor characteristic curve

The characteristic curve can be defined on a diagram of total pressure ratio versus corrected mass flow. The total Pressure Ratio (PR) is defined as the ratio between the outlet total and the inlet total pressure of the compressor, while in the industrial practice the corrected mass flow definition is the following:

$$\dot{m}\sqrt{T_{01}}/p_{01} \tag{21}$$

These two coefficients are obtained from a dimensional analysis of any machines (Buckingham theory) that operates with compressible fluid:

$$\Delta h_{0s}, \eta, P = f(\mu, N, D, \dot{m}, \rho_{01}, a_{01}, \gamma) \tag{22}$$

Using non-dimensional quantities, we obtain:

$$\frac{\Delta h_{0s}}{N^2 D^2}, \eta, \frac{P}{\rho_{01} N^3 D^5} = f\left(\frac{\dot{m}}{\rho_{01} N D^3}, \frac{\rho_{01} N D^2}{\mu}, \frac{ND}{a_{01}}, \gamma\right) \tag{23}$$

The formula can be rearranged as follows:

$$\frac{p_{02}}{p_{01}}, \eta, \frac{\Delta T_0}{T_0} = f\left(\frac{\dot{m}\sqrt{RT_{01}}}{D^2 p_{01}}, \frac{ND}{\sqrt{RT_{01}}}, Re, \gamma\right) \tag{24}$$

Once the machine size and the fluid characteristics are fixed, considering high value of Reynolds number where the performances are no longer affect by Reynolds number variation, we can simplify the formula:

$$\frac{p_{02}}{p_{01}}, \eta, \frac{\Delta T_0}{T_0} = f\left(\frac{\dot{m}\sqrt{T_{01}}}{p_{01}}, \frac{N}{\sqrt{T_{01}}}\right) \tag{25}$$

The operating line (see Figure 2.5) represents the operational points of the compressor during engine acceleration/deceleration with a fixed firing temperature. Each speedline presents a constant value of correct rotational speed $N_c = N/\sqrt{T_{01}}$. Moving on a speedline a mass-flow rate reduction corresponds to an increment of the pressure ratio. Indeed, a decrease in the mass flow rate corresponds to a decrement of the absolute velocity C_1 (see Figure 2.1). This reduction determines a positive incidence on the rotor row that leads to an increase of the blade loading and consequently of the pressure ratio. On the contrary a mass flow increment generates a negative incidence on the rotor leading edge and the consequent reduction of the blade loading.

The right limit of each speedline corresponds to the choke condition that occurs when sonic condition is reached on the blade throat section and no more flow can pass through the compressor. The choke limit corresponds to the maximum flow rate and it grows as the reduced rotational speed increases. In an axial compressor stage, the sonic condition is usually reached inside the rotor row.

The left limit is determined by the surge line that separates the stable and unstable operating conditions. Moving left to the surge line, the additional mass flow reduction determines a high variation of the compressor performance due to the following phenomena:

- Compressor stall
- Compressor surge

The compressor stall is an operating condition where the incidence angle is excessive and it generates a flow separation on the rotor suction side. The blockage caused by the separation area increases the incidence on one adjacent rotor blade and decreases it on the other one. The blade with the larger incidence will tend to stall. The flow separation on this new blade automatically decreases the incidence on the previous stalled one and the separation can disappear. In other words, the stall will run in the direction in which the incidence is increasing that corresponds to the opposite of the rotating speed in the relative frame. In the absolute frame it rotates as the rotating speed but slower.

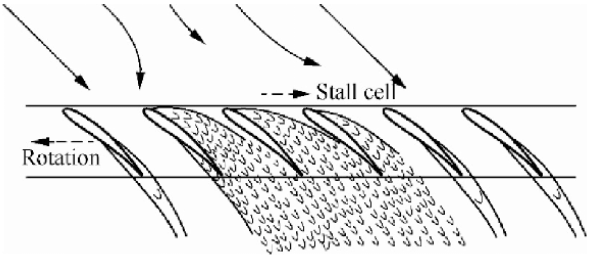

Figure 2.6 – Rotating stall inception

The area characterized by flow separation is called stall cell and it can be composed by a single blade or a blade group. In general, the performance drops and therefore stall is unwanted. In case of progressive stall, the drop in performance is quite small and the presence is only indicated by a change in noise or by high frequency instrumentation. Abrupt stall leads to a large drop in pressure rise and flow rate. In both cases the flow is no longer axisymmetric but has a circumferentially non-uniform pattern rotating around the annulus. The rotating stall is one of the several stall that can occurs inside a compressor. Day [58] reports in his work an in-depth explanation of the different inception mechanisms and development of the different stall types.

The compressor surge occurs when the overall annulus average mass flow varies with time, so that the entire compressor changes in phase from being un-stalled to stalled and back again [56]. The so-called "deep surge" arises when the flow inside the compressor is completely reversed. This process is also unwanted and can lead to serious damage (e.g. blade rubbing) due to the high transverse load placed on the rotor and casing, because of the non-axisymmetric nature of surge. However, the mechanism of surging in axial compressors is complex and is still

not yet fully understood. It is often difficult to distinguish between both, because one phenomenon could also result in the other [59]. Usually frequency is a way to distinguish between rotating stall and surge.

The axial compressor characteristic curve can be expressed also in terms of two other non-dimensional parameter:

- Flow coefficient Φ
- Work coefficient ψ

The flow coefficient is given by the ratio between the axial velocity and the local peripheral speed while the work coefficient by the ratio between total enthalpy variation across a compressor stage and the square of the local peripheral speed:

$$\Phi = \frac{C_x}{U} \tag{26}$$

$$\psi = \frac{h_{03} - h_{01}}{U^2} = \frac{C_{\vartheta 2} - C_{\vartheta 1}}{U} = \Phi(\tan\alpha_1 - \tan\alpha_2) \tag{27}$$

Considering velocity triangles shown in Figure 2.1, the stage loading can be rewritten as follows:

$$\psi = \phi(\tan\beta_1 - \tan\beta_2) = 1 - \phi(\tan\alpha_1 + \tan\beta_2) \tag{28}$$

The Figure 2.7 shows the characteristic curve in terms of ϕ-ψ of an axial compressor stage. Considering α_1, β_2 constant, a flow coefficient increase determines a reduction in the work coefficient (see equation (28)). In the ideal case without loss and separation issue, there is a linear correlation between the flow and the work coefficient. The loss sources, already explained in chapter 2.1.1.3, determine a lower value of the work coefficient with

respect to the ideal case. The difference between real and ideal case increases moving away from the design point (ϕ_d) because of the variation of the incidence angle. Increasing ϕ, the incidence decreases, and we move towards the choke region, while decreasing ϕ the incidence increment determines a greater diffusion on the suction side and consequently we get closer to the stall region.

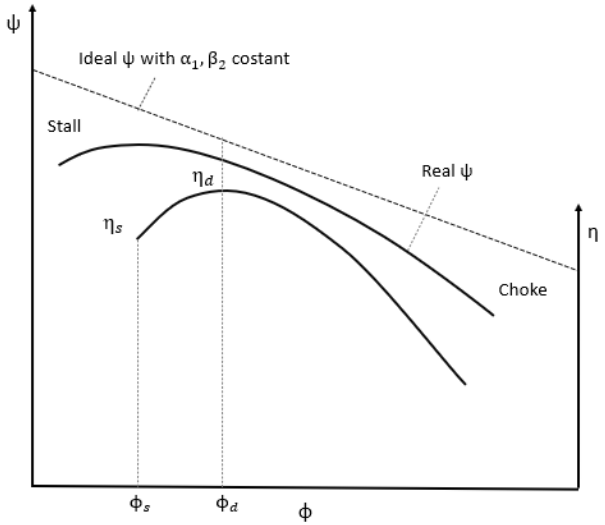

Figure 2.7 – Characteristic curve Φ-ψ of an axial compressor stage

To reach high compressor performance is essential that all the stages operate in the region with high efficiency around the design point. The matching of the stages will be treated in the following chapter.

2.1.3 Stage matching

The stage matching is a really important topic that must be taken into consideration during the compressor design. An industrial compressor consists of many stages, each of which is described by its own characteristic curve. Each stage of the compressor must operate with the optimum inlet non-dimensional speed and inlet mass-flow $\dot{m}$ at the design point that corresponds to the operating condition where the compressor will operate for most of the time. The problem of matching the inlet flow requirements of each stage to the outlet flow of the upstream one is general to all multi-stage compressors. Nevertheless, it is important that the compressor presents high efficiency and adequate pressure ratio also during off-design conditions where the stages match differently with respect to the design condition.

The compressor flow function F is given by:

$$F = \frac{\dot{m}\sqrt{c_p T_0}}{A p_0} \tag{29}$$

Where A corresponds to the cross-sectional area. The cross-sectional area decreases along the compressor to obtain an almost constant axial velocity despite the density rise. The issue of operating in different conditions from the design one is that an excursion in the flow function at inlet of a stage generally leads to a larger excursion at outlet. This because the pressure ratio $PR = P_{02}/P_{01}$ depends strongly on the flow function. The ratio of inlet to outlet flow functions can be approximated as:

$$\frac{F_2}{F_1} = \frac{\dot{m}_2}{\dot{m}_1} PR^{\frac{\gamma-1}{\gamma \eta_p}} \approx PR^{-k} \;\; with\; k > 0 \tag{30}$$

$$F_2 \approx \frac{F_1}{PR^k} \tag{31}$$

From the previous equation, we can obtain:

$$\frac{dF_2}{F_2} = \frac{dF_1}{F_1} - k\frac{dPR}{PR} \tag{32}$$

Considering, for example, a 1% reduction of the inlet flow function of a stage at fixed speed, the pressure ratio will increase and the outlet flow function will decrease by more than 1%. Similarly, an in-crease in the inlet flow function of the stage will produce a larger increase in the outlet flow function. A multistage compressor amplifies the effect of the mismatching because of it is multiplied stage by stage. Indeed, the overall pressure ratio can be written as:

$$PR_{overall} = PR_1 PR_2 \dots PR_n \tag{33}$$

Where PR_1 is the pressure ratio of the first stage and so on. The Figure 2.8 show the overall pressure ratio/flow function characteristic curve together with the characteristic curves of the first and the last stage.

It is immediately clear the mismatch during off design conditions that increases from first to the final stage. The four points on the overall compressor characteristic curve represents the following operating conditions:

- Point a → design point
- Point b → reduced pressure rise at the design speed
- Point c → increased pressure rise at the design speed.
- Point d → reduced rotational speed

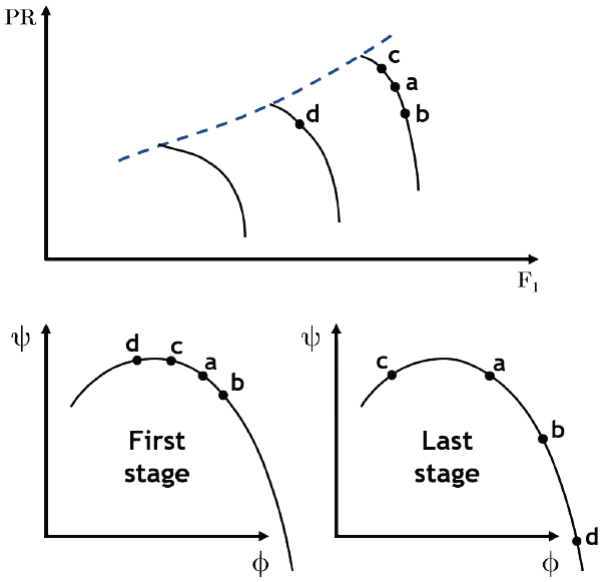

Figure 2.8 - Overall pressure ratio/mass-flow characteristic and characteristic curves for the first and last stage

The position of point a remain the same on the first and last stage characteristic curve. For the point b, the mass flow is grown, so the flow coefficient of the first stage (ϕ_1) is increased, which results in a decrease in ψ. This decrease in pressure ratio causes a decrease of the density at the entry of the second stage. As a consequence the axial velocity increases at the entry of the second stage ($C_x \uparrow = \dot{m}/\rho \downarrow A$) which increases the flow coefficient of the second stage (ϕ_2). This effect is propagated through the compressor till the last stage that corresponds to the point b on the bottom right plot in Figure 2.8. The final stage can arrive to choke condition by increasing the inlet mass flow. This process can be summarized as follow:

$$\phi_1 \uparrow \Rightarrow \psi_1 \downarrow \Rightarrow PR \downarrow \Rightarrow \rho \downarrow \Rightarrow c_x \uparrow \Rightarrow \phi_2 \uparrow \Rightarrow \cdots \Rightarrow \phi_n \uparrow \Rightarrow choke$$

The point c is characterized by reverse effect of point b. The flow coefficient is decreased and so the flow coefficient. The work coefficient and the pressure ratio increase. The inlet density of the second stage increases leading to a decrease of the axial velocity ($C_x \downarrow = \dot{m}/\rho \uparrow A$). As a result, the second stage is characterized by having a lower flow coefficient (ϕ_2). This effect is propagated through the compressor and can lead to the stall of the final stages. This process can be summarized as follow:

$$\phi_1 \downarrow \Rightarrow \psi_1 \uparrow \Rightarrow PR \uparrow \Rightarrow \rho \uparrow \Rightarrow c_x \downarrow \Rightarrow \phi_2 \downarrow \Rightarrow \cdots \Rightarrow \phi_n \downarrow \Rightarrow stall$$

Finally, the effect of a rotational speed reduction is highlighted by point d behaviour. The density rise through the compressor is reduced below the design value. Consequently, the final stage is choked and limits the mass-flow rate. The first stages operate with a lower mass-flow rate with respect to the design condition. This means that the incidence increases and this can lead to stall.

2.2 Aeromechanical design

Aerodynamic design is crucial for optimizing the performance and stall margin of a compressor. Nevertheless, vibration issues may compromise blade-row integrity thus leading to premature failures. In light of this, the aeromechanical design is at least as important as the aerodynamic ones for proper compressor design. The aeroelasticity [60] [61] is the discipline that studies the interaction between inertial, elastic and aerodynamics forces that may occur when an elastic body is invested by a fluid flow. Figure 2.9 shows that fluid dynamics, dynamics and structural mechanics interact each other when considering aeroelastic phenomena. Collar [62] provides an historical summary of aeroelasticity.

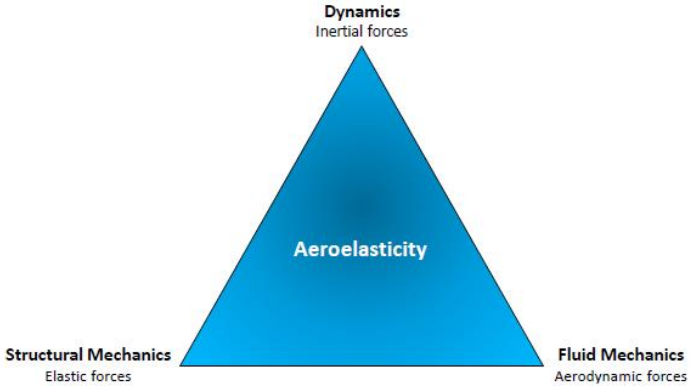

Figure 2.9 – Collar triangle

The two main phenomena of the aeroelasticity are the following:

- Flutter
- Forced responce

Flutter is a self-excited and self-sustained aeroelastic vibration caused by the flow unsteadiness around an oscillating blade. In turbomachinery, forced response is the aeroelastic matter that studies the blade vibrations caused by external unsteady aerodynamic forces due to the rotor-stator interaction [24]. In the following chapters, the main aeromechanics design aspects will be discussed, with a particular focus on the new aspects and approaches introduced during this work.

2.2.1 Blade row modeshape and mode families

The modeshape describes any deformed position that the structure assumes at the different natural frequencies of the system. For turbomachinery blade-row, the different modeshapes can be grouped in "family" depending on their deformed shape (i.e. first

bending, first torsion, etc.) and the natural frequency. The blade row can be considered "tuned" when all blade + one-pitch angular sectors composing the entire wheel are identical in terms of geometrical and mechanical properties. This is an ideal condition because the turbomachinery manufacturing is affected by uncertainties that lead to small property discrepancies between different blade angular sectors of the same row (the so-called andom mistuning). If we consider the approximation of tuned cyclic structures with N identical sectors, each mode shape family consists of n vibration waves of the whole blade-row, named nodal diameters which occur by pairs, a cosine and sine modes at the same frequency.

Figure 2.10 shows the cosine and sine mode for ND=3. Nodal diameters represent the lines that connect the zero crossings symmetrical to the centre. The maximum number of nodal diameters depend on sector numbers:

- N/2 for an even number of sectors
- (N-1)/2 for an odd number of sectors

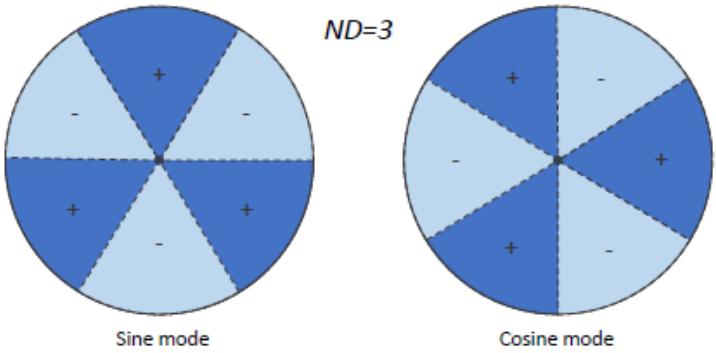

Figure 2.10 – Sine and cosine mode with ND=3

The rotating modes are characterized by a pair of traveling waves, one forward and one backward, that produce in the identical sector oscillation with the same amplitude and frequency but phase-shifted. The phase is called Inter-Blade Phase Angle and it is defined as follows:

$$IBPA = \frac{2\pi}{N} n \text{ with n} \in Z\text{: } -\frac{N}{2} < n \leq \frac{N}{2} \qquad (34)$$

where n is the number of nodal diameter and N is the number of sectors. The sign of the IBPA determines the wave propagation direction with respect to the rotational speed:

- IBPA > 0, the next blade is in phase advance and the travelling wave propagates in a backward direction.
- IBPA < 0, the next blade is in phase delay and the travelling wave propagates in a forward direction

Figure 2.11 shows the frequency curve of the blade alone family (red curve) and the disk family (blue curve), as if we consider the two component as separate entities. The blade alone curve has a constant frequency as a function of nodal diameters. The disk alone family is closely linked to the nodal diameter concept, in particular the frequency always increases with the nodal diameter. The mechanical connection between blades and disk along with the disk stiffness has an important impact on the natural frequency of the structure. Fir-tree or dove tail attachments may be used at the root of the blade while rotor blades are often welded to the disk or even produced as integral part of both disk and blade (blisk). The blade-alone modes are predominant in terms of natural frequency for disk with high stiffness. When the disk stiffness is low, the rotor and the blade mode interact with each other. The purple line shown in Figure 2.1 shows the typical frequency curve of the first mode of a

bladed disk in a cantilever configuration (i.e. blade without any type of contact at tip section).

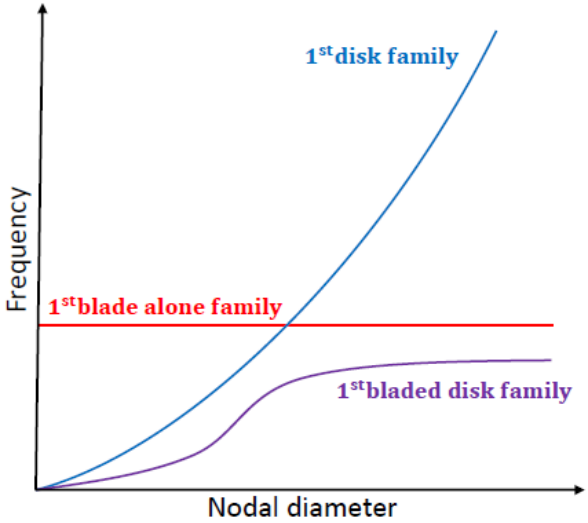

Figure 2.11 – Blade and disk family frequency curve

The curve trend is given by the combination of the two alone modes. With low ND the curve is dominated by disk modes while for high ND the curve tends to be constant as the blade-alone mode become predominant. Mode shapes of a bladed disk may be real or complex, which means that both sine and cosine shapes are present along the circumferential direction. Figure 2.12 reports the mode shape displacement contours and the modal displacements of three selected points on the blade surface. The polar diagrams on the left shows that the real modal displacements are in phase or counter-phase for all the points, while the phase shift is different between different points for the complex mode as shown on the right.

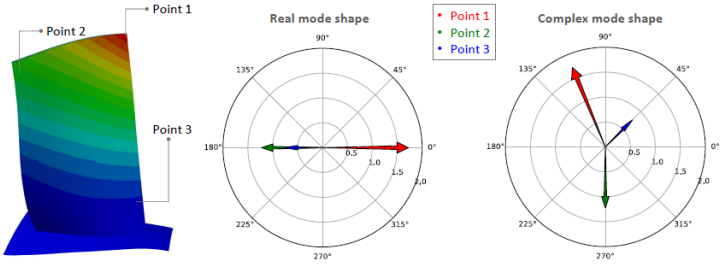

Figure 2.12 - Real and complex mode shape displacements

2.2.2 Flutter

Flutter is a self-excited and self-sustained aeroelastic vibration caused by the flow unsteadiness around an oscillating blade. Thus, flutter is usually an asynchronous problem meaning that no excitations due to neighbouring blade-rows are needed to maintain or magnify the blade vibration. From a physical point of view, flutter is an unstable condition of an elastic structure immersed in a fluid flow: initially, the vibration starts with small amplitudes due to the overall unsteadiness and then, the oscillation amplitude may rapidly increase by the energy exchange with the fluid flow, thus leading to structural failure [63]. The components which are most affected by this phenomenon in turbomachinery are high aspect ratio blades subjected to high loads [64], such as LP stages for an axial compressor. The flutter design starts with the evaluation of the operating range. The blade geometries must be developed with safety flutter margins for all the operating range. The second step is the evaluation of the average flow around the blade. This is necessary to compute the average temperature and pressure distribution on the blade surface because the static stresses have an impact on the mode natural frequency. A further step is the evaluation of natural

frequency and mode shapes, that strictly depends on the choice of the blade material and geometry. The dynamic of the system is also affected by the blade-disk connections with the shaft or tip shroud and snubbers. Usually, a modal analysis is performed to evaluate these aspects. Finally, the aerodynamic work is computed by integrating the unsteady pressure overall the blade surface within a single oscillation period. The aerodynamic work can be expressed by the following equation:

$$W_{aero} = \int_{t}^{t+T} \int_{\Sigma} (-p)\vec{n} \cdot \overrightarrow{v_b} d\Sigma \, dt \tag{35}$$

where p is the pressure field over the blade, $\vec{n}$ is the surface outgoing normal vector, $\overrightarrow{v_b}$ is the blade velocity during the oscillation period, Σ is the blade surface and T is the vibration period. The sign of the aerodynamic work determines the aeroelastic stability. A positive work indicates that the energy flux is from flow to blade and therefore the vibration may be amplified. On the contrary, whether the work is negative, blade is transferring energy to flow and the oscillation is damped. The different aeroelastic behaviour mainly depends on the local phase shifting between unsteady pressure and blade vibration.

2.2.2.1 Aerodynamic damping estimation

The aeroelastic stability assessment can be performed also evaluating another parameter: the aerodynamic damping. The overall damping is defined as the sum of structural damping ζ with the critical damping ratio ξ. From the aerodynamic work, the critical damping ratio can be computed by the following formula:

$$\xi_{aero} = \frac{-W_{aero}}{8\pi E_{kin}} = \frac{-W_{aero}}{2\pi m \omega^2 A_m^2} = \frac{-W_{aero}}{8\pi^3 \nu^2 A_m^2} \tag{36}$$

where W_{aero} is the aerodynamic work (35), E_{kin} is the blade average kinetic energy, m is the modal mass, A_m is the modal amplitude and ν is the vibration frequency. The aerodynamic damping in term of logarithm decrement can be evaluated by:

$$\delta_{aero} = 2\pi\xi_{aero} \tag{37}$$

The damping can be expressed also in terms of amplification factor, defined as follows:

$$Q = \frac{1}{2\xi_{aero}} \tag{38}$$

When dealing with blade vibration due to flutter, three different situations might occur (reported in Figure 2.13):

a) Damped oscillation
b) Limit cycle with stable oscillation
c) Self-increased vibration

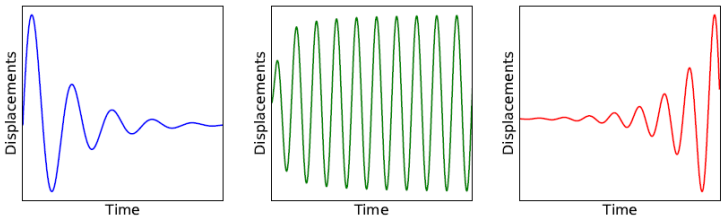

(a) Damped oscillation (b) Limit cycle (c) Flutter oscillation

Figure 2.13 - Possible situations of blade-row vibration

The case *a* corresponds to the stable condition, where the overall damping ratio is positive and any oscillation is damped. The case *b* occurs when the overall damping ratio is equal to zero. This means that the critical damping ratio is negative with the same absolute value of the structural damping. This condition is marginally stable which means that in absence of external

driving forces the oscillation amplitude remains constant on a so-called limit cycle. HCF blade failure may occur because of the high stresses due to the blade vibration. The case *c* represents the worst condition, where the blade absorbs energy from the flow and its vibration is amplified over time. In this case the critical damping ratio is negative and its modulus is greater than the structural damping. The structural damping is not easily predictable and it may need a dedicated experimental campaigns. For this reason, even if negative values of critical damping ratio do not necessary lead to a flutter oscillation, a common flutter stability criterion is to have positive values for all the possible nodal diameters.

2.2.3 Forced response

Forced response is the aeroelastic matter that studies the blade vibrations caused by external unsteady aerodynamic forces due to the rotor-stator interaction [65]. The resonance condition occurs when the forcing frequency coincides with the bladed disk natural frequency. All the possible synchronous excitations that can excite the blade-disk are called engine orders. The compressor design requirements are to avoid resonance conditions within the operating range in order to prevent high cycle fatigue failures [66]. The forced response design can be summarized in the following step:

- **Identify possible sources of excitation**
  The main aerodynamic source of excitation is the interaction with upstream and downstream rows, in particular the wakes effect due to upstream blade rows and the potential field effect generated by the downstream blade row. The excitation frequency is associated with the blade passing frequency (BPF) and its higher harmonics. Exciting force amplitudes are independent from

the blade displacements [67]. Excitation force at low engine order can also be generated by circumferential inlet flow distortion in terms of pressure, temperature, and velocity. Tangential flow distortions can be generated also by rotating stall or injections/extractions that lead to resonance conditions. Finally, an unsteady force on the rotor row can be caused also by an asymmetry in flow-path geometry. The exciting forces can be produced also by the interactions between mechanical components such as gear tooth meshes or rub and blade rows.

- **Determine operating speed range**
  Resonance conditions that occurs out of the operating range are not harmful regarding the axial compressor life cycle.

- **Calculate natural frequencies and mode shapes**
  Usually, a modal analysis is performed to predict natural frequencies and mode shapes. As already said in chapter 2.2.2, it is important to correctly model the blade-disk connections because it is not negligible regarding the dynamic of the system,

- **Build resonance diagram**
  The resonance diagram is used to check which unsteady forces actually excite the blade rows. It will be discussed in detail in chapter 2.2.3.1.

- **Determine response amplitudes**
  The forced response amplitude does not just depend on the force amplitude but on the matching between the

unsteady force distribution on the blade surface and the mode shape displacements. In this work, the force response analysis has been performed with a modal work approach (see chapter 2.2.3.4)

- **Calculate stress distributions**
  The blade stresses are given by the sum between static and alternating stresses. The alternating stresses are evaluated starting from the forced response results and adding the contribute of the overall damping.

- **Construct Goodman diagram and determine High Cycle Fatigue (HCF) life**
  The HCF life assessment (see chapter 2.2.3.5) is the final step that determine the goodness of the design. If the HCF life is not infinite, a redesign of the investigated blade rows is necessary.

- **Conduct strain gaged rig/engine tests to verify predicted response amplitudes**
  The forced response is not easy to be predicted both in terms of amplitude and excited frequencies. The actual industrial design tools are not sufficiently accurate regarding the forced response analysis. Considering the importance of avoiding blade premature failure, strain gaged rig/engine tests must be conducted to verify predicted response amplitude and also to control unexpected blade vibration.

2.2.3.1 Campbell and Interference diagram

The resonance diagram is a fundamental tool to predict the presence of resonance conditions. The Campbell diagram is one

of the most used resonance diagrams, and it reports the blade eigenfrequencies as function of the rotational speed. An example of Campbell diagram is shown in Figure 2.14.

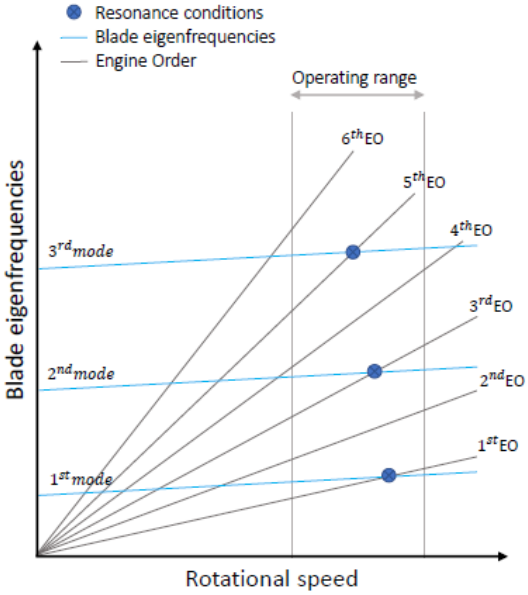

Figure 2.14 - Campbell diagram

The increase of rotational speed corresponds to an increase of the blade temperature and of the centrifugal force. Usually, the centrifugal stiffness has a predominant effect respect to the thermal softening due to the higher temperature, so the blade natural frequencies of a rotor row tend to increase with the rotational speed. The Campbell diagram also reports the curve of the engine order excitation frequency and its multiple. It is defined as follow:

$$\nu_{EO} = \frac{\Omega\, EO}{2\pi} \tag{39}$$

where ν_{EO} is the excitation frequency, Ω is the rotational speed and EO is the engine order. If a mode curve intercepts the EO curve inside the operating range (blue circles in Figure 2.14), it means that rotor row natural frequencies coincides with the forcing frequencies and so it corresponds to a resonance condition. The Campbell diagram is limited by the fact that it is valid only for a single nodal diameter. A bladed disk configuration with low disk stiffness can have a relevant change in the eigenfrequencies with the nodal diameter number.

Forcing Engine Order	**Aliased Engine Order**	**Perturbation direction**
$\boldsymbol{EO \leq N/2}$	EO	*Backward*
$\boldsymbol{N/2 < EO \leq N}$	$N - EO$	*Forward*
$\boldsymbol{N < EO \leq 3N/2}$	$EO - NB$	*Backward*
$\boldsymbol{3N/2 < EO \leq 2N}$	$2NB - EO$	*Forward*

Table 1 – Aliased engine order for even blade number (N is the number of blade sectors)

Forcing Engine Order	**Aliased Engine Order**	**Perturbation direction**
$\boldsymbol{EO \leq (N-1)/2}$	EO	*Backward*
$\boldsymbol{(N-1)/2 < EO \leq N}$	$N - EO$	*Forward*
$\boldsymbol{(N-1)/2 < EO \leq (3N-1)/2}$	$EO - NB$	*Backward*
$\boldsymbol{3N/2 < EO \leq 2N}$	$2NB - EO$	*Forward*

Table 2 – Aliased engine order for odd blade number (N is the number of blade sectors)

In this case, the Interference diagram, also called "Zig Zag shaped Excitation line in the Nodal diameter versus Frequency"

(ZZENF) diagram, developed by Wildheim [68] [69], can be used. The Interference diagrams also adds the information relative to the different nodal diameter. It provides the eigenfrequencies and engine order versus the nodal diameter number. The purpose of the Interference diagram is to identify which EO causes the resonance condition for a certain blade-row mode family (nodal diameter mode). The Interference diagram is based on the following assumptions:

- The structure has in cyclic symmetry configurations
- The exiting force is a rotating perturbation (the EO is given by the blade number of the excitation row) that will excite the structure with a harmonic index equal to the aliased engine order

The aliased engine order can be detected with the formula explained in Table 1 and Table 2. The perturbation direction has been reported with respect to the rotational direction. It is important because the aerodynamic damping change from forward to backward traveling wave and so it will have an impact on the system response. The resonance conditions for a rotationally periodic structure are when natural frequencies match the following relationship:

$$\omega_n = (kN \pm n)\Omega \tag{40}$$

with $k = 0, 1, 2, \dots, N$. where Ω is the natural frequency, N is number of blade sectors and n the nodal diameter. Only intersections at integer values of n lead to resonance.

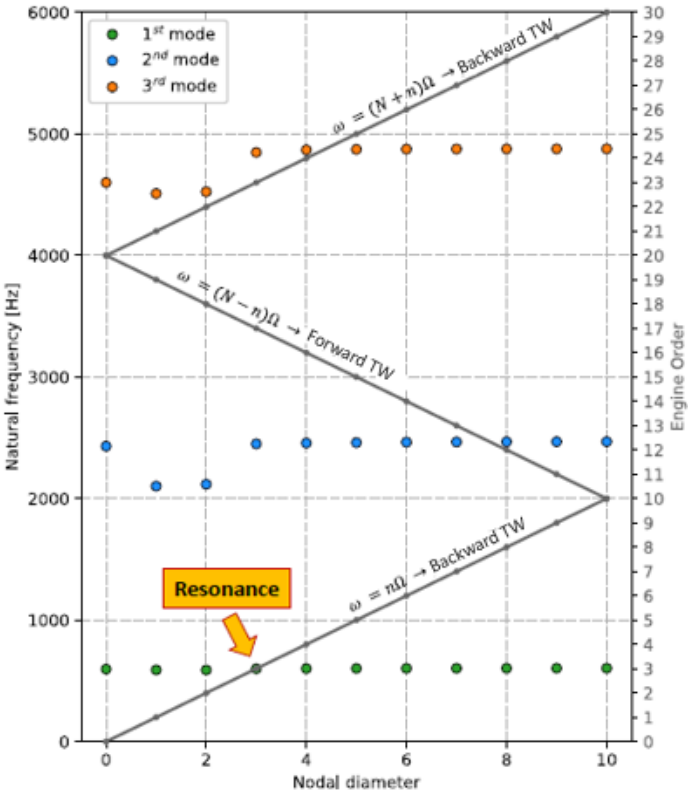

Figure 2.15 – Interference diagram

An example of Interference diagram built for a 20-blades axial compressor row is reported in Figure 2.15. A resonance condition occurs for the first bending mode family caused on the EO = 3 for a given rotational speed. The versus of the grey Zig-Zag line indicates the travelling wave propagation direction respect to the rotational speed direction.

2.2.3.2 Forcing circumferential decomposition

The unsteady forcing that may excite a blade row can be numerically evaluated through an unsteady CDF analysis. The time-varying pressure fluctuation can be decomposed in time to extract the harmonic content at a single Engine Order (EO) by the following formulation:

$$P^{(h)} = \frac{1}{N_{div}} \sum_{n_t=0}^{N_{div}-1} p_t \, e^{-ih\frac{2\pi}{N_{div}}n_t} \tag{41}$$

in which h is the time harmonic index (or Engine Order), p_t is the discrete equally-space pressure signal in time and N_{div} is the total number of samples. A preliminary study of the blade unsteady loading variation along an entire blade-row shows that the amplitude distribution of the pressure time-Fourier coefficients on the blade-row is not constant in the circumferential direction (see Figure 2.16). The circumferential variability along the entire blade-row suggests that the unsteady forcing is not composed by a single rotating forcing but by a more complex structure. Also the unsteady lift amplitude (coming from a temporal DFT of the time blade load history) of a single EO presents a relevant blade-to-blade variation. Figure 2.17 shows the unsteady lift amplitude along the same blade row of Figure 2.16. This behavior suggests the need for a specific spatial decomposition that follows the concept of blade mode-shape in cyclic symmetry. To extract the pressure fluctuation components in the cyclic symmetry environment, the resulting complex Fourier coefficients $P^{(h)}$ are spatially decomposed along the circumferential direction. The time-space Fourier coefficients are extracted as follows:

$$\hat{P}_{(m)}^{(h)} = \frac{1}{N} \sum_{k=1}^{N} P_k^{(h)} \, e^{-im\frac{2\pi}{N}k} \tag{42}$$

in which m is the circumferential order, $P_k^{(h)}$ the discrete time Fourier coefficient tangential distribution on blade corresponding surface points and N the blade count. It allows to determine the rotating perturbation that will excite the corresponding traveling wave mode-shape.

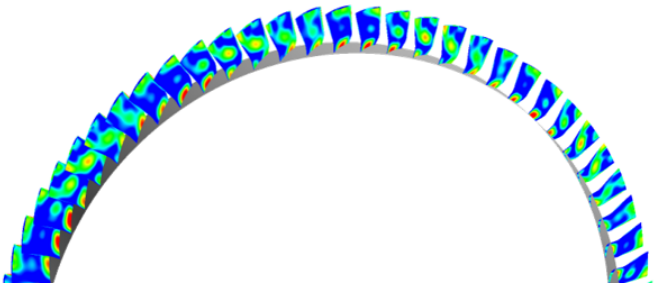

Figure 2.16 - Amplitude of pressure of time Fourier coefficients on adjacent blade surfaces along the blade-row

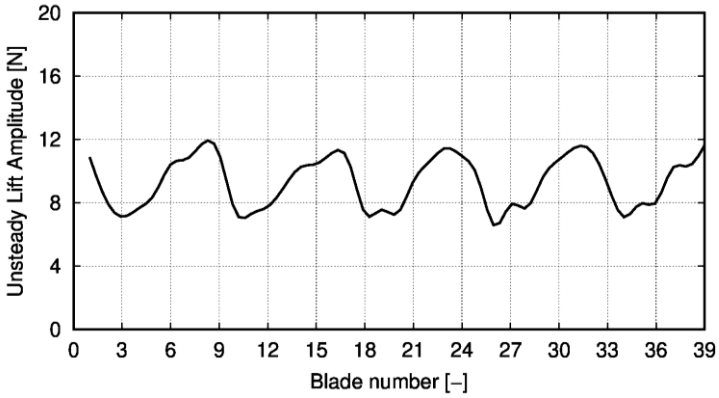

Figure 2.17 - Unsteady lift amplitude along the blade-row

This approach, that extracts perturbations in space-time (spinning lobes in annular ducts as described by Tyler and Sofrin [30]), is usually employed in aeroacoustics where this circumferential decomposition is performed along the computational grid in the annular duct between rows to extract noise components in terms of their acoustic power.

In this thesis, a new approach has been introduced to extract the pressure fluctuation components on the blade surface in the cyclic symmetry environment. In the present time-space decomposition, the circumferential DFT is performed on a coarse down-sampled (with respect to acoustic analysis) set of only N samples taken on each blade at the corresponding axial and radial position, far circumferentially one blade pitch. Hence, the extracted rotating pressure components have a number of lobes ranging from (-N)/2 to (+N)/2 or from (-(N-1))/2 to (+(N-1))/2 in case of odd blade count as suggested by the Nyquist's theorem. It is clear how this approach also takes into account the aliasing phenomenon experienced by the blade-row when excited by a rotating perturbation with a lobe number higher than N/2. Figure 2.18 provides a visual representation of a possible excitation scenario, where a rotating perturbation with 16 lobes, represented by the violet solid line, impinges on a row composed by 12 blades represented by the gray radial segments. The 12 blades experience a 4-lobe perturbation represented by the green dashed-line due to the aliasing phenomenon. The orange dash-dot radial lines highlight the resulting 4 nodal diameters associated with the 4-lobe excitation.

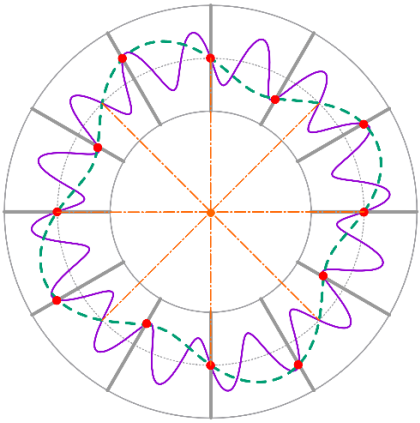

Figure 2.18 - Sketch of lobe circumferential pattern and aliasing

The proposed spatial decomposition on "blade-sampled" corresponding N points along the circumferential direction is thus able to convert the 16-lobe incoming perturbation in the 4-lobe excitation experienced by the blade-row which will finally vibrate as a traveling wave with 4 nodal diameters.

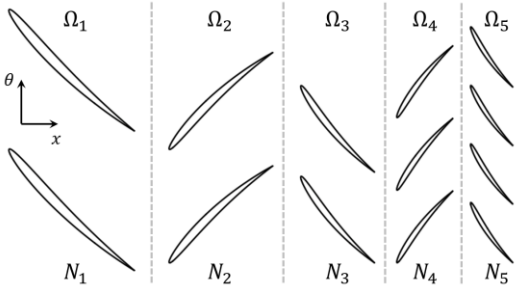

Figure 2.19 - Blade-to-blade sketch

Therefore, it is essential to evaluate all the possible rotating lobes that compose a single engine order perturbation: each spinning lobe can be seen as direct or aliased excitations for the blade-row. Tyler and Sofrin [30] theory states that rotor-stator interactions generate pressure spinning lobes, that are in fact acoustic waves, which travel along the machine causing additional "acoustic excitations" for a given blade-row. The concept of Tyler and Sofrin modes is thus employed to decompose the overall perturbation. The resulting rotating lobes perturbation predicted by theory are included in the improved use of the interference diagram to detect any further possible crossing. The presented theory is a generalization (with different rotational speeds) of the original Tyler and Sofrin formulation and also includes propagation effects and further scattering by previous or successive blade-rows [70]. The generalized rotor-stator interaction theory predicts the generation of rotating perturbations with the number of lobes m (circumferential order) and angular frequency ω in the different frame of reference (fixed or rotating with rotational speed Ω). For instance, with reference to Figure 2.19, the rotating lobes in the frame of reference of the blade-row 2 see are characterized by:

$$m_2 = k_1 N_1 - k_2 N_2 \tag{43}$$

$$\omega_2 = k_1 N_1 (\Omega_1 - \Omega_2) \tag{44}$$

where N is the blade count and k is an integer value called harmonic or scattering index [30] and Ω the rotational speed. The sign of m is coherent with the θ direction reported in Figure 2.19. Such acoustic perturbations travel upstream and downstream with different propagating behaviors depending on the axial wave number k_x. The k_x quantity can be real (the corresponding acoustic mode is cut-on) or a complex value (the mode is cut-off). Cut-off modes decay as they axially propagate,

whereas cut-on waves keep their amplitude unchanged resulting more dangerous for aeromechanical and acoustic implications.

A single spinning lobe changes its frequency when it is seen in a different frame of reference as follows:

$$\omega_3 = -\omega_2 + m_2(\Omega_3 - \Omega_2) \tag{45}$$

Moreover, the pressure perturbation also experiences successive scattering when propagating across other blade-rows. The scattering effect due to a further blade-rows with N blades generates new sets of rotating perturbations with circumferential order m_s related to the fundamental propagating one m_f by the following relations:

$$m_s = m_f + k_s N_s \tag{46}$$

Scattered waves also change their angular frequency with respect to the fundamental one when analyzed in a different frame of reference where the scattering occurs. For instance, when studying spinning lobe frequencies in the absolute frame of reference (the statoric frame), stator scattering does not alter the fundamental frequency ω_f, while rotor scattering generates scattered perturbations with the following new frequencies:

$$\omega_s^{\text{abs}} = \omega_f + k_s N_s \Omega_s \tag{47}$$

Vice versa, in the rotor frame of refence, the stator scattering produces additional rotating lobes with different frequencies.

It is thus evident that the scattering phenomenon, due to the interaction of Tyler and Sofrin modes with successive blade-rows, generates a number of additional perturbations potentially dangerous for all the blade-rows and deserves to be carefully studied during the aeromechanical verification of the design.

2.2.3.2.1 Test on reduced domain

A reduced domain composed by two compressor final stages has been simulated to clarify the observed circumferential distortion of the unsteady lift amplitude at the analyzed engine order. Table 3 reports the three cases under investigation.

	R10	S10	R11	S11
Case A	80	88	80	88
Case B	76	88	80	88
Case C	80	92	80	88

Table 3 - Reduced domain: case definition

Case A corresponds to the base case, where rotor and stators rows are characterized by the same blade count, respectively. The R10 blade count of case B is decreased by four blades with respect to case A, while S10 blade count of case C is increased by four. The variation in the blade number was selected to have in all the cases a common divisor equal to four. This condition allows to perform the CFD unsteady simulations with full annulus approach on a quarter of the complete annulus, solving all the relevant frequencies and saving computational time and cost. The computational setup used for this preliminary analysis is the same used for all the unsteady CFD computations and it is reported in chapter 3.4.2. Figure 2.20 shows the variation of the unsteady lift amplitude of R10 as a function of the blade numbering included in the computational domain (1/4 of the entire wheel). The investigated frequency corresponds to the BPF due to the downstream stator row (88X for case A and B, 92X for case C). Case C and A present a constant value, while case B, that is characterized by having a different blade count between R10 and R11, shows a circumferential variation of the lift amplitude.

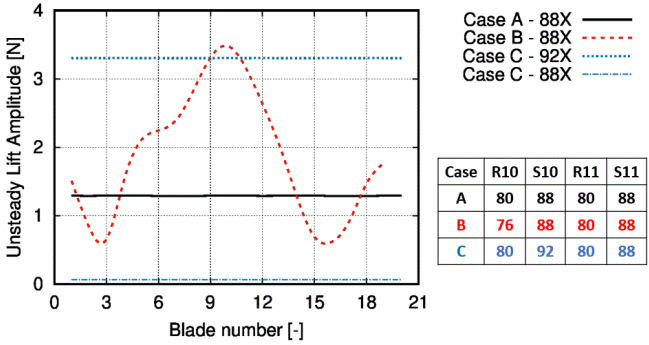

Case	R10	S10	R11	S11
A	80	88	80	88
B	76	88	80	88
C	80	92	80	88

Figure 2.20 - Harmonic lift amplitude on R10

Applying the circumferential DFT to the pressure time Fourier coefficients on the blade surface, the contribute of the different nodal diameter can be separated. The unsteady forces at 88X of case B is composed by the two main contributions which match different nodal diameters: ND=12 is excited by the interaction between R10 and S10, while ND=8 responds to the upstream running wave generated by the Tyler-Sofrin interaction between S10 and R11. The sum of two rotating unsteady rotating forces at same frequency, but different circumferential pattern leads to a variation of the amplitude along the circumferential direction. This behavior is easily explained by Figure 2.21 and Figure 2.22, that show two simplified cases characterized by the overlap of two waves, the first one with the same number of circumferential order (as for case A), and the second one with a different number of m (as for case B). The final wave composed by the sum of the two contributions presents a different amplitude trend. Figure 2.21 shows a constant amplitude trend since the overlap of two waves with the same m is identical along the circumferential direction, while the sum of two waves with different circumferential pattern varies with the tangential position and determines a non-uniform amplitude distribution, as shown

in Figure 2.22. The decomposed unsteady pressure distributions in terms of amplitude and phase for 88X on R10 surface relative to case B are reported in Figure 2.23. The upper side of the picture corresponds to the contribute that excites ND=8 while the lower side the ND=12. Also the unsteady forces at 88X and 92X of case A and case B respectively are composed by the sum of two contributes but they are characterized by the same circumferential order. In this condition it is not possible to separate the two contributions.

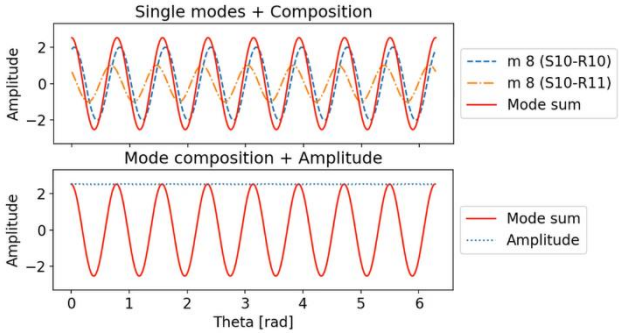

Figure 2.21 - Overlap of two sinusoidal waves with the same number of nodal diameters

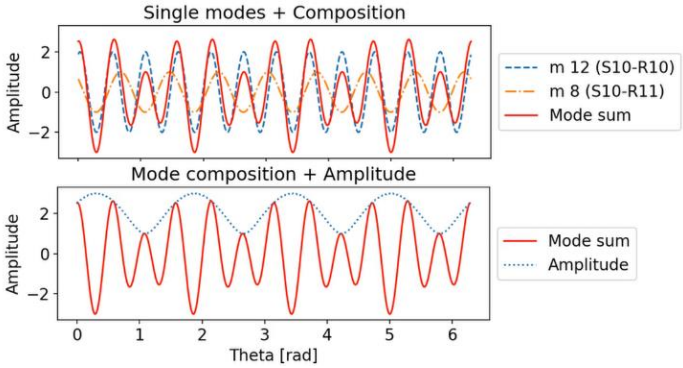

Figure 2.22 - Overlap of two sinusoidal waves with different number of nodal diameters

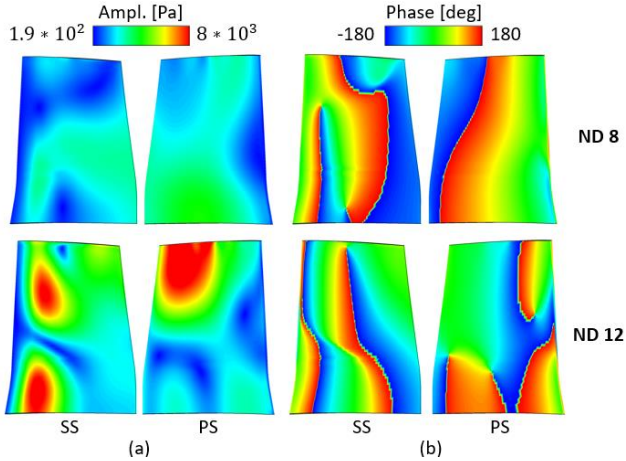

Figure 2.23 - Case B: Unsteady pressure amplitude (a) and phase (b)) from time and space decomposition: EO=88X, ND=8 (top) and ND=12 (bottom) on R10

Figure 2.24 shows the variation of the unsteady lift amplitude of S10 with the blade number. The trend is constant for case A and B, while case C presents a very slight oscillation due to the very low contribute of the upstream running pressure wave which excites ND=8 and generated by the interaction between R11 and S11.

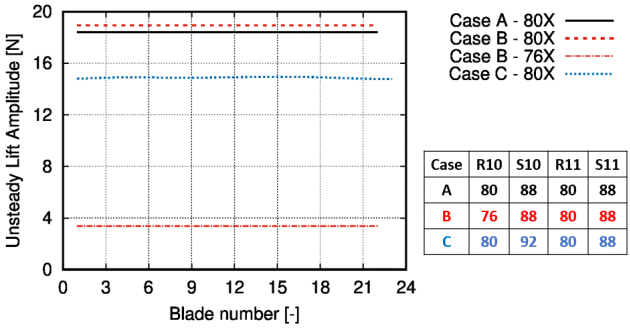

Case	R10	S10	R11	S11
A	80	88	80	88
B	76	88	80	88
C	80	92	80	88

Figure 2.24 - Harmonic lift amplitude on S10

The variation of the unsteady lift amplitude of R11 and S11 (shown in Figure 2.25 and Figure 2.26 respectively) confirms that the tangential distortions occur when the blade-rows in the same frame of reference have a different count (case B for R11 and case C for S11).

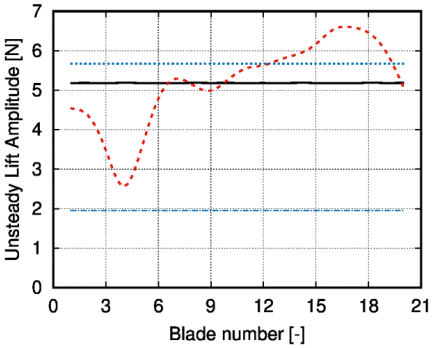

Case	R10	S10	R11	S11
A	80	88	80	88
B	76	88	80	88
C	80	92	80	88

Figure 2.25 - Harmonic lift amplitude on R11

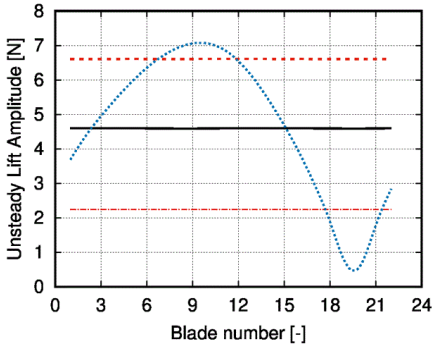

Case	R10	S10	R11	S11
A	80	88	80	88
B	76	88	80	88
C	80	92	80	88

Figure 2.26 - Harmonic lift amplitude on S11

The spinning lobes due to Tyler-Sofrin unsteady interactions (mainly acting on ND=12 both for R11 and S11) present a relevant amplitude because they are downstream running wave. The resulting tangential distortion is clearly visible when the

contribute of the Tyler-Sofrin pressure waves has an amplitude comparable to the main interaction, as shown in Figure 2.27.

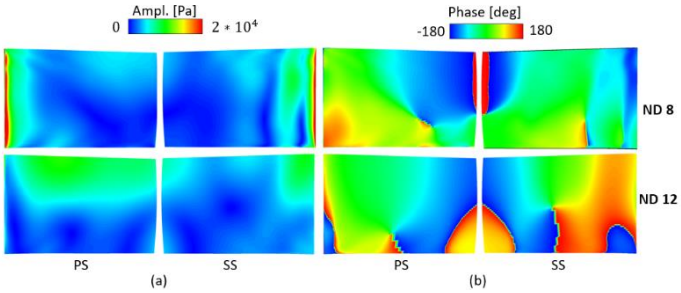

Figure 2.27 - Unsteady pressure amplitude (a) and phase (b) from time and space decomposition: EO= 88X with ND=8 (top) and ND=12 (bottom) on S11

In the three cases where the circumferential variation of the unsteady lift amplitude has been observed, the curve shows indicatively a single oscillation. Considering that the plot includes only a quarter of the full wheel and the domain is periodic, the circumferential distortions is characterized by four lobes along the full annulus. The number of circumferential distortions in the unsteady lift is related to the difference of the blade number in the same frame of reference and it is due to the fact that the two rotating waves composing the unsteady forces present the same difference in the number of nodal diameters.

2.2.3.3 Improved use of the Interference diagram

The interference diagram is based on the assumptions that the structure is in cyclic symmetry and the forcing function is a rotating pressure perturbation (with an engine order given by the excitation count) that will excite the structure at a space

harmonic index (nodal diameter) equal to the aliased engine order. The coincidence of the excitation frequency and shape of a structural mode is graphically identified in the interference diagram through the well-known "zig-zag" line (see Figure 2.15).

However, a single engine order may include additional spatial contents on top of the aliased engine order, due to different rotor-stator interactions associated with the same time harmonic. Since the additional spatial harmonics may have sufficient amplitude to cause significant blade vibratory responses, it is necessary to capture their presence in the interference diagram with the procedure explained below. A simplified rotor-stator-rotor example with the count expressed in Table 4 is reported to explain the overall identification process.

rotor1	$N_1 = 13$	$\Omega_1 = \Omega$
stator1	$N_2 = 10$	$\Omega_2 = 0$
rotor2	$N_3 = 12$	$\Omega_3 = \Omega$

Table 4 - Rotor-stator-rotor examples

With reference to the engine order 10X excitation on rotor2, the aliased engine order corresponds to the main interaction detected by the classical use of the interference diagram for stator1- rotor2 and would excite the nodal diameter equal to 2:

$$m_3 = N_2 - N_3 = -2 \Longrightarrow ND = 2 \tag{48}$$

where ND positive sign means that this interaction excites the forward traveling wave mode-shape. Moreover, also the interaction stator1-rotor1 produces nodal diameter excitations at the engine order 10X on the rotor1, that will have an impact also on the spatial content of rotor2 at the same 10X engine order due to the Tyler-Sofrin modes traveling from rotor1 to rotor2. For example, in the rotor frame of reference, the rotor1 experiences at the engine order 10X:

$$m_1^a = N_2 - N_1 = -3 \tag{49}$$

and

$$m_1^b = N_2 - 2N_1 = -16 \tag{50}$$

These two interactions generate acoustic spinning lobes that travel across the stator1 and merge in the engine order 10X on the rotor2 and will excite the following forward nodal diameters:

$$m_3^a = m_1^a = -3 \implies ND = 3 \tag{51}$$

$$m_3^b = m_1^b = -16 \overset{aliasing}{\implies} ND = 4 \tag{52}$$

This last interaction is aliased as a 4 nodal diameter excitation as already explained in the previous paragraph. In the improved use of the interference diagram, the crossings with modes having a spatial harmonic index (nodal diameter) coincident with the additional spatial content are also considered.

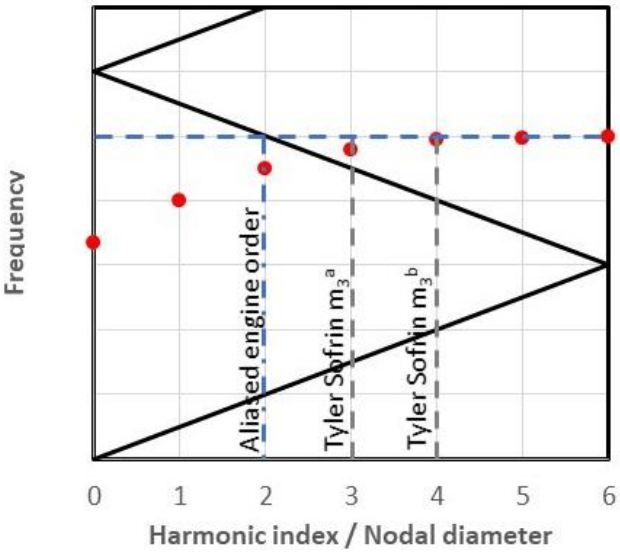

Figure 2.28 - Improved use of the interference diagram

In Figure 2.28 the sample rotor2 interference diagram is sketched, highlighting a case where the classical use of the interference diagram would not highlight any resonances at the considered speed. However, the horizontal projection of the engine order frequency 10X matches a mode that is excited by a further circumferential order of the forcing (in this case ND=4 due to m_3^b) calling for a potential resonance condition.

In summary, the recognition of additional resonances excited by Tyler and Sofrin rotor-stator interactions can be done in two steps:

- **step 1 (classical use):** determination of excitation frequency through the zig-zag line and check the overlap with any modes having harmonic index equal to the aliased engine order
- **step 2 (improved use to account for Tyler-Sofrin excitations)**: horizontal (constant frequency) projection searching for any modes having a circumferential order included in the forcing function at the studied engine order and detectable by the spatial decomposition process described in the first part of the Thesis.

In light of this, the time-spatial decomposition of unsteady forcing at the studied engine order, becomes a key aspect to detect any possible resonance conditions on the interference diagram taking into account both classical and "Tyler-Sofrin" additional crossings.

2.2.3.4 Modal work

The blade-row forced response is evaluated by means of a numerical approach based on modal work computation. The approach is valid for resonant conditions and assumes that, at a

crossing, the energy associated with the forcing function, extracted by the abovementioned spatial decompositions is equal to the energy dissipated by the overall system damping. Under this assumption it is possible to compute a scaling factor that can be applied to modal displacements and stresses to obtain the actual displacement and oscillating stress. The modal work approach determines the maximum energy transfer of a rotating pressure perturbation, decomposed on blade corresponding points and defined by the circumferential order, applied to the correspondent traveling wave mode-shape defined by the nodal diameter. The search for maximum value is required to the fact that the phase shift between rotating forcing and mode-shape is unknown. The work per cycle produced by a sinusoidal force during a steady forced vibration must be equal to the energy dissipated during one cycle due to the damping force as follows:

$$\pi dF \sin\alpha = \pi\zeta d^2\omega \tag{53}$$

where α is the phase between force and displacement. It may be assumed with sufficient accuracy that this amplitude occurs at resonance condition where $\alpha = \pi/2$,, and so:

$$\pi dF = \pi\zeta d^2\omega = 2\pi\xi d^2\omega^2 \tag{54}$$

from which

$$d = \frac{\pi dF}{2\pi\xi d\omega^2} = \frac{F}{2\xi\omega^2} \tag{55}$$

Same conclusion can be drawn for a distributed forcing acting on component modal displacements and leading to the modal force concept. It demonstrates that the scaling factor for the displacements d (and also for the stresses) depends on modal force F_m, the total system damping ξ and the square of angular frequency ω as summarized in the following formula:

$$d = \frac{F_m}{2\xi\omega^2} \tag{56}$$

The modal force can be computed by the complex dot product between the conjugate of the modal displacement δ_m^* coming from modal analysis in cyclic symmetry and the aerodynamic forcing $F_a$spatially decomposed to match the nodal diameter of the mode-shape as follows:

$$F_m = \sqrt{\left[\iint_\Sigma \Im\mathfrak{m}[\delta_m^* F_a]\, d\Sigma\right]^2 + \left[\iint_\Sigma \Re\mathfrak{e}[\delta_m^* F_a]\, d\Sigma\right]^2} \tag{57}$$

2.2.3.5 HCF life assessment

Assessment of the dynamic response amplitudes and stress distributions are necessary for determining the maximum alternating stresses and hence evaluating the high cycle fatigue life when resonances occur and cannot be avoided [71]. The stress distribution can be obtained with modal work approach or other computational methods. As already shown in chapter 2.2.3, usually measurement campaigns are performed at the end of the design loop to verify the force response amplitude. The main issue of the experimental approach is that the maximum stress locations vary with the mode shape family. As a result, several strain gauges are needed along the blade surface in order to minimize the experimental uncertainty. The amplitude response diagram and the Goodman diagram are meant to evaluate response the allowable static and alternating stresses of the blade. Figure 2.29 [72] [73] [74] reports an example of Goodman diagram where the steady and alternative stress are reported on the x-axis and y-axis respectively. The ultimate strength at zero vibratory stress and the fatigue strengths at 10^7 (or more) cycles are the two material properties that correspond to the starting point for

building the Goodman diagram. The infinite life area is defined by the red line that joins these two values.

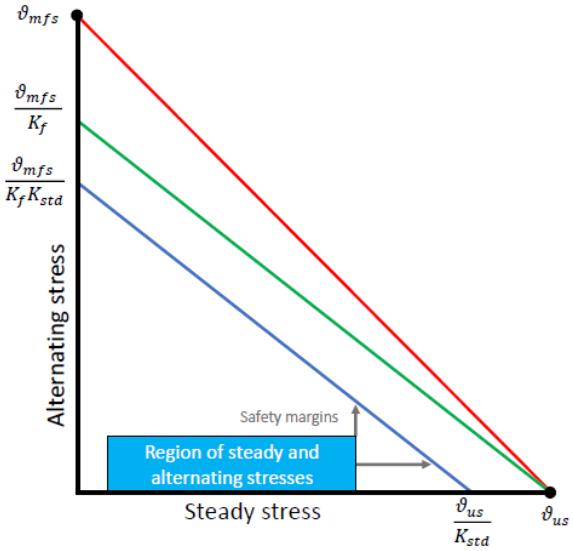

Figure 2.29 – HCF life assessment

The fatigue strength distribution may be affected by 3 main parameters:

- **Fatigue notch factor K_f**
  It is strongly dependent on the bladed disk geometry and is related to a stress concentration factor that corresponds to the ratio between the maximum steady stress to the unnotched steady stress in specific locations such as notches, holes, fillets, etc ..

- **Standard deviation of measured data**
  The component material and processing differ between components. From the test data it is possible to extract

the standard deviation factor that take into account this aspect. A minus three sigma 3 value of fatigue strength accounts for 99.865% of all pieces having a fatigue strength greater than this value.

- **Temperature**
  The ultimate and fatigue strengths are both influenced by the material temperature. The material resistance decreases as the temperature rises.

The red line is corrected with the notch factor to consider the effect of the first parameter. The green line in Figure 2.29 defines the corrected infinite life area. Finally, a "safety" coefficient is introduced to consider also the -3σ of fatigue strength that reduce the "safe" region to the one delimited by the blue line. The infinite life of the bladed disk is ensured when both steady and alternating stresses stay inside the blue triangle (see Figure 2.29).

3 Numerical methods

This chapter is aimed at introducing the numerical method and the computational setup that have been used during this work. The chapter starts with the description of the new CFD steady and unsteady design strategy proposed in this work. The second part reports the main characteristics of TRAF code, developed by the research group led by Prof. Andrea Arnone starting from the end of the 1980s. It is the CFD code that has been used for all the CFD computations presented in this thesis. The third part focuses on the numerical setup of aerodynamic and aerodamping computations.

3.1 CFD design strategy

The CFD design strategy concerns the 3D blade design. Figure 3.1 summarizes the steady and unsteady CFD design strategy proposed in this thesis. The rectangles highlighted in red correspond to the additional step respect to the actual industrial approach. The 3D design process starts with steady computation on single stage to match the performance assessed after 1D and 2D design. Once all the stages have been modified, steady run on the whole compressor may be performed. The primary purpose of this step is to verify the matching of the stages at the design condition and to apply some modifications to the blade geometry when needed. Once the design point is optimized other operating conditions are investigated with a particular focus to the stall condition. The designer may apply additional refinement to increase the stall margin. The limit of the standard approach it the low accuracy of the steady state results, especially in terms of stall margin prediction. To overcome this issue,

the new design strategy provides an additional step that involves unsteady computations on the whole axial compressor with a full-annulus approach (see chapter 3.4.2).

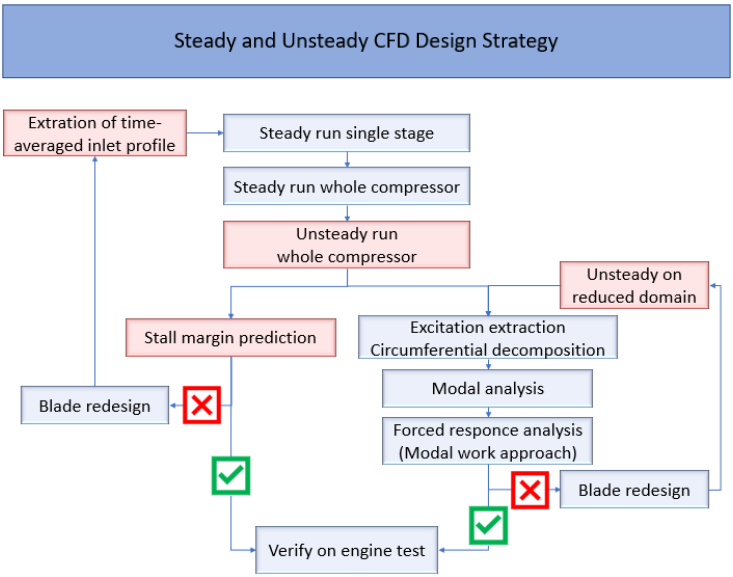

Figure 3.1 – CFD design strategy steps

From an aerodynamical point of view, the unsteady runs guarantee an improvement in the result accuracy in terms of performance and stall margin (see chapter 4.2), as well as capturing unsteady phenomena as rotating stall. From an aeromechanical point of view, the extension of the computational domain to the whole compressor for unsteady simulations allows one to evaluate all the possible excitation frequencies coming from upstream and downstream blade rows and from all the Tyler-Sofrin interactions that happen inside the compressor. This approach permits to evaluate unexpected resonances (see 5.4.2) that appear

during compressor validation tests, often calling for painful and time-consuming redesigns.

The unsteady runs, as for the steady ones, first of all provides the performance at the design point to confirm the correct prediction of steady results and apply some corrections if needed. The next parallel steps consist in the stall margin prediction and forced response analysis. If the stall margin results to be lower than the design specifications, some blade row may need a redesign. Considering the large amount of iterations needed during the blade redesign, the use of unsteady runs to optimize the stage geometry is not compatible with industrial design times. This issue can be overcome by extracting the spanwise profile of the time-average quantities from the unsteady run of the whole compressor at the inlet section of the investigated stage. The steady run on a single stage with the inlet profile condition taken from time-average quantity of unsteady computations guarantees an optimum agreement with unsteady results (see chapter 4.2.4). This technique allows to redesign the blade based on unsteady results but using a steady approach that keeps low computational times and costs.

The blade design must also consider the mechanical constraints. The excitation frequencies of each row must be investigated and in case of resonance condition the blade forced response must be assessed. The blade spectrum frequency characterized by all the BPF (see chapter 5.1) can be extracted from the whole compressor unsteady analysis. A runtime temporal DFT is activated during the last period of the URANS computations (when the solution is already periodic) to obtain the time Fourier coefficients. Such coefficients are extracted on the blade surface and a dedicated post-processing tool applies a spatial circumferential

DFT to extract the pressure fluctuation components in the cyclic symmetry environment. The forcing is so divided into rotating pressure waves at the same frequency but with different circumferential order. The modal analysis is then performed to predict natural frequencies and mode shapes. In this thesis, modal analyses of a bladed disk sector in cyclic symmetry have been carried out by means of the FEM ANSYS solver. Natural frequencies and mode-shapes were used to perform aerodynamic damping analyses and modal work assessments. The next step consists in determining which unsteady forcing actually excites the blade rows. The improved use of the Interference diagram (see chapter 2.2.3.3) allows to evaluate resonance condition that occurs also at harmonic indices different from the main one, by taking into account the contributes of the different nodal diameter that characterizes the exciting forcing. Once the unsteady forcing that excites the blade has been selected, the aerodynamic damping must be evaluated. Aerodynamic damping simulations (see 3.5) are performed with TRAF on a row vibrating in traveling wave manner and the aerodynamic work is directly computed by TRAF during the last blade oscillation period. Finally, the forced response analysis is computed by means of the modal work tool which takes as inputs blade mode-shape, decomposed forcing functions, and damping value to compute on the blade surface CFD discretization the scaling factor to be applied to modal displacement and stresses. A near point interpolation strategy is used to transfer blade mode-shape on the CFD blade surface discretization, that ensures a better accuracy for the modal force computation. The modal work approach ensures extremely short computational times with virtually zero computational cost. If the blade does not satisfy the HCF life assessment, the blade needs a redesign. If the exciting force must be revaluated, an unsteady computation on a reduced domain can be performed to update the unsteady pressure perturbation on the

blade surface. The reduced computational domain must include all the blade row that are involved in the generation of the exciting nodal diameter. The unsteady analysis on the whole compressor is necessary to evaluate all the nodal diameters involved but once they are selected, the use of a reduced domain is sufficient to correctly predict the investigated unsteady force.

Once the aerodynamic performance, the stall margin, and the mechanical constrains are concurrently satisfied, the 3D design process is completed and a final assessment on an engine test may be performed to verify the correct design.

The effective improvement of the result accuracy and of the blade response prediction obtained by using this steady and unsteady CFD strategy will be reported in chapter 4 and chapter 5 together with its validation.

3.2 TRAF code

TRAF (TRAnsonic Flow) is the CFD code that has been used for all the numerical simulations performed in this work. The code is a three-dimensional viscous-inviscid solver developed at the University of Florence during a project involving NASA (ICASE and ICOMP) and DEF (Department of Energy Engineering "Sergio Stecco" of the University of Florence). The code was designed for cascade flow predictions and includes several techniques to achieve computational efficiency and accuracy.

Reynolds–Averaged Navier–Stokes (RANS/URANS) equations are mapped in a curvilinear coordinate system [75] [76]. The link between the Cartesian coordinate system and the curvilinear

one is handled by means of transformation matrices and Jacobian. The turbulence closure models employed in TRAF code are the following:

1. Baldwin-Lomax algebraic model [77]
2. Baldwin-Lomax algebraic model with Degani-Schiff correction [78]
3. Mixing length algebraic model [79]
4. One-equation Spalart-Allmaras model [80]
5. One-equation Spalart-Allmaras model with Spalart-Shur correction [81]
6. Two-equation k-ω Wilcox Low-Reynolds model [82]
7. Two-equation k-ω Wilcox High-Reynolds model 1988 ver. [82]
8. Two-equation k-ω Menter SST model [83]
9. Two-equation k-ω Wilcox High-Reynolds model 2008 ver. [84]

The spatial discretization is based on a finite-volume approach, with the space discretization of the governing equations provided by starting from an integral formulation without any intermediate mapping [85] [86] [87]. The inviscid fluxes may be discretized with two different options:

- 2^{rd} order cell-centered scheme
- Roe's upwind scheme

For the first one, the flow quantities are computed by a simple averaging of adjacent cell-centered values of the dependent variables and then the fluxes can be calculated on each cell face. Artificial dissipation terms are included away from the shear layer regions to assure stability and prevent oscillations near shocks or stagnation points. The physical diffusion associated with diffusive terms is generally not sufficient away from the

wall to prevent the possible odd-even point decoupling typical of cell-centered schemes. Both scalar [85] and matrix [88] dissipation models are available in the code. To minimize the amount of artificial diffusion inside the shear layers, these terms are weighed with an eigenvalue scaling [89] [90]. As far as the upwind scheme is concerned, a higher order of spatial accuracy is achieved through a MUSCL (Monotone Up-stream-centered Schemes for Conservation Laws) extrapolation scheme (3^{rd} order spatial discretization). To avoid numerical instabilities, a TVD (Total Variation Diminishing) scheme is also applied [91].

The system of differential equations is advanced in time using an explicit four-stage Runge-Kutta scheme [85]. A dual-time stepping method [75] [92] is adopted for time-accurate calculations and the coupling between consecutive rows is handled by means of sliding interface planes. The TRAF code provides four different techniques to strongly reduce the computational cost and to speed up the convergence [76].

- **Local time-stepping**
  The use of a local maximum available time step leads to a faster expulsion of disturbances while adopting the time-marching approach. In particular, the local time step limit is computed accounting for both the convective (Δt_c) and diffusive ((Δt_d) contributions:

$$\Delta t = CFL \frac{\Delta t_c \Delta t_d}{\Delta t_c + \Delta t_d} \tag{58}$$

  where CFL is the Courant-Friedrichs-Lewy number.

- **Residual smoothing**
  TRAF code use implicit smoothing of residuals to increase the stability limit and the robustness of the basic

scheme. Lerat [93] introduced this technique in conjunctions with Lax-Wendroff type schemes and later Jameson [94] implemented it on the Runge-Kutta stepping scheme. For viscous calculations on highly-stretched meshes, the variable coefficient formulations of Martinelli and Jameson [89] and Swanson and Turkel [90] have proven to be robust and reliable.

- **Multigrid**
  The idea of multigrid is based on obtaining coarse meshes by simply eliminating mesh lines in each coordinate direction from the finer reference mesh, thus leading to a convergence speed up. The speed-up of the propagation due to the coarse grid leads to a faster expulsion of disturbances. The procedure is repeated on a succession of coarser grids and the corrections computed on each coarse grid are transferred back to the finer one by bilinear interpolations. Even if more grid levels can be adopted, usually the multigrid method is performed with a V-cycle on three grids: coarse (4h), medium (2h) and fine (h) [95].

- **Grid refinement**
  The code uses a grid refinement strategy to provide a cost-effective initialization of the fine grid solution. The Full Multigrid (FMG) procedure is obtained by the combined use of grid refinement and multigrid strategy. The solution is initialized on the coarser grid level and iterated for a prescribed number of multigrid cycles. The solution is then passed, by bilinear interpolations, to the next finer grid and the process is repeated until the finest grid level is reached [96].

The convergence evaluation is based on the residual check based on the l2 norm, defined as:

$$Q = \frac{1}{N}\sum_{n=1}^{N}\left(\sum_{i=1}^{5} Q_i^2\right)^{1/2} \tag{59}$$

where $N = n_x \cdot n_y \cdot n_z$ are mesh cells and the target for convergence is half-order above the machine accuracy (single precision).

There are five main types of boundary conditions: inlet, outlet, solid walls, periodicity and interface between adjacent rows.

- **Inlet conditions**
  The spa-wise distributions of total temperature, total pressure and flow angles are imposed at the inlet section of the computational domain, while the outgoing Riemann invariant is taken from the interior.

- **Outlet condition**
  The span-wise distribution of static pressure or a value or a value at the casing used to impose a radial equilibrium is imposed at the outlet section of the computational domain. The density and momentum components are extrapolated.

- **Solid wall conditions**
  the pressure is extrapolated from the interior grid nodes. The density and total energy are computed using no-slip and temperature conditions. The code provides two different temperature conditions: adiabatic wall and prescribed constant wall temperature. The first one

imposes adiabatic condition that are obtained by nullifying the wall temperature gradient in the normal-like direction. In the second one the user specify the constant wall temperature as a fraction of the total temperature at the domain inlet section.

- **Periodicity condition**
  The TRAF code is characterized by adopting one phantom-cell layer for each grid boundary. The periodic phantom cell values are used to impose the periodicity in circumferential direction from a blade passage to the contiguous one.

- **Interface condition between adjacent rows**
  This treatment of this boundary condition is different from steady-state to time-accurate case. The steady-state case provides the mixing-planes to handle the coupling between adjacent rows. The data are exchanged through the common interface plane of consecutive rows by an appropriate calculation of phantom cell values, keeping the spanwise distribution while averaging in the pitch-wise direction. A detailed description is reported in chapter 3.4.1. The unsteady analysis handles the coupling between consecutive rows by means of sliding interface planes. The exchange of information between adjacent blocks is obtained performing linear interpolations in both the tangential and the radial direction [11].

The code provides a multi-level hybrid strategy for parallelization on CPUs [97]. This scheme is obtained from the OpenMP and MPI parallelism. This strategy guarantees to have optimum performance in terms of computational time and cost respect to usual commercial CFD code.

The TRAF code performs aeroelastic analysis using an uncoupled method that will be described in chapter 3.5. The CFD code is capable to solve both tuned and mistuned blade row and it has been widely validated for aeroelastic computations in many previous works [98] [99] [100] [101] [102] [103] [104] [105].

3.3 Discretization

The computational grids used in this work for viscous full Navier-Stokes simulations are O-type structured grid obtained using in-house developed code. An elliptic procedure that solves the discretized Poisson equations using a point relaxation scheme is used to generate 2D grids.

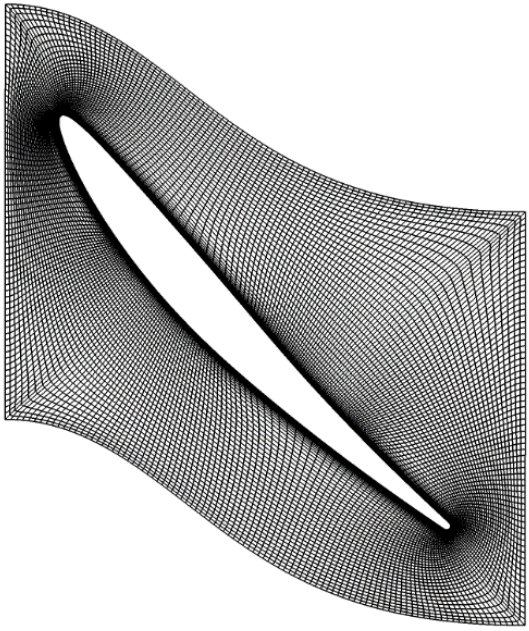

Figure 3.2 - Rotor blade-to-blade grid

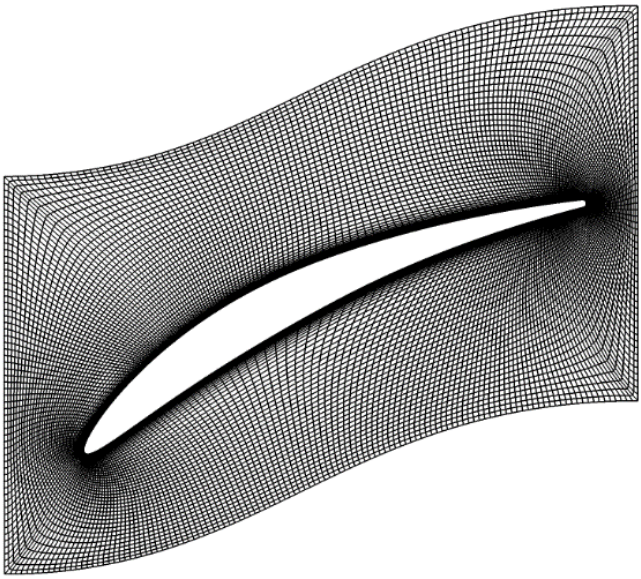

Figure 3.3 - Stator blade-to-blade grid

The grid spacing and orientation at the wall are controlled with forcing functions like the one proposed by Steger and Sorenson [106]. Viscous grids are obtained from the inviscid grids by adding lines near the wall. The grid spacing was selected to give a y^+ value lower than 2.0 for the first grid point above the wall. This condition allows a proper resolution of the laminar sublayer of all the boundary layers located in the computational domain due to the presence of solid walls. The 3D mesh (see Figure 3.4) is obtained by stacking in the spanwise direction different 2D grids. Figure 3.2 and Figure 3.3 shows an example of O-type blade-to-blade grids for rotor and stator row respectively used in this work.

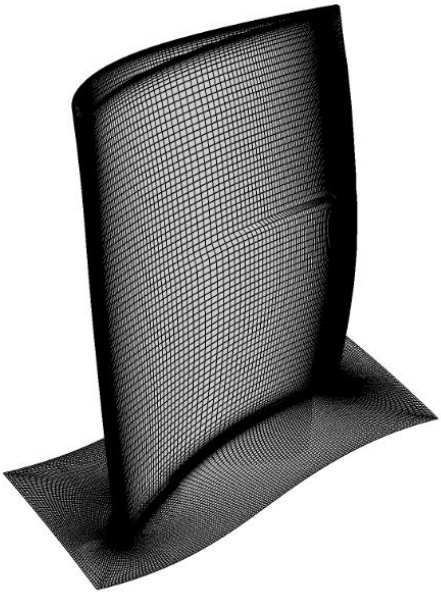

Figure 3.4 - Stator 3D mesh

The sensitivity of the converged results to the quality of the space discretization was assessed before the production runs. The investigation concentrated an intermediate stage of the investigated axial compressor, as the results discussed in chapter 4.2 showed a very complex flow field followed by the onset of flow separation. Three grid levels were considered with a total number of grid points in the range from 8×10^5 to 7×10^6 for both stator and rotor rows. The corresponding grids are referred to as coarse, medium and fine respectively. Figure 3.5 summarizes the result of the grid sensitivity analysis in terms of stator and rotor loss coefficients (see equation (20)

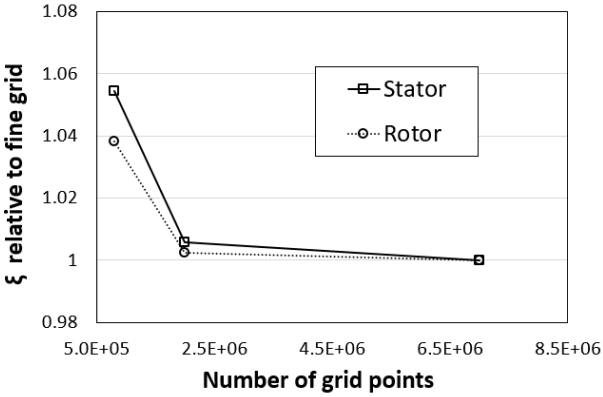

Figure 3.5 - Grid sensitivity analysis: rotor and stator loss coefficient versus grid size

Figure 3.5 reveals that the variation of loss coefficient from the medium to the fine mesh is, on average, less than 1% for both the stator and the rotor rows. Therefore, all the results presented in this thesis were obtained with the medium mesh, which was deemed to give the best compromise between computational effort and grid convergence. The full annulus domain for time accurate analyses is composed of about 2000M cells.

3.4 Aerodynamics computational setup

In this work steady and unsteady CFD computation have been performed to evaluate the axial compressor aerodynamic performance. From the unsteady simulations, the unsteady excitations have been extracted for the forced response evaluation with the modal work approach. In the following chapters the steady and unsteady computational setup will be described in detail.

3.4.1 Steady analysis

Steady state analysis has been performed on a single stage and on the whole compressor domain. The two-equation $k-\omega$ Menter SST model [30] is the turbulence closure model adopted in all the numerical simulations. The flow was assumed as fully turbulent and the mesh spacing near the wall allowed wall-integration and avoid the use of wall functions, while at the inlet both turbulence intensity and integral turbulence length scale are prescribed. A mixing-plane approach provides the steady coupling of rotors and stators. The link between consecutive blade rows can be carried out with either a one-dimensional characteristic approach or a non-reflecting treatment, as originally proposed by Saxer and Giles [107], that was adopted here. The circumferentially averaged incoming characteristic changes are calculated from flux-averaged primitive variables obtained at the exit plane of the preceding blade row. The outcoming average characteristic change is calculated from the flux-averaged pressure in the inlet plane of the downstream blade row. Spanwise cell distributions in coupled domains are matching, and the flux-averaging process is carried out at each spanwise location, so that radial profiles of quantities are retained. For real gas calculations, all the derivatives needed to determine the characteristic jumps are evaluated numerically from gas properties look-up tables. To these average characteristic jumps, the two-dimensional non-reflecting characteristic fluctuations are added at each spanwise location, so that a quasi-3D non-reflecting boundary treatment is achieved. This approach is not robust in the case the mixing plane intercepts a flow recirculation zone. In such a case, the presence of reverse flow is checked at each spanwise location, and if a patch of negative meridional velocity is detected, the boundary scheme is locally switched to a different model that directly passes fluxes resulting in a reflecting but

separation-tolerant treatment. An ideal gas model has been adopted with the c_p that varies with the temperature. The clearance region has been directly meshed keeping the nominal clearance dimension. The calculations have been carried out by assuming humid air with variable specific heats.

3.4.2 Unsteady analysis

The computational setup in terms of turbulence model closure, gas model and clearance discretization is the same of the steady state simulations. The circumferential periodicity conditions are imposed using the full annulus approach. This method is the most straightforward and accurate, but also the most expensive to compute an unsteady solution since a circumferential periodic domain must be simulated. The computational domain corresponds to the sufficient number of blades to reach the circumferential periodicity. This condition is verified when the number of blades in each row has at least one common divisor, alternatively the entire annulus must be simulated. In order to solve all the relevant frequencies, while avoiding modifications in the blade count ratio, the time-accurate simulations were carried out on a half annulus basis. The sensitivity of the converged results to the quality of the time discretization was assessed before the production runs. The sensitivity analysis to the time step was conducted on a subdomain with three rows from stator 10 till stator 11. The time step was computed by referring to stator 11 pitch, the smallest of the three rows considered for this test, that was subdivided into 25 steps, case A, 50 steps, case B, and 100 steps, case C. The results were analysed in terms of the DFT of stator 11 lift coefficient, as a measure of its unsteady response. The results summarized in Figure 3.6 indicate that the first harmonic is captured by all the three time discretizations,

but differences already arise for the second harmonic amplitude, indicating that the coarsest time step of case A is insufficient. While the intermediate time step, case B, predicts a lower content of the highest harmonics with respect to case C, it was considered sufficient to capture the most relevant unsteady phenomena that are weakly affected by the upper-order harmonics, and therefore it was adopted for all the unsteady simulations.

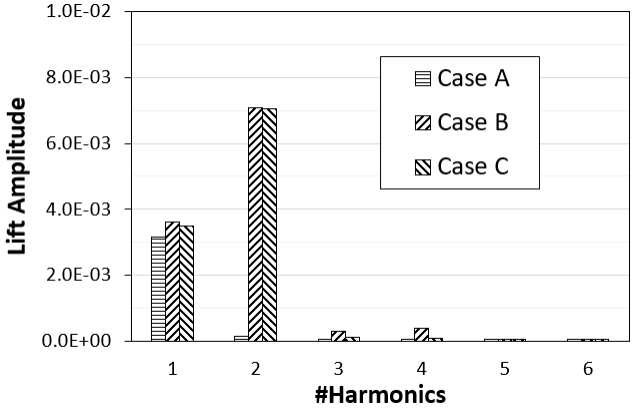

Figure 3.6 - Time-step sensitivity analysis: harmonic lift amplitude versus different number of time steps

The link between subsequent blade rows is achieved via a sliding interface approach, as already said in chapter 3.2. A buffer zone, characterized by a grid coarsening in the axial direction and higher numerical dissipation, is added at the outlet domain to avoid undesired numerical reflection of the pressure waves. This additional buffer grid at the domain exit acts as an absorbing layer, where physical outgoing waves are damped out as a result of the grid coarsening. This also reduces the effects of possible spurious reflections from the outlet boundary, as they are likewise damped while travelling back towards the interior of the domain [108]. With this technique, the amplitude of spurious

reflection entering the physical domain is negligible compared to physical outgoing pressure wave. The hybrid OpenMP/MPI parallel version of the TRAF code was used in order to speed-up the computations.

The Table 5 shows the costs and computational times for the performed simulations using Intel(R) Xeon(R) CPU E5-2670 with Clock 2.60GHz:

	Total Core	OMP	MPI	Computational time [hour]
Single Stage Steady	8	4	2	8 h
Steady whole compressor	100	4	25	24 h
Unsteady whole compressor	750	1	750	336 h

Table 5 – Computational times and costs

3.5 Aerodamping computational setup

An uncoupled method has been used in this work for the aerodynamic damping computations. This approach is shown in Fig. 3.4. A FEM modal analysis on the Computational Solid Domain (CSD) is performed to evaluate the blade eigenfrequencies and mode shapes. At the same time, a steady CFD analysis is performed to obtain the average pressure field on the profile surface. Then, the CSD grid is superimposed on the CFD grid trough a roto-translation matrix and by interpolating the values on the CFD nodes the mode shapes can be transferred to CFD domain. At this point a URANS CFD analysis may be performed applying a harmonic perturbation of CFD mesh to update the coordinates $x; y; z$ of nodes at each discrete time-step overall the oscillation period.

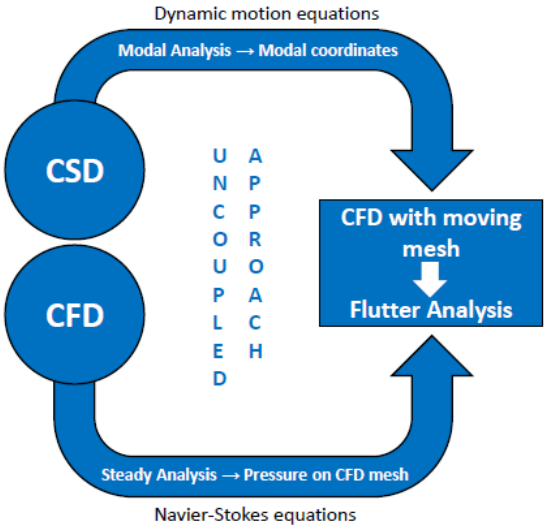

Figure 3.7 - uncoupled method outline

The blade-row vibrates in a traveling wave manner with a constant phase shift between adjacent blade passages and with the same amplitude and frequency.

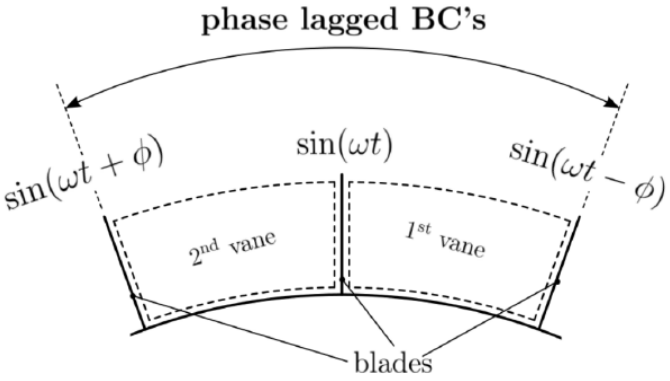

Figure 3.8 - Periodicity conditions for a phase lagged approach with a general IBPA value ϕ [98]

The unsteady equations are solved in time on the deforming mesh using a dual time-stepping technique until the flow solution becomes periodic. By performing a temporal DFT on unsteady flow quantities computed for each discrete time-step, the main temporal harmonics of the signal may be obtained.

A phase-lagged boundary conditions has been used to handle periodicity at the circumferential boundaries by means of temporal and spatial Fourier coefficients. As shown in Figure 3.8, the computational domain is composed by two passages per row to make the approach faster and more robust [98], thus enhancing the convergence and solution periodicity. Each quantity directly depends on time, so that a generic solution variable at a periodic boundary $f(t)$ can be expressed by Fourier series in time with a finite number of time-harmonic coefficients as below:

$$A_0 = \frac{1}{T}\sum_{j=1}^{NP} f(t)\Delta t \tag{60}$$

$$A_n = \frac{\omega}{2\pi}\sum_{j=1}^{NP} f(t)\sin(n\omega t)\,\Delta t \tag{61}$$

$$B_n = \frac{\omega}{2\pi}\sum_{j=1}^{NP} f(t)\cos(n\omega t)\,\Delta t \tag{62}$$

where A_0, A_n, B_n are the Fourier series coefficients, n is the harmonic number, ω is the natural pulsation, T is the blade oscillation period, NP is the time-step number on the oscillation period and t is the time-step. The code stores in memory A_0, A_n, B_n constants for a prearranged harmonic number and uses it to reconstruct fluid properties through a suitable phase lag. An acceleration of the convergence is reached in TRAF code by

updating the coefficients even during the oscillation period through a moving average scheme.

Flutter stability is assessed by computing the critical damping ratio from the aerodynamic work by means of the Energy Method [109]. In this method the aeroelastic stability is estimated by means of the energy transfer between fluid and structure during one period of blade oscillation. This method is based on the assumption that the effects of the aerodynamic forces on the structural dynamic properties can be considered negligible. It means that the natural frequencies and mode shapes are not influenced by the unsteady aerodynamic blade loading. Usually, this assumption is completely satisfied because compressor blades are typically characterized by having a high mass ratio and a significant frequency gap between different eigenmode families. As already said in chapter 2.2.2, the unsteady pressure is numerically integrated over the blade surface and over time to compute the aerodynamic work. The sign of the aerodynamic work asses the flutter stability:

- A positive aerodynamic work means that the energy is transferred from the flow to the blade and the vibration is amplified over time.
- A negative aerodynamic work means that the energy transfer is from the blade to the flow and so the oscillations are damped.

4 Aerodynamic validation

This chapter illustrates the validation of the steady and unsteady CFD strategy in terms of aerodynamic performance prediction through a direct comparison with a detailed experimental data set of an 11-stage industrial compressor for Heavy Duty Gas Turbine (HDGT). The results shown in this chapter are taken from the paper of Burberi et al. [110]. The first part describes in detail the test rig, which was also used for aeromechanical measurements. The comparison with experimental data, reported in the second part, shows how the use of unsteady simulation leads to a significantly increase in the result accuracy. The difference between the steady and unsteady results has been investigated in detail in order to understand how to integrate the two approaches. Finally, the single-stage steady approach with inlet time-average spanwise profile is validated.

4.1 Test rig

The experimental campaign was carried out by Nuovo Pignone S.r.l.. The 11-stage axial compressor under analysis is in a design space where aero-engines and light industrial gas turbine load and flow coefficient parameters are blended to optimize performance with a reduced number of stages. This compressor was tested in-house in a dedicated facility driven by a PGT25 [111] gas turbine. The full-scale set-up of Figure 4.1 replicates real operating conditions and includes bleed ports and extractions designed to purge and cool the turbine hot-gas path.

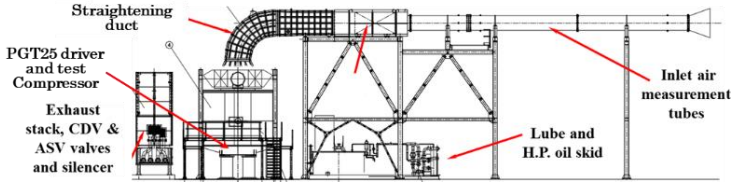

Figure 4.1 - Overall test facility

The compressor was throttled at the inlet to reduce the power requirements, while the exit throttle was adjusted to sweep across different operating conditions. The compressor was equipped with variable inlet guide vanes and two rows of variable stator vanes. A total of 583 test points across corrected speeds in the range 20-108% allowed a full characterization of the compressor map. Measurements include inlet, outlet and extractions mass flow rates, stagnation pressure and temperature, with accuracies of 0.85%, 0.05%, and 2°C respectively.

Figure 4.2 - Instrumented stator rows

The stator rows leading edges are instrumented with stagnation pressure and temperature probes, as visible in Figure 4.2, while static pressure taps are available at casing upstream and downstream each stator row. Figure 4.3 shows a sketch of the 11-

stage compressor meridional cross section in which the overall number of measurements includes shroud static pressures in 22 axial positions, 118 stagnation pressures, and 106 stagnation temperatures along the instrumented stators leading edge, with an accuracy of 0.12%, 0.05%, and around 2°C respectively. The number of spanwise probes reduces from six in the front rows to three in the back rows. Each rotor row tip clearance was measured at runtime.

All the compressor airfoils were instrumented with strain gages. The Rotor 7 scrutinized in this thesis (see chapter 5.2) was instrumented with two wire resistance strain gages constructed of platinum/tungsten alloy placed in the positions and orientations shown in Figure 5.7. The gages were attached with a thermal spray process, and the grid dimension was 3.18 x 1.57 mm. The uncertainty in the position of the gage was ±0.75 mm, while the uncertainty in the orientation was ±5 deg. The gages were installed on different blades.

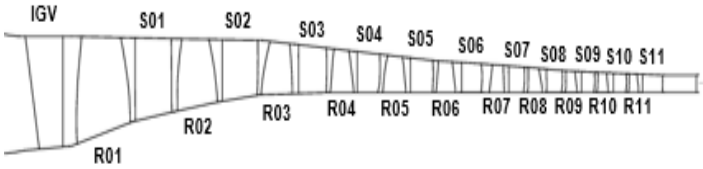

Figure 4.3 - Meridional cross section of the 11 stage axial compressor.

4.2 Measured and predicted stage-by-stage speedlines

Several RANS and URANS analyses have been performed varying the back-pressure, in order to cover the complete speedline at Nc=100%. Figure 4.4 compares test data with steady and

unsteady results in terms of total-to-total pressure ratio and inlet mass-flow of the overall compressor. The pressure ratio PR is normalized with respect to the measured value at design point condition, while the mass-flow rate is normalized with respect to the design point value taken from measurements or predicted by steady and unsteady CFD. This normalization was chosen to directly compare the shapes of the characteristic curve considering that the predicted mass flow error is less than two percent. The stall margin is defined as follow:

$$\left(\frac{PR_{stall} - PR_{design}}{PR_{design}}\right)\% \tag{63}$$

The dotted curve in Figure 4.4 is obtained interpolating the test data and it shows a stall margin equal to 19%. A marked improvement of the agreement between test data and predictions is visible when switching from steady to unsteady computations.

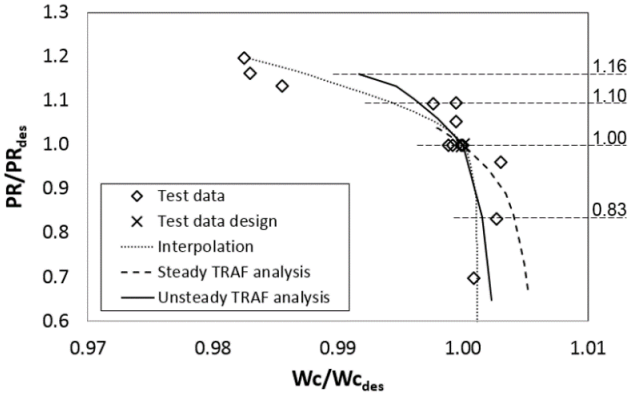

Figure 4.4 - Overall compressor speedline at 100% speed (Test, RANS, URANS).

The curve obtained with steady calculations (thick dashed line) presents a lower slope moving right of the design point as compared to the trend of test data. Moreover, the computations

have difficulty to converge as soon as the pressure ratio grows slightly above the design point and, therefore, the predicted stall margin is less than three-five percent. Conversely, the URANS prediction shows an improved agreement in comparison with experimental data. The computed stall margin, defined above, is around 16%, only 3% short with respect to experimental data. Still, the predicted speedline slope left of design point is slightly flatter than what a simple interpolation of the measurements suggests. In order to have a better understanding of the overall compressor speedline prediction, Figure 4.5 compares steady and unsteady results in terms of stage pressure rise and stage inlet through flow velocity at aero design point and for an additional condition at lower pressure ratio. The stage pressure rise is normalized with respect to the inlet absolute isentropic dynamic pressure, while the stage inlet through flow velocity is normalized with respect to the through flow velocity at the compressor inlet section. The lower set of curves in Figure 4.5(a) refer to PR=0.83 for which steady and unsteady predictions are very similar and in good agreements with the measurements. Figure 4.5(b) shows only moderate differences in through flow velocity at the same PR. On the contrary, at the aero design point (upper set of curves and symbols), a clear mismatch arises. The steady calculation predicts lower pressure ratio for stage 10 and 11 with respect to the unsteady results, that in turn are in excellent agreement with data. The through flow velocities predicted by RANS deviate as well from the ones obtained by URANS. It is worth noting that at design point RANS and URANS predict the same overall pressure ratio but the stage work is differently redistributed. In fact, RANS loads stages 4 to 8 more than URANS to compensate for the lower load of stages 10 and 11. A corresponding overall behaviour is visible in the through flow velocity.

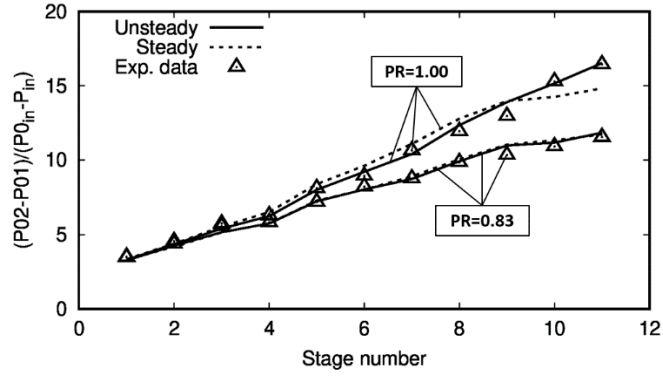

(a)

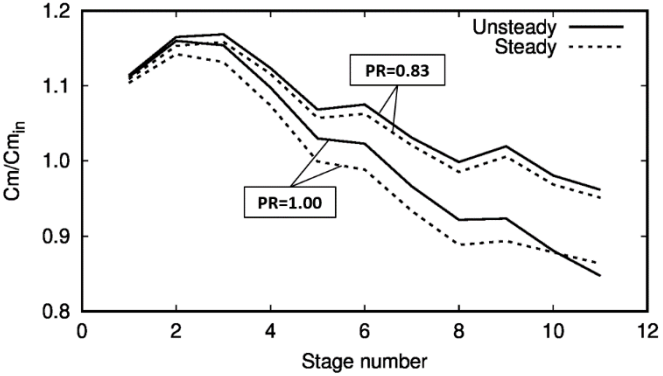

(b)

Figure 4.5 - Comparison of stage pressure rise (a) and stage inlet through flow velocity (b) between steady and unsteady simulations at ADP and PR=0.83

The speedlines of stage 8 and 11 in terms of total-to-total pressure ratio and inlet reduced mass flow (quantities are normalized with respect to the operating condition predicted by the unsteady analysis at design point) shown in Figure 4.6 confirm the results seen so far. The unsteady predictions reveal a good agreement with data along the entire operating curve, while the steady predictions are unable to reach the left limit neither in

terms of reduced mass flow nor in terms of pressure ratio. Remarkably, for low overall pressure ratio (PR=0.83) both RANS and URANS predictions are similar and sit both on top of the experimental curve.

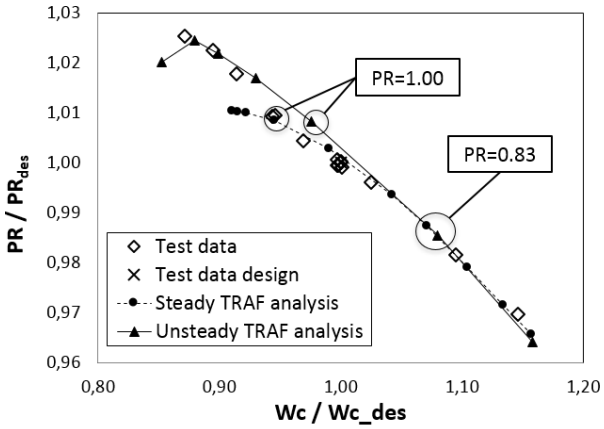

(a)

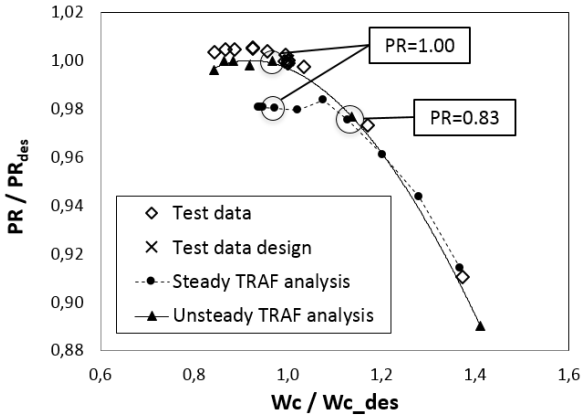

(b)

Figure 4.6 - Measured and predicted speedlines of stage 8 (a) and stage 11 (b)

4.2.1 The spanwise profiles and their impact on stage matching

The strong impact of spanwise profiles of total pressure and total temperature on stages matching was discussed by Cumpsty [56] who described the progressive profile evolution from compressor inlet to discharge. As shown in [13] a time-accurate analysis predicts spanwise mixing in better agreement with measurement. The steady and time-averaged spanwise distributions of total pressure from front-to-back stages of Figure 4.7(a) do not show large differences and they are both in excellent agreement with test data for low pressure ratio (PR=0.83), while the re-matching of stage loading at the design point is evident in Figure 4.7(b).

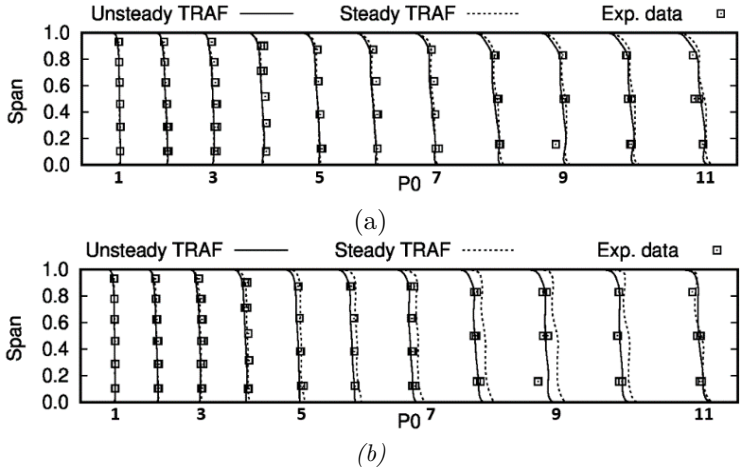

Figure 4.7 - Total pressure profiles at PR=0.83 (a) and ADP (b) at stator inlet (Test, RANS, URANS)

The effect of spanwise mixing is particularly evident in the distributions of stagnation temperature reported in Figure 4.8. The time-averaged unsteady profiles are smoother and clearly in better agreement with measurements than the steady ones,

especially near the endwall regions of the back stages. As expected, the difference grows from front to back of the compressor.

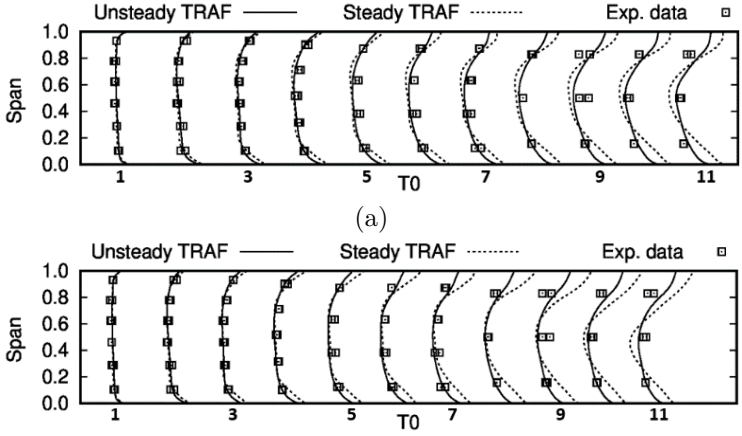

Figure 4.8 - Total temperature profiles at PR=0.83 (a) and ADP (b) at stator inlet (Test, RANS, URANS)

Figure 4.9 compares steady and unsteady spanwise distributions of meridional velocity. At PR=0.83 the steady predictions present a higher value in the tip region and lower in the hub region with respect to the unsteady simulation, as evidenced by the black arrows. This suggests that RANS predicts a stronger tip flow with a different radial distribution of mass-flow rate. The same trend holds at ADP, but only up to stage 8-9, as for the back stages the steady state simulations predict a higher blockage near the tip region and the mass flow tends to be redistributed towards lower radii compared to the time-averaged results.

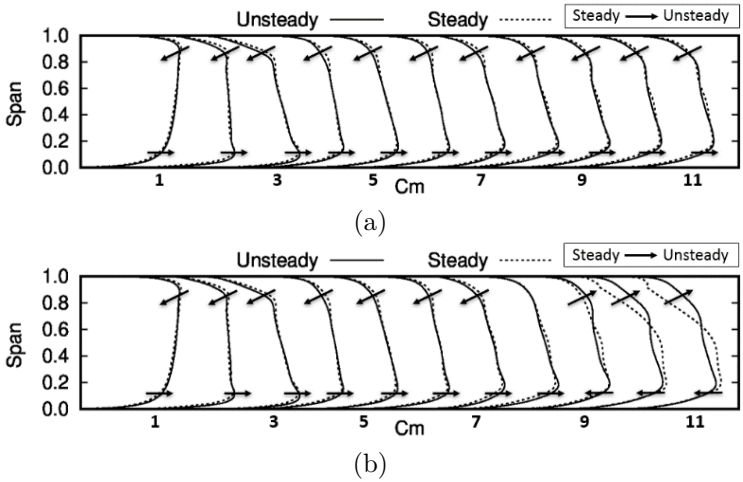

Figure 4.9 - – Meridional velocity profiles at PR=0.83 (a) and ADP (b) at stator inlet (RANS, URANS)

Such behaviour is related to the tip clearance vortices that create a stronger blockage in the casing region in the steady state analysis. The mixing plane method may predict unrealistic blockage in presence of negative axial velocities from the upstream. Thankfully, around the design point the steady simulations show no flow reversal, with only a very small negative axial velocity in the tip vortex core leaving stage 9. So, the differences between steady and unsteady simulations are not to be attributed to a malfunction of the mixing plane. Figure 4.10 shows the work coefficient (see equation (27)) which is computed by spanwise integration along streamlines. This definition provides a physically sound evaluation of such a quantity that accounts for the changes in stagnation temperature, peripheral and throughflow velocities across the stage. Each spanwise distributions of work coefficient is normalized with respect to its own average value in order to directly compare the profile shape. At both PR=0.83 and 1.0 the work coefficient is higher in RANS

towards the endwalls and this behaviour contributes to the underestimation of the stall margin by the steady state approach. Large discrepancies between steady and unsteady results near endwalls are not surprising.

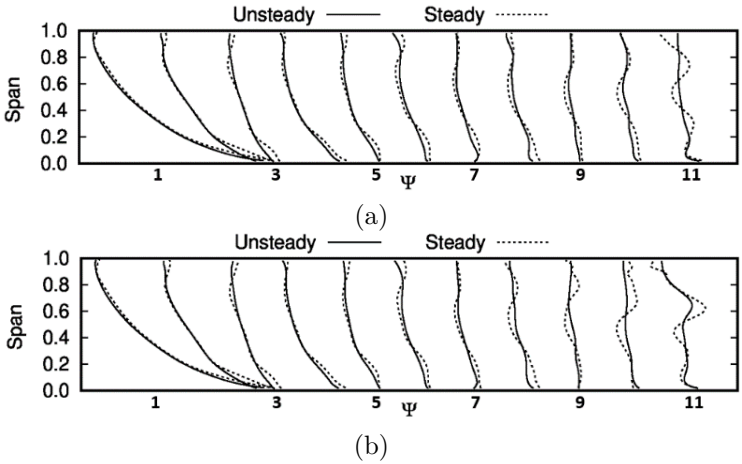

Figure 4.10 – Work coefficient profiles at PR=0.83 (a) and ADP (b) at stator inlet (RANS, URANS)

Streamwise vorticity associated with secondary and tip leakage flows is transported downstream of the blade trailing edge and interacts with the downstream blade rows. While the time-accurate analysis captures both the transport and interaction phenomena, this is not the case for steady state calculations, where the mixing-plane treatment filters out any circumferential distortion. At PR=0.83 the wavy spanwise shape of the work coefficient profile predicted by RANS gradually grows from front to back to reach its maximum at stage 11, while the time-averaged unsteady distribution is much smoother all across the compressor. At PR=1, steady and unsteady CFD predict similar stage 11 spanwise work coefficient profiles. Still, in RANS this is due to a carry-over from the upstream stages as the wavy

shape grows from front to back, whereas in the unsteady predictions only stage 11 shows an uneven spanwise load distribution.

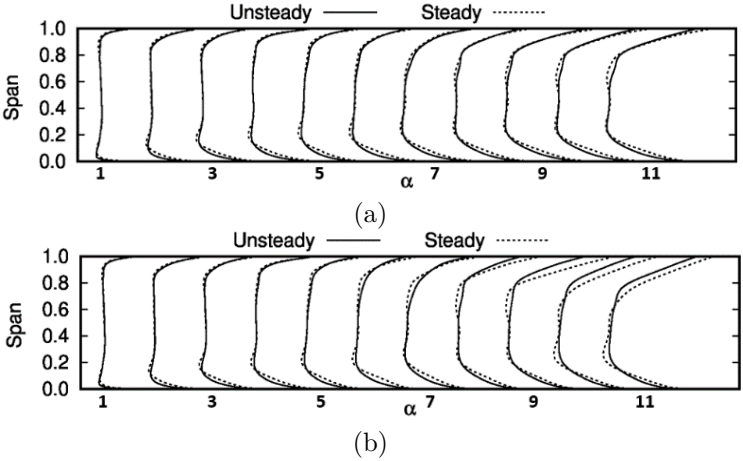

Figure 4.11 – Absolute flow angle profiles at PR=0.83 (a) and ADP (b) at stator inlet (RANS, URANS)

The stationary absolute flow angle profiles at stator inlet are slightly higher at endwalls with respect to the unsteady simulation visible in Figure 4.11, except for the back stages at PR=1.0 where the differences are more pronounced. This behaviour is linked to the steady work coefficient profiles that have higher values towards the endwalls, as mentioned above. Until the local incidence in the tip region is unable to provoke a flow separation on the stator suction side, the steady analysis predicts a stage matching that is comparable to the unsteady one (PR=0.83). On the other hand, when predicted local incidences are too high for the following stator (PR=1.0, stage 9), a flow separation occurs on stator row. This generates a snow-ball effect whereby subsequent stages are no longer able to work properly. At design point, the increase of the flow angle approaching the stator

leading edge at tip on the three back stages predicted by RANS as opposed to URANS is mainly due to the drop in C_m at tip visible in Figure 4.9.

The results shown in this chapter suggest that as long as the differences in the spanwise profiles are small RANS and URANS predict similar stage-matching that fits with the test data. When increasing the PR further RANS predicts profiles that are the consequence of incorrect stage loadings.

4.2.2 Non-dimensional speedlines

Figure 4.5 shows that steady and unsteady computations predict different stage pressure ratios and through flow velocities and, in practice, different stage matching. Moreover, at PR=1.0 the discrepancy is more pronounced than at PR=0.83, indicating that the level of aerodynamic loading plays a role. In presence of a significant mismatch, the comparison of steady and unsteady predictions at single-stage level may be misleading as the same stage would see different operating conditions resulting from the different load distributions predicted by the two approaches.

A possible strategy to remove the effect of mismatch is to shift the comparison between steady and unsteady results at the level of non-dimensional characteristic curves for each stage. In this section plots of work coefficient ψ (see equation (27)) versus the flow coefficient ϕ (see equation (26)) are reported for stages 1, 4, 8 and 11 (Figure 4.12, Figure 4.13, Figure 4.14 and Figure 4.15 respectively). The curves are scaled by the unsteady design values, which differ from stage to stage.

The axes scales are kept the same to highlight the increasing levels of off-design from front to rear stages while the overall compressor is sweeping the pressure ratio at design speed. At design speed the back-end block prevents the front-one from deviating too much from its design point. A lower speed would be more suitable to explore first stages in a wider range, but this is beyond the scope of this thesis.

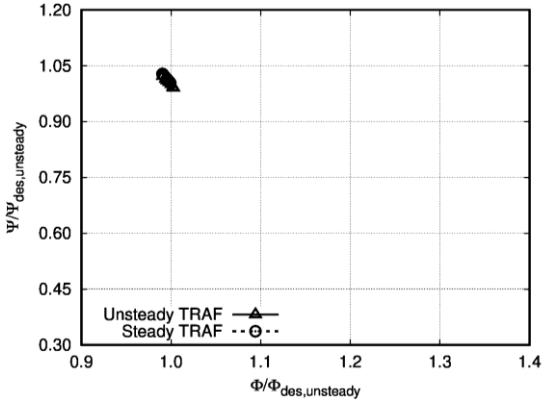

Figure 4.12 - Stage 1 speedline. Steady and unsteady results

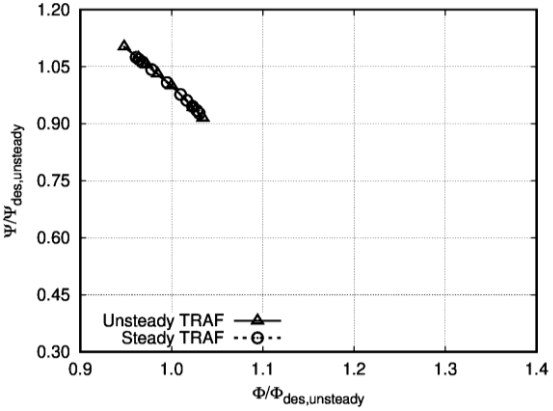

Figure 4.13 - Stage 4 speedline. Steady and unsteady results

Figure 4.14 and Figure 4.15 show that steady and unsteady non-dimensional speedlines differ more as the flow coefficient decreases, while at high flow coefficients the curves show the same trend. The same figures also show the different points, corresponding to different ϕ-ψ combinations, at which stages 8 and 11 are operated according to RANS and URANS for the same overall compressor pressure ratio of 0.83 and 1.0. For PR=1.0 the stationary point sits on a curve that differs from the curve that fits to the unsteady points, and this is a proof of the different matching of stages as predicted by steady versus unsteady runs. For PR=0.83, the corresponding points on solid and dashed curve are very close. From this point on increasing ϕ, the same good matching is expected. The reason why the agreement between non-dimensional speedlines deteriorates on the left must be sought in the increasing level of aerodynamic loading of rotors and stators. In critical regions such as the tip of rotors, this stresses the capability of the steady approach that might also converge to flow patterns significantly different from unsteady predictions.

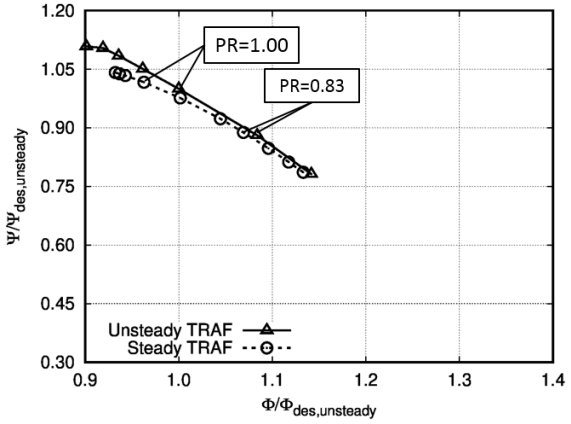

Figure 4.14 - Stage 8 speedline. Steady and unsteady results

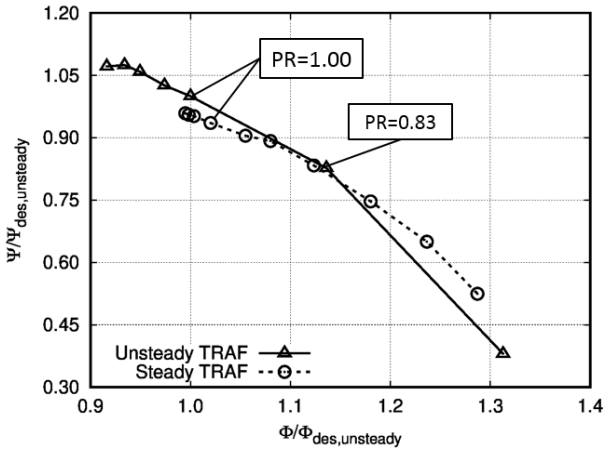

Figure 4.15 - Stage 11 speedline. Steady and unsteady results

As mentioned in the previous section, the incidence predicted by the steady approach might exceed the maximum levels tolerated by a given stator or rotor. In this case, the steady runs will predict an earlier stall as compared to the unsteady approach. Other computational problems may occur also at flow coefficients higher than the design value where, rather than flow separation, shock-waves may arise in the back stages. If this happens the back stages may operate in the so-called "fourth quadrant" with positive flow coefficients and a net pressure drop. Such flow does represent a challenge for steady computations and an anticipated right limit could be predicted.

4.2.3 The impact of unsteadiness

The ability of URANS to capture the unsteady stator-rotor aerodynamic interaction is the main driver of its superiority with respect to RANS. Such interaction is driven by the periodic impact of incoming wakes on the downstream blades that may

delay stall, as documented by Leggett et al. [17] who demonstrated how both LES and RANS capture this effect, although with some differences. Nevertheless, in [17] only the midspan section was scrutinized, while the majority of the stall driving phenomena arise in the proximity to the endwalls. The current simulations revealed how the differences between steady and unsteady results are relatively small in the front stages, and grow gradually while moving towards back stages, and it is around stage 9 where the differences become quite large.

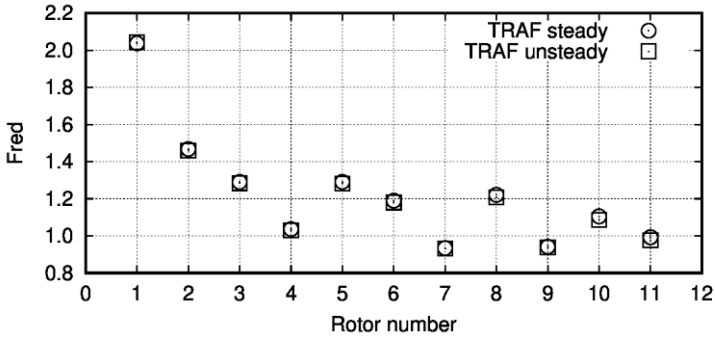

(a)

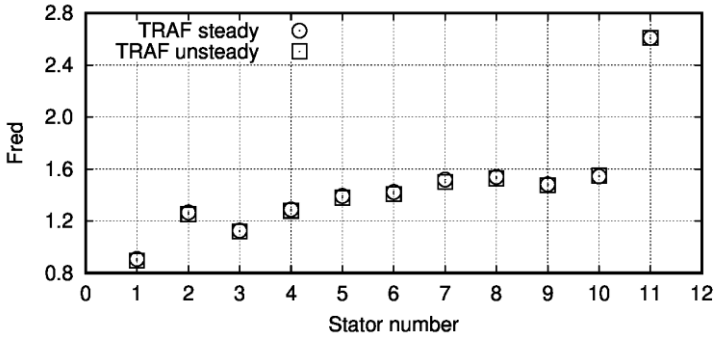

(b)

Figure 4.16 - Rotor (a) and stator (b) Fred at design point

To determine the possible reasons for the observed differences, Figure 4.16 shows the reduced frequency, F_{red}, defined as:

$$F_{red} = \frac{u}{pitch-upstream} \times \frac{chord}{c_{exit}} \tag{64}$$

using values at midspan, as seen by rotor and stator rows at design point, where RANS and URANS already predict different performances. Notably, F_{red} is unable to show substantial differences between steady and time-averaged unsteady results regardless of the operating point. While the fundamental source of deterministic unsteadiness (F_{red}) does not seem to be affected by the operating point, it is desirable to analyze the airfoil lift fluctuation range for three operating conditions to dissect the presence of non-deterministic unsteadiness due to the presence of local intermittent stall.

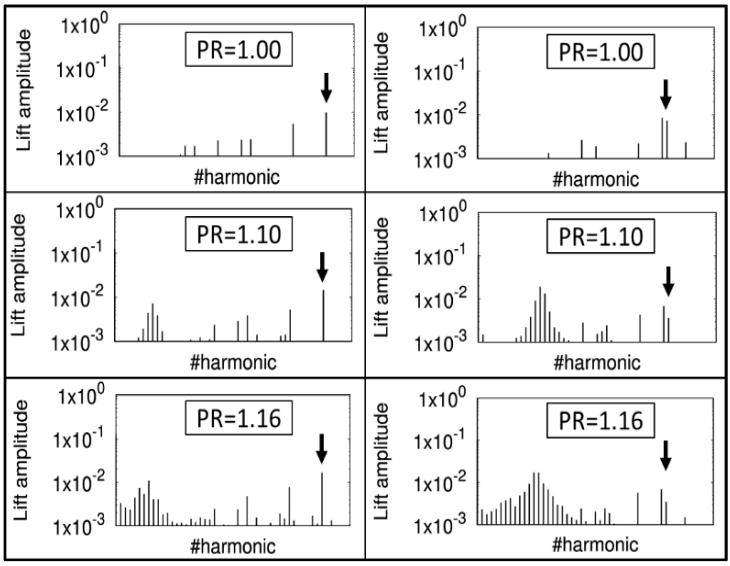

Figure 4.17 - DFT of stage 11 rotort (left) and stator (right) lift for three operating conditions (PR=1.00, PR=1.1 and, PR=1.16).

Figure 4.17 shows the DFT of stage 11 rotor and stator lift for three pressure ratios, the position of which on the overall and single-stage speedlines can be found in Figure 4.4 and Figure 4.15 respectively. The plots concentrate on the low frequencies. The presence of a deterministic unsteadiness that holds approximately constant in the three operating conditions for both stator and rotor is witnessed by the vertical segments that refer to specific harmonics driven by both wakes and potential effects. In particular, the black arrows indicate the first harmonic from the upstream row. The DFT at PR=1, corresponding to the design point, does not show low frequencies that, conversely, appear clearly for the two other operating conditions at higher pressure ratios.

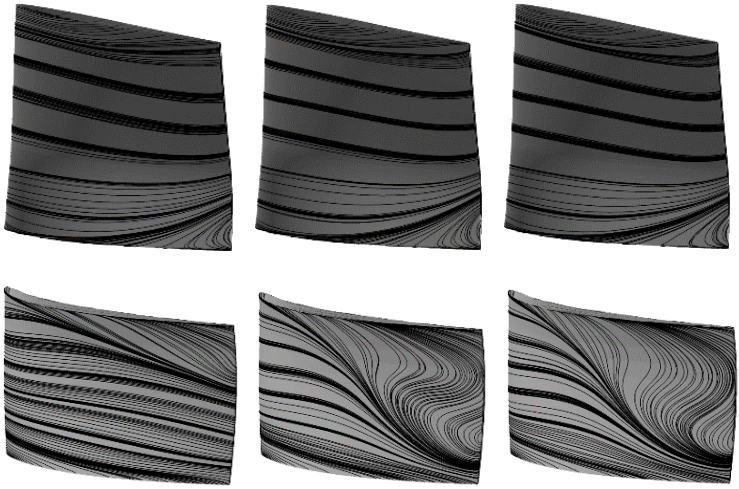

Figure 4.18 - Streamlines on the suction side of rotor (top) and stator (bottom) of stage 11 for three pressure ratios (PR=1.00, PR=1.1 and, PR=1.16). Flow is left to right.

The low frequencies are the strongest when moving further to the left at PR=1.16. The low-frequency portion of the spectrum grows in intensity and the frequency signature widens, a clear indication of the onset of a stall.

To investigate further what was observed in the DFT, Figure 4.18 shows the streamlines on the suction side of both rotor and stator of stage 11 extracted from the time-averaged multistage URANS. The plots refer to three operating conditions with increasing pressure ratio from design point. The rotor suction side shows a mild hub corner stall the size of which is remarkably constant for the three conditions, as well as the flow pattern in the proximity to the blade tip. The stator suction side at the design point shows a stable secondary vorticity at tip that grows in size and spanwise penetration with the onset of a separation when moving to higher pressure ratios. This suggests that the low frequencies visible in the rotor lift DFT are not caused by a local aerodynamic phenomenon, rather they are provoked by the back-pressure fluctuations caused by the intermittent separation in the downstream stator.

To determine the relative importance of rotor and stator on the onset of this low-frequency unsteadiness, Figure 4.19 shows the stator and rotor lift RMS and time-averaged values as predicted by URANS for three operating points, in which PR=1 refers the nondimensional design pressure ratio. The plot shows how each rotor and stator lift grows while moving left approaching the stall point, as expected. URANS allows to determine the level of lift unsteadiness for the three operating points under investigation. Low levels of RMS are driven by the simple adjacent blade rows interaction, but when the RMS level increases this is the clear sign of additional unsteadiness driven by local inter-

mittent separations. While rotor rows are all quite healthy, stators 5, 8, and 11 show an evident growth of the unsteadiness level when moving left of the design point at PR=1.13. Figure 4.19 shows that RMS grows due to the insurgence of low frequencies, the indication of a local stall, as visible in Figure 4.18 for stage 11 stator row.

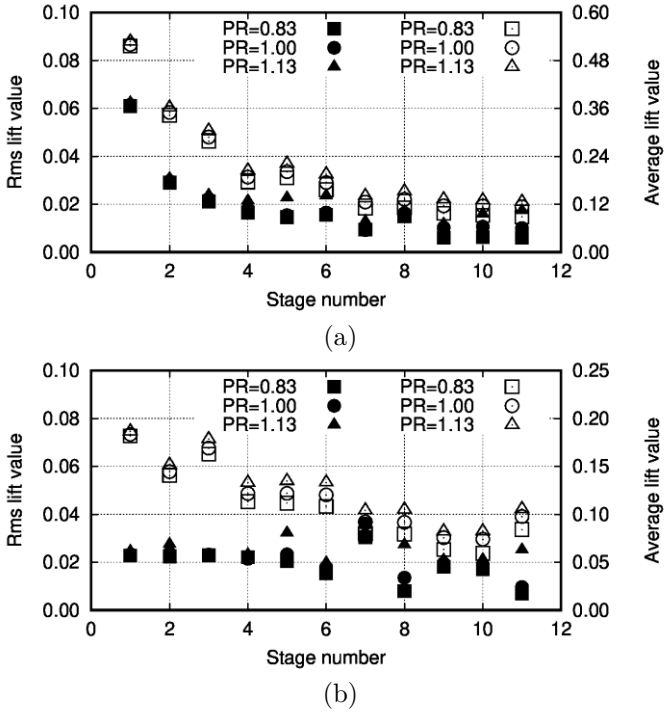

Figure 4.19 - RMS (hollow symbols) and average (solid symbols) lift of rotors (a) and stators (b) for three operating conditions.

The different trends in the lift RMS are an evident indication that the compressor aerodynamic limiting components are the

stators. Consider that the higher value of the pressure ratio examined here cannot be reached by a steady mixing-plane calculation as the speedline rolls-over for PR < 1.1.

4.2.4 Single stage steady approach for design

With a somewhat clearer picture on the growth and propagation of unsteadiness, to determine its true impact on the capability of a given stage to operate left of design, it was decided to conduct a simple numerical test selecting one operating point where the unsteady simulations provide a satisfactory statistical convergence and the time-averaged results are in good agreement with experiments. Rather than running the full compressor, it was convenient to perform the steady simulation of one single-stage with the boundary conditions coming from the pitchwise-averaged and time-averaged spanwise profiles of the multistage unsteady runs. In particular, pitchwise-averaged and time-averaged profiles of stagnation pressure and temperature, pitch and yaw angle, turbulence intensity and frequency were set at inlet, while the static pressure distribution was specified at stage exit. For the sake of brevity, it will not be rewritten that the input profiles are also pitchwise-average. As design iterations are performed stage-by-stage, this test is important to determine if and how a single stage run is accurate and reliable enough to drive design improvements. To select the single-stage to perform such verification, Figure 4.5 shows the stage pressure ratio and inlet through flow velocity at midspan predicted by the steady and unsteady simulations for the design point and an additional point at a lower overall pressure ratio. It was not possible to compare steady and unsteady results left of the design point as RANS were unable to converge for pressure ratios significantly above the design value.

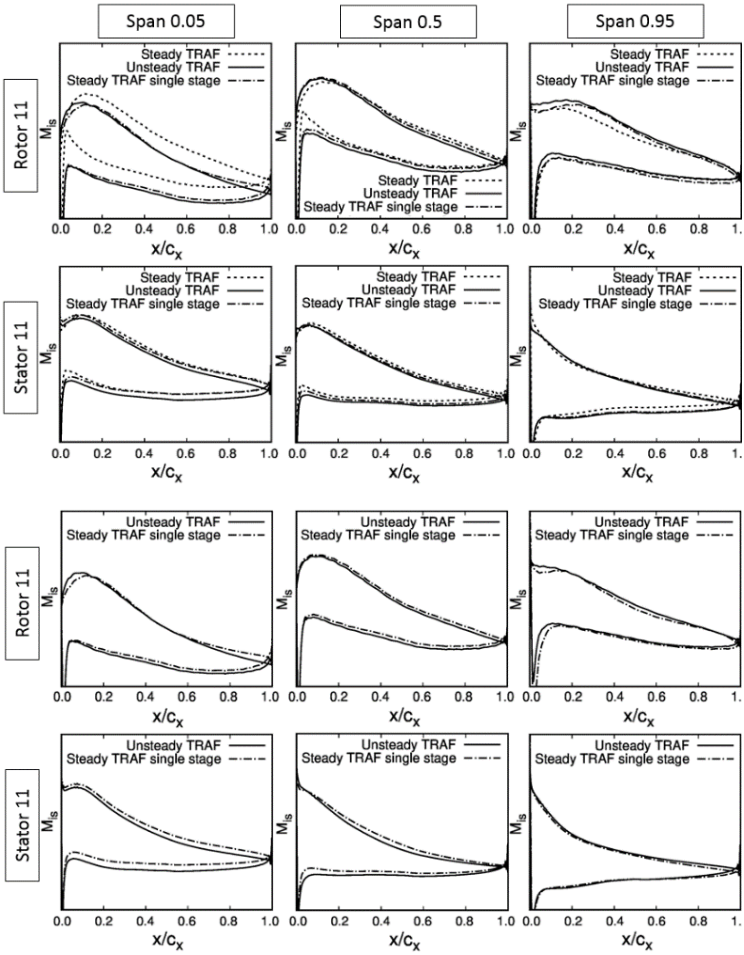

Figure 4.20 - Isentropic Mach number distributions on stage 11 rotor-stator at three span-heights (5%, 50%, 95%) for PR=1 (top 6 figures), and PR=1.1 (bottom six figures).

While right of the design point steady and unsteady simulations substantially coincide, already at design point stage 10 and 11 show remarkable differences. In particular, Figure 4.5 shows

that at design point the steady calculation predicts lower pressure ratios for stage 10 and 11 with respect to the unsteady results. The overall steady pressure ratio is reached by a stages rematch that grows stage loads above the unsteady results for stages 4 to 8. Stage 11 shows the largest difference between steady and unsteady results at design point, and therefore the unsteady versus steady with time-averaged inlet profile analysis concentrated on this stage. Figure 4.20 shows stage 11 isentropic Mach number distribution along rotor and stator profiles at three span heights for PR=1 and 1.1. The PR=1 plots compare the multistage steady predictions with the time-averaged unsteady and with the single-stage steady calculation with time-averaged inlet profiles, while at PR=1.1 the multistage steady calculations are absent as they do not converge. At design pressure ratio the steady calculation predicts an evident hub blockage due to a local stall that provokes a migration of the flow away from the hub and reduces the incidence at midspan, while the unsteady and the single-stage are very well aligned and predict a more regular spanwise load. The discrepancies fade out on the stator, although they are still visible at the hub section. This is at variance with what the unsteady calculations show, where the rotor is in good shape, while it is stator 11 that stalls first (see Figure 4.18). Moving to PR=1.1, stage 1 plots reveal only a very marginal deterioration of the agreement between multistage unsteady and single-stage steady. This suggests that enforcing the time-averaged inlet profiles extracted from the multistage URANS to the single-stage RANS is enough to predict the performance of stage 11. Figure 4.21 confirms this surprising result as, at $\phi/\phi_{des} = 1 - PR = 1$, the time-averaged unsteady performance are almost indistinguishable from the steady calculation in which the steady inlet profiles are the multistage time-averaged inlet profiles, while the multistage steady

deviates as illustrated in Figure 4.14 and Figure 4.15. To determine if this conclusion holds in other operating points the same exercise was repeated for few additional points for both stage 8 and 11 respectively. In Figure 4.21 the agreement between the two sets of predictions is good for stage 8, while it slightly deteriorates left of the design point for stage 11.

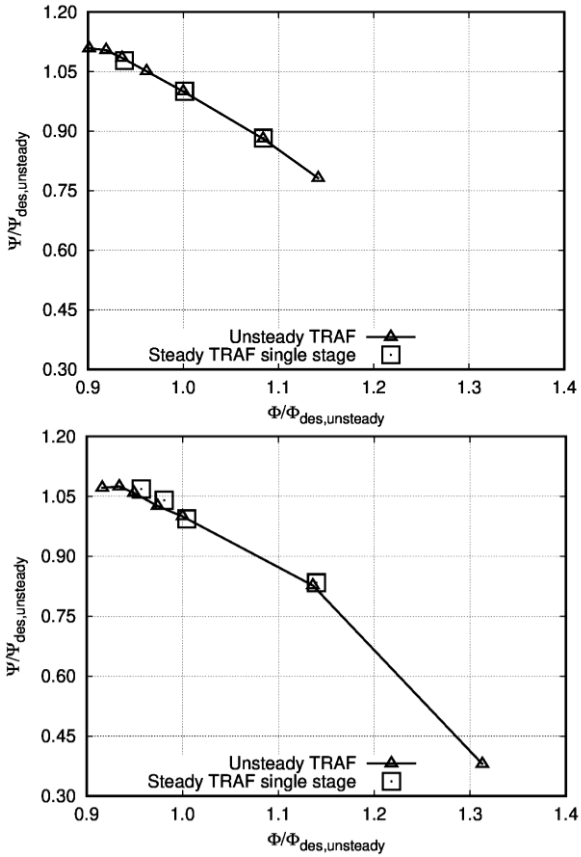

Figure 4.21 - Comparison of stage 8 (top) and stage 11 (bottom) speedlines from multistage unsteady and single-stage steady

Nevertheless, it is remarkable that according to steady multistage CFD, stage 11 could not be operated left of the design point, while with the time-averaged inlet profiles this stage remains stable with RANS much longer. This numerical experiment suggests that it suffices to enforce the time-averaged inlet profiles with a steady calculation to converge to almost the same result of the full multistage unsteady CFD. A closer look at Figure 4.7 through Figure 4.11 reveals large differences between the steady and time-averaged unsteady spanwise profiles responsible for the growth of endwall incidence in the steady calculations and the consequent earlier stall. In particular, Figure 4.22 compares stage 11 inlet and exit profiles extracted from multistage RANS and URANS. The analysis of the speedlines and of the stage boundary conditions suggests that it is not only the unsteadiness per se that keeps the boundary layers attached when moving left to the design point, as suggested in [17], but rather it is the impact of unsteadiness on the spanwise profiles that dictates the operability of each stage.

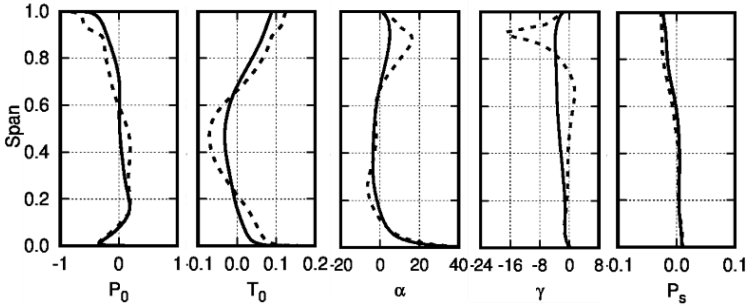

Figure 4.22 - Stage 11 inlet normalized stagnation pressure, P0, and temperature, T0, pitch and yaw angles, and exit static pressure profiles extracted from multistage RANS (dashed), and URANS (solid).

The discussed results can be summarized as follows. The simulations proved how the URANS approach is substantially superior to RANS, as the latter predicted the stall onset around the measured design point, while the former allowed to get much closer to the observed left limit. The comparison with the measured inter-stage stagnation pressure and temperature spanwise profiles confirmed the superiority of the unsteady approach, especially for what concerns the stagnation temperature. The match between stages from front to back suggested that steady and unsteady computations may give similar overall results, but with notable differences in the stage load distribution. The stage load distribution was identified as one of the root causes of the early stall predicted by RANS as opposed to URANS. To determine the main driver of URANS superiority, single-stage steady runs performed on stage 8 and stage 11 with inlet conditions extracted from the time-averaged companion multistage URANS suggested that the spanwise profile shapes are the main driver for the correct prediction of stage performance and match. It is common understanding that in-coming periodic wakes may delay compressor blade stall at midspan. Nevertheless, as axial compressors operability is generally limited by endwall regions, this stabilizing effect may not be as relevant as it was thought so far. The simulations, and their match with the measured speedline, suggest how unsteadiness is responsible for a stage re-match through the deformation of the inter-stage spanwise profiles. Therefore, it is possible to conclude that unsteadiness predicted by URANS does not only delay stall due the stabilizing effect of intermittent incoming wakes, rather it is responsible for a remodulation of the spanwise profiles that guarantees a good match with data, at least for the compressor

under investigation. Finally, the single stage steady run analysis has implications relevant to the execution of design iterations. Design iterations are generally carried out by RANS on single stages enforcing fixed inlet and exit conditions to guarantee the match with the upstream and down-stream stages. Still, the computational results show that multi-stage RANS are unable to predict the operating envelope of the compressor, while URANS are capable to move much closer to the measured performance and operability. Importantly, single stage RANS accuracy can be largely improved by enforcing inlet and exit boundary conditions extracted from the time aver-aged multistage URANS. This suggests that full multistage URANS may be used to compute a limited number of operating points of interest. These runs provide a set of realistic stage inlet and exit profiles, that can be enforced in single stage RANS in the framework of design iterations, although the stage geometry modifications should not be large enough to provoke a significant departure from the original inlet profiles.

5 Aeromechanical validation

This chapter reports the aeromechanical validation of the steady-unsteady CFD strategy. The content of the this chapter has been submitted to ASME Turbo Expo 2021 [112] [113]. In the first part the numerical results obtained by a modal work approach are compared with experimental data focusing on two resonances, the first of which is detected by the classical use of the interference diagram, while the second one is justified only by the improved use. In both cases, the predicted blade responses are in good agreement with measurements. The second part focuses on the impact of clocking on forced response in axial compressors taking advantage of the spatial decomposition theory. An extensive numerical study of two final stages of the 11-stage compressor is reported.

5.1 Overall compressor results

The unsteady computation on the whole axial compressor allows, from an aeromechanical point of view, the evaluation of the complete blade load frequency spectrum and contains all the excitations.

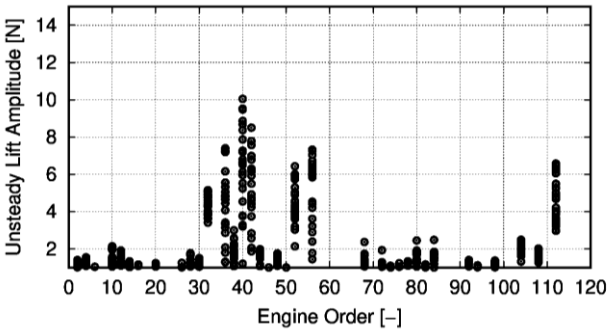

Figure 5.1 - R5 frequency spectrum

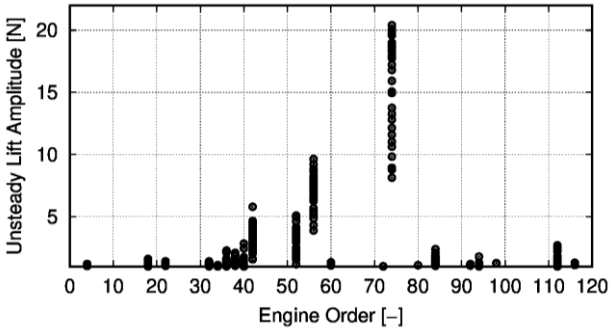

Figure 5.2 – R8 frequency spectrum

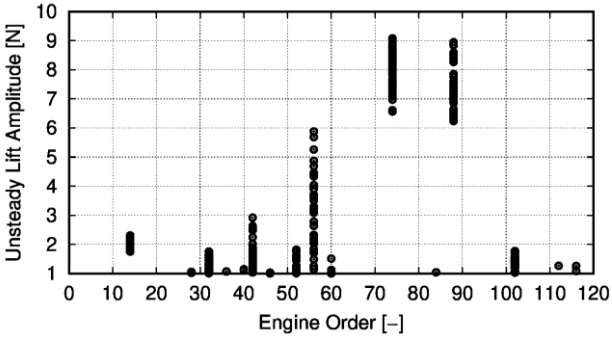

Figure 5.3 – R10 frequency spectrum

Figure 5.1, Figure 5.2 and Figure 5.3 show the blade load frequency spectrum of R5, R8 and R10 respectively. The unsteady lift amplitude and the engine orders are reported on y-axis and x-axis respectively. The plot is characterized by having two main features:

- The spectra present relevant contributions at many different frequencies. The engine order number clearly exceeds those due to interactions with adjacent rows.

- Each plot presents several points for each engine order and each point corresponds to the unsteady lift amplitude value of a single profile within the blade-row. All the engine orders that characterize the frequency spectrum show a relevant blade-to-blade variability in terms of unsteady lift amplitude. An example is reported in Figure 5.4 that shows the blade-to-blade variability of unsteady lift amplitude at EO 74X on R8.

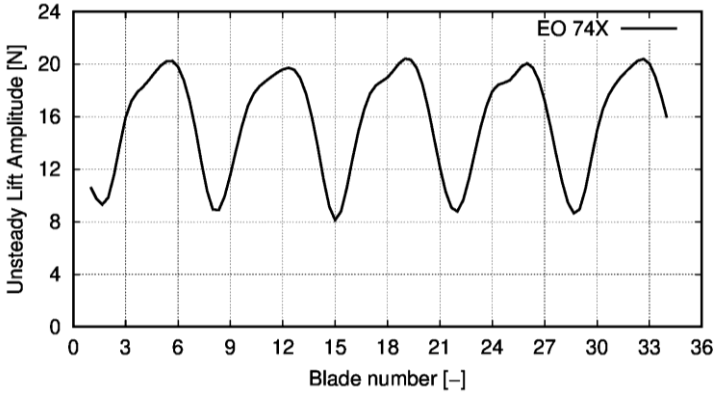

Figure 5.4 - Unsteady lift amplitude of EO 74X on R8

The large number of engine order cannot be evaluated through a single stage unsteady computation. Moreover, each unsteady forcing is composed by several contributions with different number of nodal diameters that can excite the blade at different operating conditions. This behavior can be observed looking at Figure 5.5 (74X on R8) that shows the maximum value of the amplitude of the time-space Fourier coefficients on the blade surface decomposed into all the possible m that will excite the NDs of the blade-row. The single stage computations can only predict the main contribute due to the different count between rotor and stator (6). The exciting forcing with ND=-5 and

ND=16 are captured only with the whole compressor domain simulation. Figure 5.10 (56X on R7) shows that a single engine order can be composed of a large number of contributions with different circumferential orders. It is definitely clear that the full annulus unsteady approach of the whole compressor allows to design the blade considering a vast amount of unsteady interactions avoiding unexpected resonance conditions.

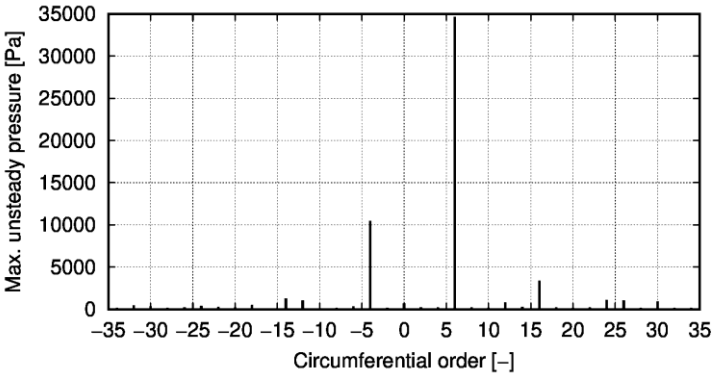

Figure 5.5 - Maximum unsteady pressure amplitude of EO 74X on R8 blade surface vs. circumferential order

5.2 Forced responce test case

The numerical CFD approach described in the thesis was validated with the help of an extensive experimental data set of an 11-stage axial compressor prototype. The test details and the instrumentation described in chapter 4.1 allowed a detailed aerodynamic and aeromechanic characterization of the prototype multistage axial compressor.

The resonant response of an intermediate rotor stage (Rotor 7) to the engine order excitation of the upstream stator (Stator 6) at different rotational speed has been used as validation data. Two different resonances that showed a repeatable behaviour

across multiple test instances is used as reference test cases. The two specific response conditions investigated in different speed ramps are summarized in Table 6

	Case1	*Case2*
Rotational Speed (N/N_{ref})	0.90	1.00
Normalized Frequency (f/f_{ref})	0.90	1.00
Corrected mass flow ($m_c/m_{c,ref}$)	0.66	1.00
Compressor Inlet Pressure (bar)	0.76	0.40
Overall Pressure ratio (PR/PR_{ref})	0.56	1.00
Most sensitive gage measured response (microstrain) (see Figure 5.7 for position and orientation)	300 ±10% (gage1)	85 ±10% (gage2)

Table 6 - Reference R7 responses for validation

The Case 1 was chosen in order to validate the procedure for a typical crossing where the aerodynamic forcing is directly generated by the wake of the upstream rows. The Case 2 was chosen to demonstrate the capability of this approach to find and correctly predict also unexpected resonance condition (see Figure 5.6). The airfoil count is included in Table 7, because of their influence on forced response results, as shown in chapter 5.4. The Rotor 7 interference diagram computed with the assumptions explained in section 5.3 is shown in Figure 5.6. The aliased engine order corresponding to the Stator 6 count (56) on Rotor 7 (68) is equal to 12. The case1 observed resonance is clearly detected by the standard use of interference diagram, as visible by the crossing of the vertical dash-dot line, corresponding to the harmonic index of 12, with the case1 frequency that coincides with one resonant mode described by the dotted line.

Airfoil	Count
R5	44
S5	56
R6	50
S6	56
R7	68
S7	74

Table 7 - Reference compressor airfoils count

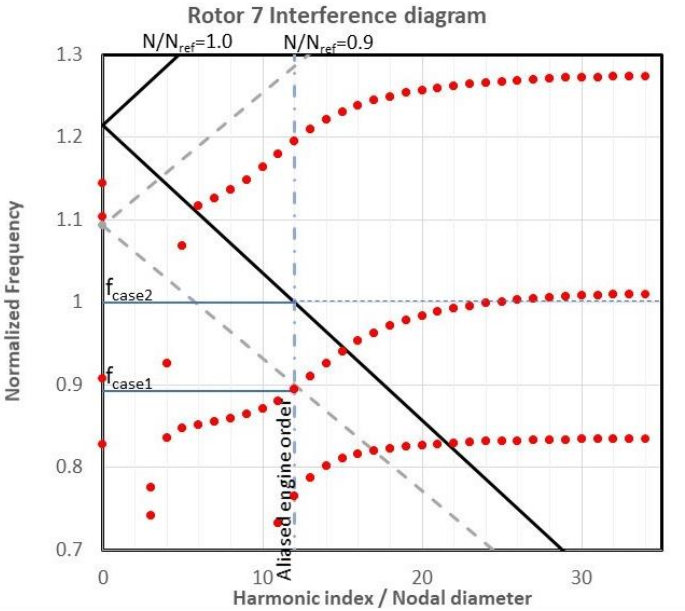

Figure 5.6 - R7 interference diagram

On the contrary, case2 detected resonance, although lower in amplitude, needs a more complex explanation based on the spatial decomposition theory, as it does not immediately appear as a risk from the baseline interference diagram. Since there are no natural modes with harmonic index equal to the aliased engine

order of 12 close to case2 frequency, the measured response must be due to a mode with a different harmonic index (nodal diameter). The detailed explanation of the origin of a forcing with higher nodal diameters is done in the section 5.4.

5.3 R7 FEM model

The FEM computation was not performed directly by the author of the thesis, but the detail of the FEM model has been reported for clarity. The FEM model included a fundamental sector of Rotor stage 7, comprising the corresponding portion of disk and accounting for cyclic symmetry constraints (see Figure 5.7); non-linear contact has been assumed to model rotor-disk interface.

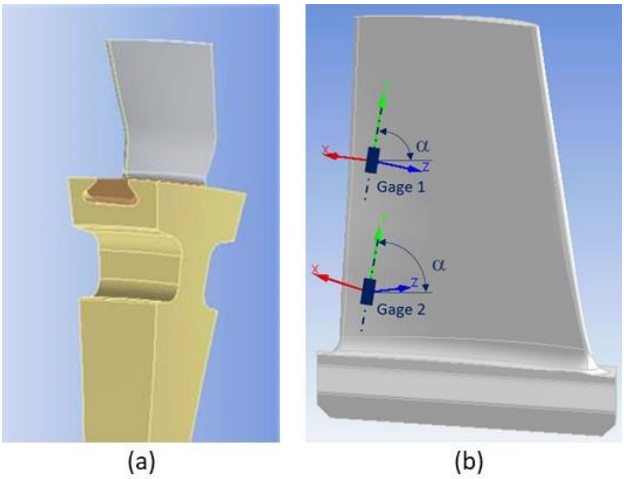

Figure 5.7 - (a) View of the reference compressor Rotor 7 bladed disk (b) Reference compressor Rotor 7 gages position and orientation (both gages oriented along Y axis)

Given the main purpose of the simulation, special attention has been paid to capture the major phenomena of whom effects on component dynamics are known: pre-stress, geometrical non-linearities and temperature dependent material properties. Therefore, simulation setup has consisted in a pre-stressed modal analysis, thus requiring the stress results coming from the static computation to be considered into the subsequent modal counterpart, acting on the system stiffness matrix. On gas turbine compressor blades, in fact, the contribution of the pre-stressed state onto blade dynamics can be significant: combination of generally high tensile stresses and slender airfoil geometry often leads to measurable variation of blade natural frequencies.

Geometrical non linearities has represented the second focus of the static calculation. Again, slender airfoil aero design being operated at high nominal speed can undergo sensible structural deformation – especially when characterized by a certain level of 3D complexity – which tends to straight the geometry in the radial direction and to reduce bending stresses, thus affecting component eigenvalues by means of the modal pre-stress. Geometrical non linearities play also a second important role in settling the accuracy of the unsteady pressure mapping process. Unsteady pressure distributions coming from CFD calculations usually refer to components under operative condition, thus in hot temperature state and subject to static pressure and inertial loads. A quality structural analysis should then be able to correctly predict the shape of the component once in its operating condition yet starting from its cold shape, usable for production. If good accordance is met, the mapping of hot unsteady pressure onto an initially cold model will also benefit from the accuracy of the map superposition. As last main focus, the analysis has accounted for material properties variation over operating temperature. As widely known, material Young Modulus tends to

decrease over an increasing temperature, leading to measurable drop of the component natural frequencies.

5.4 R7 results

The R7 blade-row frequency spectrum is shown in Figure 5.8. The unsteady lift amplitude and the engine orders are reported on y-axis and x-axis respectively. Also in this case the all the engine orders are characterized by a relevant blade-to-blade variability in terms of unsteady lift amplitude.

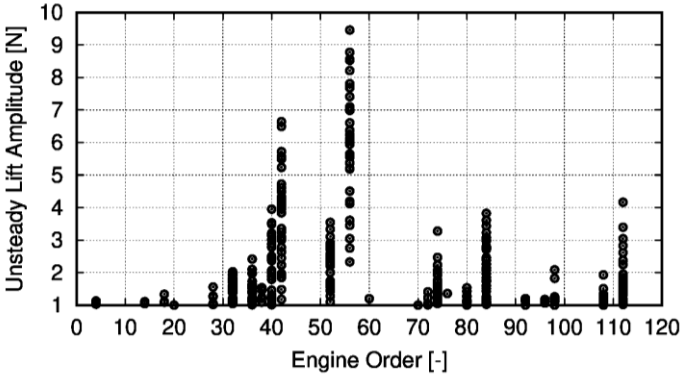

Figure 5.8 - R7 frequency spectrum (case2)

As explained in the chapter 2.2.3.2.1, the unsteady lift amplitude blade-to-blade variability in a same blade-row is due to the superpositions of two or more rotating unsteady pressure wave with the same frequency, but different circumferential patterns. Considering that each circumferential order can excite a particular nodal diameter of the blade-row, the circumferential decomposition is therefore necessary for the accurate forced response assessment.

As already said, the resonant response of R7 to the engine order excitation of the S6 has been investigated. Figure 5.9 shows the

blade-to-blade variation of unsteady lift amplitude of the BPF 56X on R7. The amplitude variation between the minimum and maximum value is greater than 100%. This means that the contributes of the different spinning perturbations are not negligible.

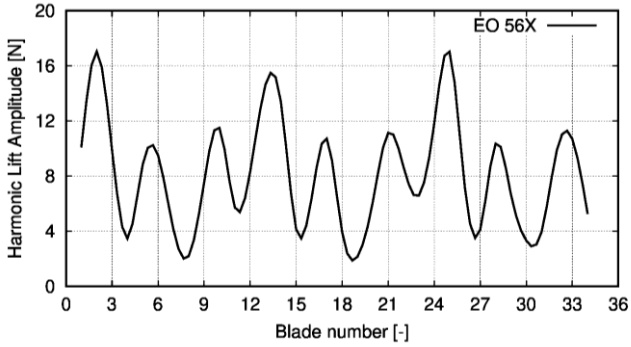

Figure 5.9 - Unsteady lift amplitude of EO 56X on R7 (case2)

Applying the circumferential DFT to the unsteady pressure time Fourier coefficients on the blade surfaces, the contribution of the different circumferential order can be separated. Figure 5.10 shows the maximum value of the amplitude of the time-space Fourier coefficients on the blade surface decomposed into all the possible m that will excite the NDs of the blade-row.

The sign on the ND is referred to the rotational direction of the spinning perturbation compared with the rotational speed direction, in detail:

- negative value corresponds to forward running forcing respect to R7
- positive value corresponds to backward running forcing respect to R7

The origin and the spinning lobe circumferential order found from the time-spatial decomposition (which will excite the cyclic mode-shapes) of the engine order 56X are summarized int the following list:

1. the main interaction between S6 and R7

$$m = 56 - 68 = -12 \Rightarrow \mathrm{ND} = 12$$

2. the interaction between S6 and R6

$$m = 56 - 50 = 6 \Rightarrow ND = -6$$

3. the interaction between S5 and R5

$$m = 56 - 44 = 12 \Rightarrow ND = -12$$

4. the interaction between S6 and the second harmonic of R6

$$m = 56 - (50 \times 2) = -44 \overset{aliased}{\Longrightarrow} ND = -24$$

5. the interaction between S5 and the rotating distortion due to different count between R6 and R5

$$m = 56 - (50 - 44) = 50 \overset{aliased}{\Longrightarrow} ND = 18$$

6. the interaction between S6 and the rotating distortion due to different count between R7 and R6

$$m = 56 - (68 - 50) = 38 \overset{aliased}{\Longrightarrow} ND = 30$$

7. the interaction between S6 and the rotating distortion due to different count between the second harmonic of R6 and the second harmonic of R5

$$m = 56 - (68 \times 2 - 50 \times 2) = 30 \Rightarrow ND = -30$$

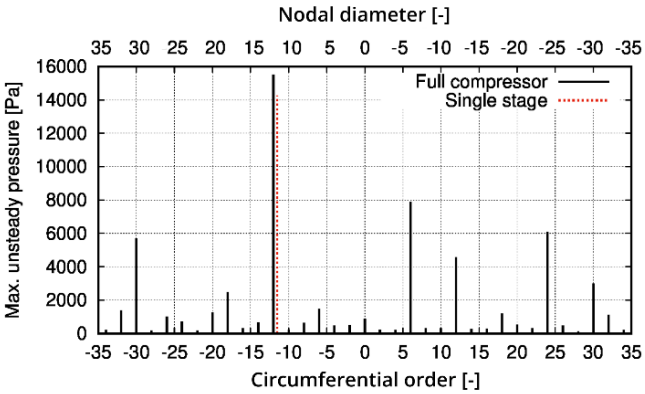

Figure 5.10 - Maximum unsteady pressure amplitude of EO 56X on R7 blade surface vs. circumferential order and nodal diameter (case2)

5.4.1 Classical crossing results

As introduced in previous paragraphs, the validation of the methodology proposed in the thesis to evaluate the forced response is performed firstly for case1 response that is linked to the main interaction (S6-R7). The unsteady CFD analysis of the complete compressor domain with boundary conditions coherent with Table 6 was performed to compute the unsteady pressure fluctuation of all the different profiles composing R7 included in the computational model. Then the spatial decomposition process was applied to extract the proper spinning unsteady pressure component, that will excite the ND=12 rotating in the forward direction. The aerodynamic damping was computed with the numerical procedure detailed in section 2.2.2.1: a single row unsteady computation with the R7 blade-row which vibrates following the ND=12 nodal diameter forward rotating mode shape.

The comparison between calculated and measured responses on gage1 is included in Table 8 and shows a good agreement.

ND	Normalized Frequency	Predicted Q	Predicted Response (gage1)	Measured response (gage1)
12	0.894	594	279.7	303.0 (±10%)

Table 8 - Case1 response

The small difference between the numerical prediction and measurements could be due to uncertainties linked to effective boundary conditions considering that the experimental response was measured during a shut-down transient.

5.4.2 Tyler-Sofrin crossing

Case2 response requires a more complex explanation. Figure 5.9 shows the maximum amplitude of the time-space pressure Fourier coefficients for each circumferential order on the R7 at the 56X engine order from the all compressor computation and the reduced S6-R7 analysis. This comparison highlights the appearance of additional spatial content with amplitude lower than the main interaction, but that should be considered to assess the overall blade resonant response risks. The main components and the explanation of their generating mechanism are explained in section 5.4. The additional nodal diameters are highlighted in the R7 interference diagram in Figure 5.11 to detect potential resonances in case2 conditions applying the improved use procedure.

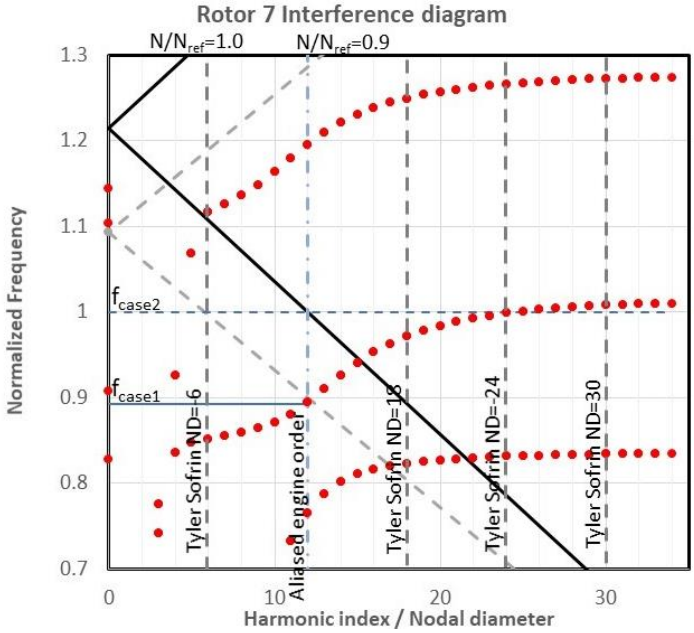

Figure 5.11 - R7 interference diagram: improved use to highlight crossing with additional modes

Since case2 excitation frequency is close to the mode natural frequencies for the nodal diameters 18, 24 and 30, the resonant response is computed for all these three cases, by extracting the corresponding unsteady pressure components with the spatial decomposition process on the results of the unsteady analysis of the complete domain. The modal damping ratio is assumed equal to the aerodynamic damping computed with the presented method for the corresponding mode-shapes. Table 9 shows the comparison between predicted and measured case2 responses.

ND	Normalized Frequency	Predicted Q	Predicted Response (gage2)	Measured response (gage2)
+18	0.970	742	3.4	85 (±10%)
-24	0.998	969	56.0	
+30	1.008	805	7.7	

Table 9 - Case2 response

The results suggest that the ND=-24 is most excited mode-shape mainly responsible for the overall case2 response. The predicted response value is reasonably close to the experimental measurements, demonstrating that Tyler-Sofrin interactions propagating along the compressor may have enough amplitude to excite airfoils structural modes.

5.4.3 Reduced domain

In case of blade redesign the exciting force may be revaluated. In that case, an unsteady computation on a reduced domain can be performed to update the unsteady pressure perturbation on the blade surface.

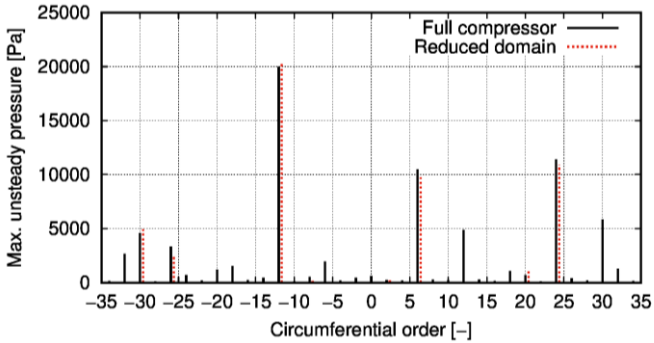

Figure 5.12 - Maximum unsteady pressure amplitude of EO 56X on R7 blade surface vs. circumferential order (case1)

The reduced computational domain must include all the blade row that are involved in the generation of the exciting nodal diameter. The inlet boundary conditions are taken from the pitchwise-averaged and time-averaged spanwise profiles of the unsteady run of the complete domain. The unsteady analysis on the whole compressor is necessary to evaluate all the nodal diameters in-volved but once they are selected, the use of a reduced domain is sufficient to correctly predict the investigated unsteady force. As already said, the classical crossing can be evaluated with a two-row unsteady computation (see Figure 5.11). Instead, the Tyler-Sofrin crossing can be evaluated with an unsteady analysis on a reduced domain from S5 to R8.

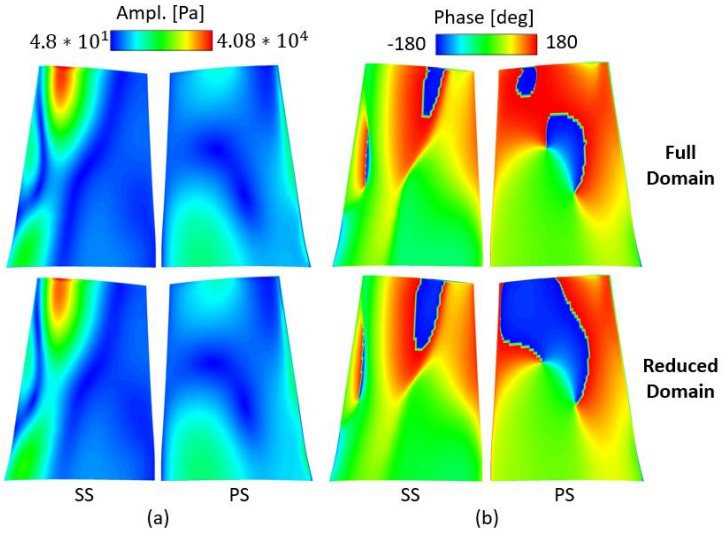

Figure 5.13 -Unsteady pressure amplitude (a) and phase (b) from time and space decomposition (EO=56X and m=24) on R7 of full domain and reduced domain computation from top to bottom respectively

A comparison between full compressor and reduced domain unsteady analysis is reported in Figure 5.12. The circumferential order 24 has similar value between the two cases. Note that all the common m have similar values. The circumferential order equal to 12, 30 and -32 are not present in the reduced domain result because they are all generated by interactions with R5 that has not been included in the computational domain. Figure 5.13 shows the unsteady pressure Fourier coefficient in time and space distributions on R7 blade surface relative to 56X and m=24 in terms of amplitude and phase. The comparison between the two unsteady approach results shows that the unsteady forcing predicted by the reduced domain computation is quite the same to the ones predicted by entire compressor domain computation. The slight difference on the PS appears to be relevant only because of the discontinuous transition between -180 and 180.

5.5 Clocking effect on aerodynamic forcing

Given that Tyler-Sofrin interactions propagating along the compressor can excite airfoils structural modes, a clocking analysis that take into account the spatial decomposition theory is necessary to investigate the impact of clocking on the additional unsteady forcing.

The literature survey covered in the introduction reveals two research branches on clocking, one focusing on performance, and eventually on operability, one focusing on aeromechanics. The present investigation discusses primarily the aeromechanics implications of clocking as the numerical results revealed a very small impact on group performance, at least for back stages.

In modern gas turbines axial compressors it is common practice to have different stator counts on the two halves of the casing to increase scatter and reduce aeromechanics risk. Obviously, this practice is not applicable to rotors, that are subject to detailed scrutiny to avoid dangerous crossing. Therefore, when a designer is challenged by a dangerous aeromechanic crossing, evidenced by the application of the safe diagram, he initiates a complex iterative process, often trial-and-error, in which natural frequencies are changed by moderate airfoil changes the aerodynamic impact of which is verified by CFD. The analyses aim at understanding if rotor or stator clocking can possibly help in reducing the aeromechanic risk, thereby adding more design change opportunities for a designer. To make sure clocking can really help, the investigation covered both rotor and stator clocking, and it extended to two different operating points to ascertain the robustness of the conclusions. All the discussions and considerations are mainly based on the time-space decomposition results of the unsteady forcing.

5.5.1 Numerical test case

The numerical test case, extracted from the 11-stage multistage axial compressor, is composed by two final stages typical of an industrial gas turbine compressor.

	R10	S10	R11	S11
Case A	80	88	80	88
Case B	76	88	80	88
Case C	80	92	80	88

Table 10 - Summary of blade and vane counts.

The reduced domain was selected to study the circumferential distortions that occur when blade-rows in the same frame of reference have different sets of airfoil counts (see chapter 2.2.3.2.1) and relative tangential position. Table 10 summarizes the three investigated cases. The analyses have been performed at two speeds, design point with Nc=100%, and an additional point at 90%. The tangential position of the row with the same count was kept the same in the three different cases. Starting from the baseline geometrical position, the clocking effect on the aerodynamic forces have been investigated by changing the blade tangential position.

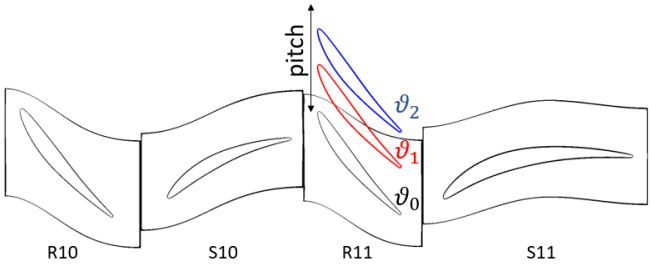

Figure 5.14 - R11 clocking positions

If we consider that the tangential position of the clocking row in the baseline case is equal to ϑ_0, two additional tangential positions, illustrated in Figure 5.14 for R11, have been considered, called ϑ_1 and $\vartheta_2$respectively:

$$\vartheta_1 = \vartheta_0 + \frac{1}{3}\vartheta_{pitch} = \vartheta_0 + \frac{1}{3} * \frac{2\pi}{NB} \tag{65}$$

$$\vartheta_2 = \vartheta_0 + \frac{2}{3}\vartheta_{pitch} = \vartheta_0 + \frac{2}{3} * \frac{2\pi}{NB} \tag{66}$$

The tangential position variation has been always applied to R11 for all the three cases under investigation. Case B was further analysed by applying the same tangential position variation to S11 to determine the impact of stator clocking. As anticipated, the analyses with different clocking position of R11 for case A have been repeated for a different operating condition, characterized by Nc=90%, to determine the impact of operating condition on clocking effect. Table 11 summarizes the extensive computational analysis performed in this work.

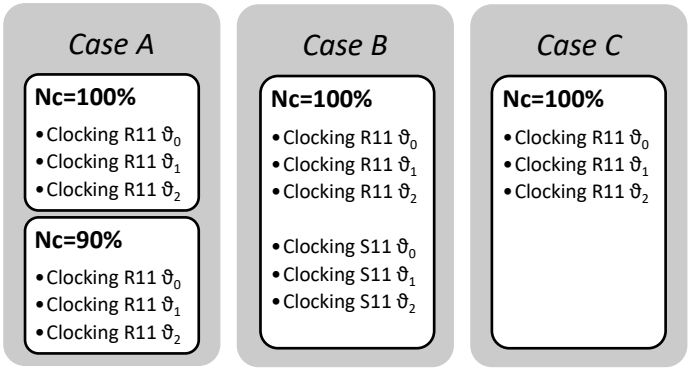

Table 11 - Summary of performed clocking analysis

The inlet spanwise profiles used for the numerical simulations with Nc=100% are taken from the time-averaged spanwise profiles of the ADP multistage unsteady runs at the R10 inlet section (see [17]). In particular, time-averaged profiles of stagnation pressure and temperature, pitch and yaw angle and turbulent quantities were set at inlet, while the spanwise distribution of static pressure was specified at the outlet section. In order to isolate the effect of the different operative points, the inlet condition at Nc=90% was very mildly tuned to guarantee the same

incidence on R10 of Nc=100% case. The stagnation temperature and pressure profiles have been obtained by scaling the spanwise distributions on the inlet average value of Nc=90% according to an internal meanline tool prediction.

5.5.2 Clocking results

This section concentrates on the clocking effect of the first blade passing frequency. The results are expressed in terms of two main quantities:

- The unsteady lift amplitude, that corresponds to the amplitude of the lift Fourier coefficients in time at selected frequencies extracted over one numerical period (1/4 revolution).
- The unsteady pressure distribution on blade surface in terms of amplitude and phase of pressure Fourier coefficients in time and space that determines the forcing shape on the airfoil surface at a given nodal diameter.

In the following result discussion, the spatially decomposed rotating forcing (usually defined by the circumferential order) are identified in terms of nodal diameter notation (as used for the traveling wave mode-shapes) for the sake of simplicity. With this notation, unsteady forcing with positive nodal diameters rotates forward with respect to the rotational speed, while negative nodal diameters describe backward forcing.

5.5.2.1 Impact on performance

As anticipated, the computed impact of clocking on performance was found to be small. The variation of time-average lift amplitude was lower than 0.5% for all the computed cases, and the corresponding impact of performance was evaluated in terms of

stator and rotor kinetic loss coefficients (see equation (20)). Figure 5.15 and Figure 5.16 show the kinetic loss variation with respect to the baseline clock ϑ_0 of case A with R11 clocking and case B with S11 clocking. The plots reveal an up-down trend from R10 to S11 worth around +/-1% of the baseline kinetic loss. The same figures show the overall efficiency of this hypothetical two-stage compressor. This is computed as the cumulative total-to-total efficiency η_{tt} and proves that the positive and negative effects almost entirely cancel out, as the symbols corresponding to the three clocking positions hardly move from unity. As observed by Huang et al. [41] CFD tends to underestimate by a factor 2 the impact on performance as compared to experiment. Still, the detailed analyses of Jia et al. [44] and Mueller et al. [45] showed very small performance impact, as confirmed by the present investigations when looking at group, and not a single row, efficiency. Therefore, the remainder of this thesis does focus on the aeromechanics impact of clocking, as this may affect the structural integrity of the compressor.

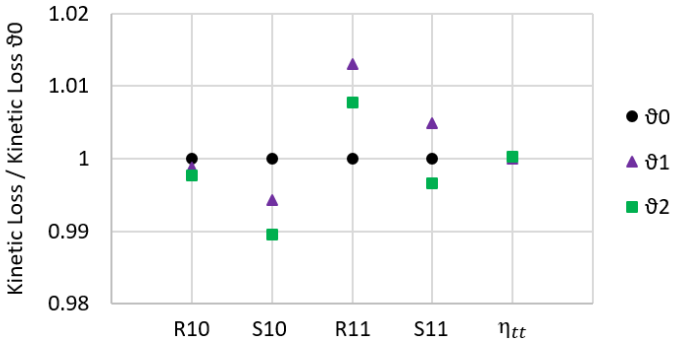

Figure 5.15 - Kinetic loss variation respect to case ϑ_0 of case A with R11 clocking

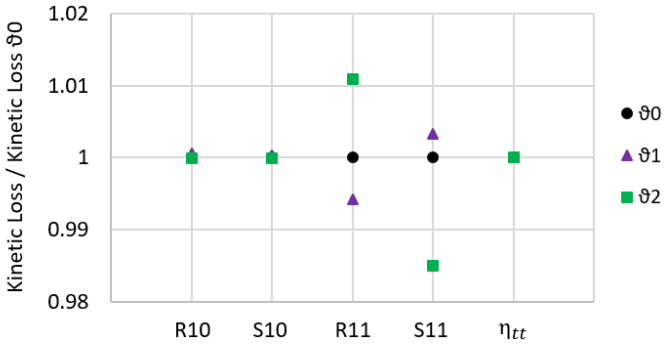

Figure 5.16 - Kinetic loss variation respect to case ϑ_0 of case B with S11 clocking

5.5.2.2 Case A - R11 clocking

This section discusses the results of R11 clocking on the airfoil count of case A. The first part 5.5.2.2.1 shows that the clocking position has a relevant effect on the unsteady lift amplitude. The second part 5.5.2.2.2 shows that the optimum clocking position changes with the operating condition, as already noted for other gas turbine components (see [39]). As a result, it is not possible to find a unique clocking position that minimizes the unsteady force for all the points of interest in the operating range. Salontay et al. [49] observed a similar behaviour. Therefore, the optimization of the clocking position for aeromechanical purposes is very tricky and could be done only on specific operating conditions where the crossings appear most dangerous and would require, at the same time, a verification for the rest of operating points in terms of forcing amplitude and distribution.

5.5.2.2.1 Nominal speed (100%)

The tangential position of R11 changes as described before and the unsteady calculations are performed at Nc=100%. Figure 5.17 shows the R11 unsteady lift amplitude at stator BPF (88X) with the three different clocking positions. The figure shows that the unsteady lift amplitude is constant across all the 20 adjacent airfoils of R11 included in the unsteady simulations.

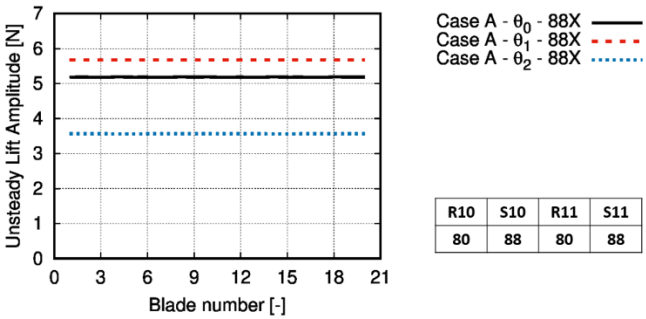

Figure 5.17 - Unsteady lift amplitude on R11.

The different tangential positions provoke a relevant variation in the unsteady lift amplitude. The concerted action of Tyler-Sofrin interaction between R10-S10 and the classical interactions S10-R11 and R11-S11 that produce the overall forcing at the BPF (88X), varies with the R11 tangential position because of the changes in the relative phase of the pressure waves with same nodal diameter coming from different sources. In fact, the overlap of two contributions can be constructive or destructive depending on their relative phase. Figure 5.18 and Figure 5.19 explain this with a simplified case characterized by three waves with the same number of nodal diameters but different relative phase. The final wave is the superimposition of the three contributions and show a different amplitude depending on the relative phase. The case 1, which corresponds to Figure 5.18, shows

the maximum amplitude since the three waves with zero relative phase add up constructively, while the amplitude of case 2 in Figure 5.19 is lower because the relative phase shift produces a destructive effect. The amplitude of the final wave is lower than the amplitude of the single wave with ND 8 generated by the single S10-R11 interaction.

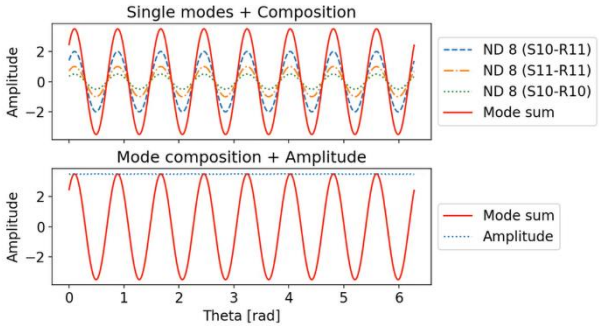

Figure 5.18 - Case 1: Overlap of three sinusoidal waves with the same number of nodal diameter and same phase

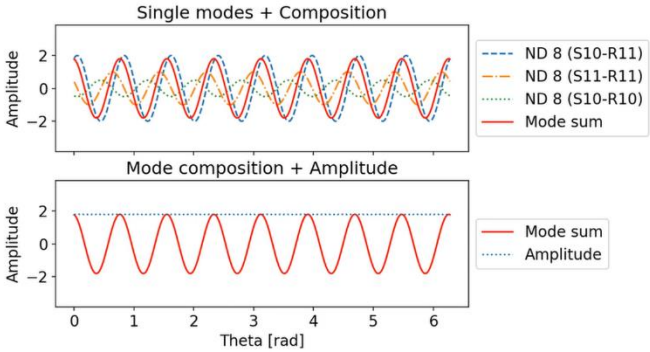

Figure 5.19 - Case 2: Overlap of three sinusoidal waves with the same number of nodal diameter and different phase

The spatial decomposition of the unsteady pressure distribution on the blade surface, obtained by applying a spatial DFT in the circumferential direction, shows that the 88X has a single ND content equal to 8. Unfortunately, it is not possible to separate the contributions from the three different sources as they have the same ND number. Figure 5.20 shows the unsteady pressure Fourier coefficient in time and space distributions on R11 blade surface relative to 88X and ND=8 in terms of amplitude and phase with three different clocking position of R11. The three positions give different surface distribution both in terms of amplitude and phase. The magnitude and, most importantly, the position of the maximum pressure amplitude vary with the clocking position.

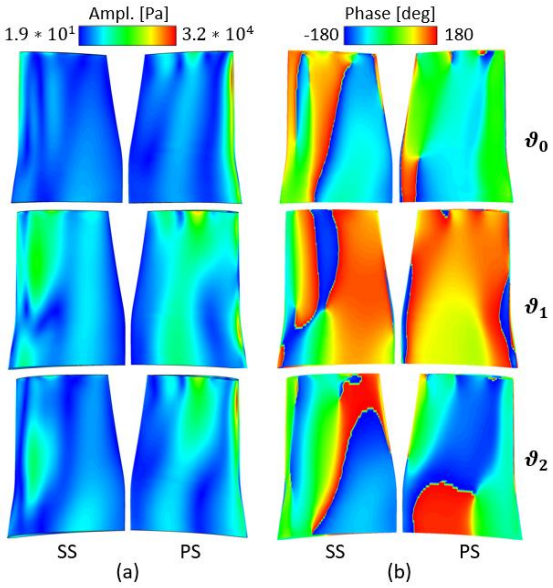

Figure 5.20 - Unsteady pressure amplitude (a) and phase (b) from time and space decomposition (EO=88X and ND=8) on R11 with clocking position ϑ_0, ϑ_1 and ϑ_2 from top to bottom respectively

Considering that the forced response results do not only depend on the unsteady force amplitude, but also on the matching between unsteady force distribution and the mechanical mode shape, the selection of an optimal clocking position for the entire airfoil pressure may be very tricky, or practically impossible. The effect of R11 clocking on R10, that have the same airfoil count, is shown in Figure 5.21. The variation of unsteady lift amplitude is larger than 100% with respect to the baseline clocking ϑ_0. This result highlights the fact that clocking position may also affect the unsteady forces on the upstream rows.

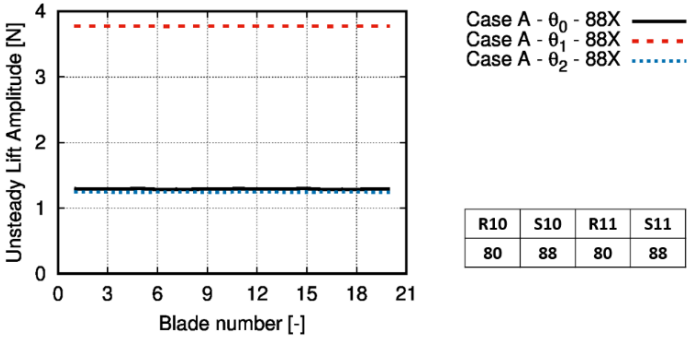

Figure 5.21 - Unsteady lift amplitude on R10

This also indicates that the upstream running pressure wave due to the Tyler-Sofrin interaction between S10-R11 is not negligible, and its effect can also be observed when looking at the unsteady pressure distribution on R10 blade surface (see Figure 5.22) where the configurations with clocking ϑ_1 and ϑ_2 present different amplitude and phase distributions. The clocking position of R11 therefore has an impact on the forced response assessment of both rotors.

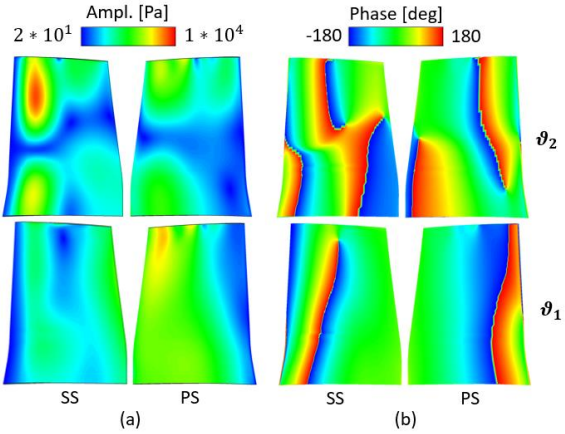

Figure 5.22 - Unsteady pressure amplitude (a) and phase (b) from time and space decomposition (EO=88X and ND=8) on R10 with clocking position ϑ_2 (top) and ϑ_1 (bottom)

The rotor clocking positions investigated here appear to modify the unsteady force not only on rotor rows but also on stator rows.

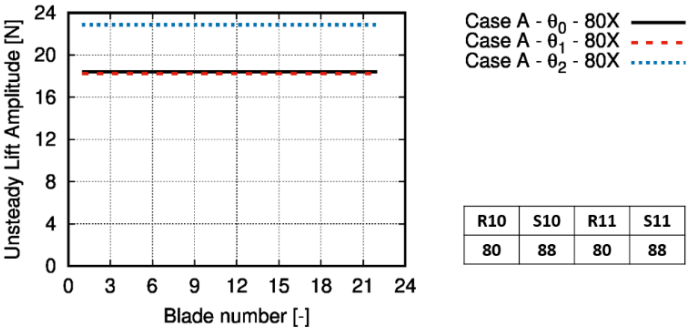

R10	S10	R11	S11
80	88	80	88

Figure 5.23 - Unsteady lift amplitude on S10

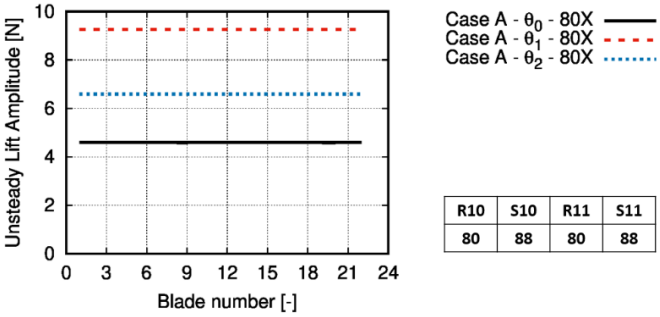

Figure 5.24 - Unsteady lift amplitude on S11

Figure 5.23 and Figure 5.24 show the unsteady lift amplitude on S10 and S11 respectively. S11 presents a variation greater than a factor 2 from clocking ϑ_0 to clocking ϑ_1. As a result, the search for a unique optimal clocking position may be even more challenging when trying to find a solution that holds valid across different operating points.

5.5.2.2.2 Off-design speed (90%)

An important aspect that must be evaluated is how the clocking effect changes with different operating conditions across different compressor speedlines. As indicated by Salontay et al. [49] for axial compressors, optimal clocking position may vary along the speedline, while Vazquez et al. [39] observed similar difficulties for low pressure turbines. Therefore, the results discussed in this section are related to Case A at Nc=90% once again modifying the tangential position of R11 as done in the companion Nc=100% case. Figure 5.25, Figure 5.26, Figure 5.27 and Figure 5.28 show the variation of the unsteady lift amplitude from Nc=100% to Nc=90% by comparing the unsteady lift plots for the four airfoil rows. The trends of unsteady lift amplitude

across baseline and ϑ_1 and ϑ_2 configurations change quite substantially when moving to a different operating point. Figure 5.25 clearly demonstrates that for R10 the clocking positions associated with the minimum and maximum unsteady lift change when moving from Nc=100% to Nc=90%. For instance, at Nc=100% ϑ_2 shows the minimum amplitude, that becomes the maximum amplitude among the three clocking positions at Nc=90%.

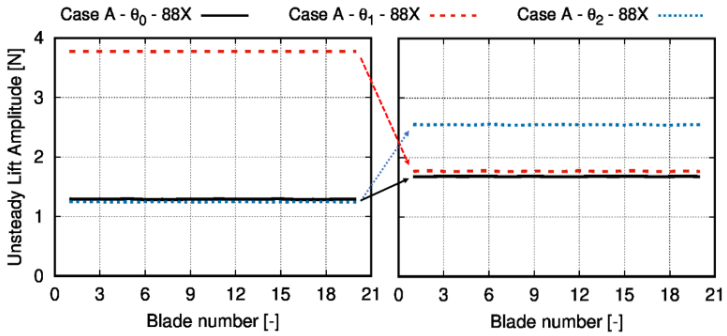

Figure 5.25 - Unsteady lift amplitude on R10 with Nc=100% (a) and Nc=90% (b)

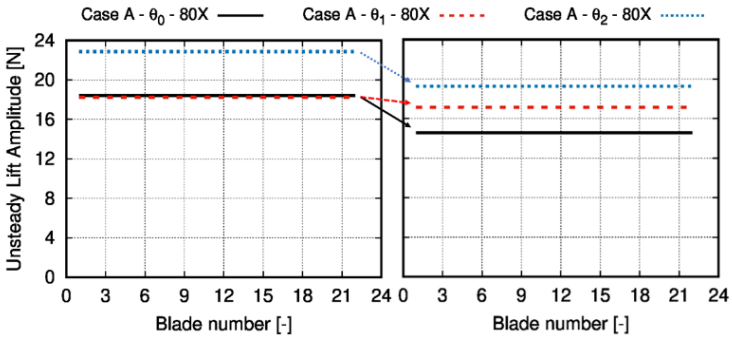

Figure 5.26 - Unsteady lift amplitude on S10 with Nc=100% (a) and Nc=90% (b)

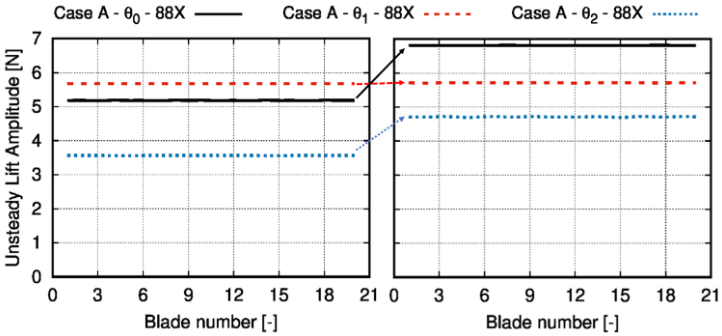

Figure 5.27 - Unsteady lift amplitude on R11 with Nc=100% (a) and Nc=90% (b)

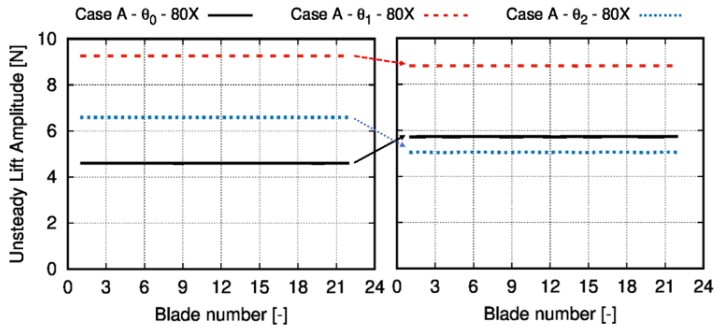

Figure 5.28 - Unsteady lift amplitude on S11 with Nc=100% (a) and Nc=90% (b)

Observe that the configurations with maximum amplitude for S10 and S11 are the same in both operating conditions (see Figure 5.26 and Figure 5.28). The same conclusion holds for the configuration with minimum amplitude of R11 (see Figure 5.27). From this set of plots, it is clear that the blade rows present different trends of the unsteady lift amplitude with the operating conditions. Consequently, it is not possible to identify a unique clocking position that minimizes the unsteady force

across different speedlines. This conclusion is confirmed by looking at the unsteady pressure distributions on blade surfaces. Figure 5.29 and Figure 5.30 prove that the surface unsteady pressure shapes with the same clocking position of both R10 and R11 change substantially when moving from Nc=100% to Nc=90%. The differences are significant in terms of both amplitudes and phase, and this suggests that they may result in a different mode-shape excitation across different speedlines. Therefore, the clocking position that minimizes the forced response at the design condition, Nc=100%, cannot guarantee that it will not determine a further resonance condition in off-design operation with another mode family, here at Nc=90%.

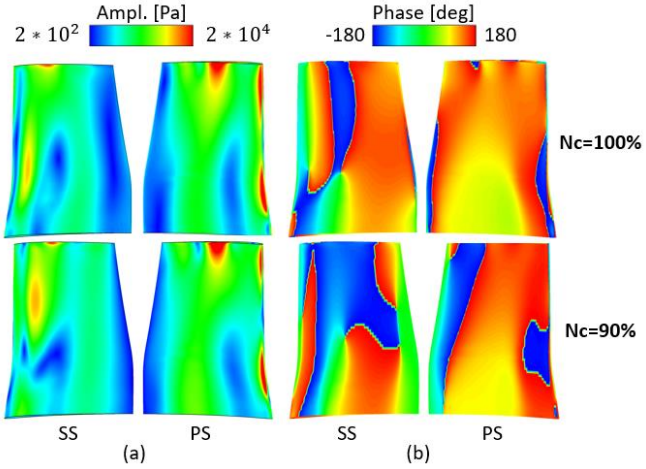

Figure 5.29 - pressure amplitude (a) and phase (b) from time and space decomposition (EO=88X and ND=8) on R10 with Nc=100% (top) and Nc=90% (bottom) with R11 clocking position ϑ_1

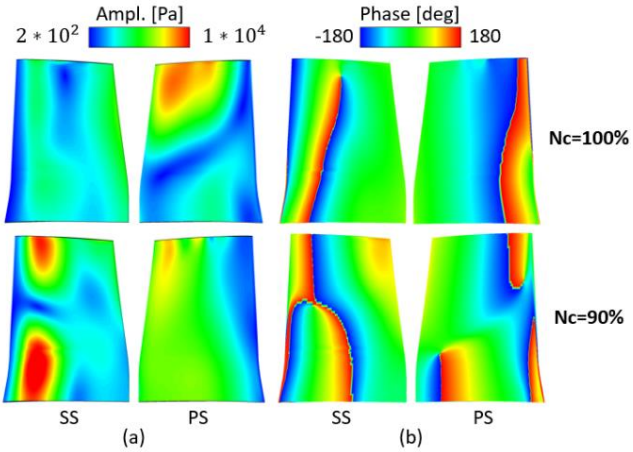

Figure 5.30 - pressure amplitude (a) and phase (b from time and space decomposition (EO=88X and ND=8) on R11 with Nc=100% (top) and Nc=90% (bottom) with R11 clocking position ϑ_1

Furthermore, the clocking position does also affect the amplitude and shape of the unsteady pressure on both rotors and stators.

5.5.2.3 Case B - R11 clocking

As already highlighted in chapter 2.2.3.2.1, the circumferential distortions of the unsteady lift amplitude are due to the sum of two, or more, rotating unsteady forces that have the same frequency, but have different circumferential patterns, or nodal diameters. The results discussed in this section concentrate on Case B with Nc=100%, i.e. nominal operating conditions, while changing the tangential position of R11 in order to investigate the clocking effect on the non-uniform unsteady lift distribution on adjacent blade rows. Figure 5.31 shows that the clocking

position of R11 does not change the circumferential distortion shape of the unsteady lift amplitude on R11 itself but it only causes a shift of the unsteady lift curve in the tangential direction. In other words, this shows that the minimum and maximum unsteady lift do not change their relative magnitude, but they occur on different blades. Recalling the results of the previous section on case A, it is clear that the composition of different acoustic spinning lobes at the same frequency and same nodal diameter leads to a constant value of the overall unsteady lift amplitude which is affected by clocking position. In this case, the composition of spinning lobes with different nodal diameters, always at the same frequency, produces a non-uniform unsteady lift distribution on adjacent blades and the clocking position only shifts this distribution tangentially.

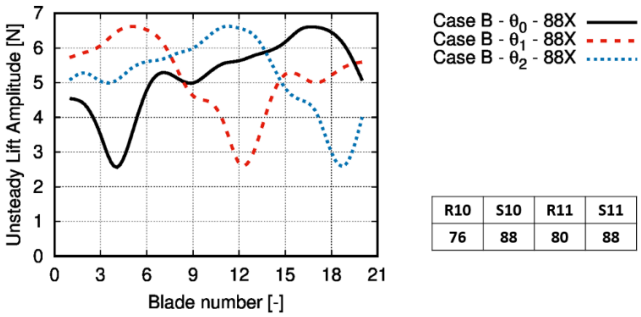

Figure 5.31 - Unsteady lift amplitude on R11 with Nc=100% of case B

In this case as well, the observed behaviour can be explained with the help of Figure 5.32 and Figure 5.33, that show a simplified case characterized by two waves with different number of nodal diameters, 8 and 12, and relative phase. The final wave composed by the sum of the two contributions presents the same

amplitude distribution but shifted tangentially. Indeed, the four peaks that characterize the pressure amplitude distribution of the "Mode sum" (see dashed line of the bottom diagram in both Figure 5.32 and Figure 5.33) have the same amplitude but different angular position.

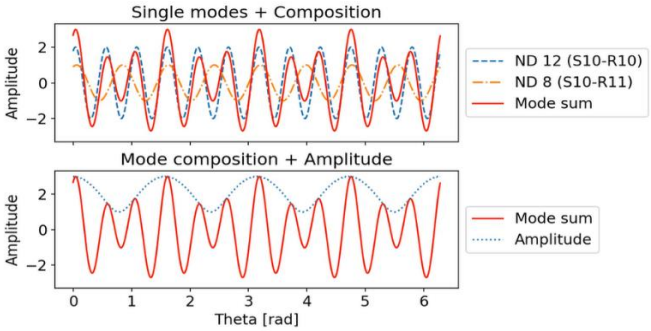

Figure 5.32 - Overlap of two sinusoidal waves with different number of nodal diameter and relative phase φ_0

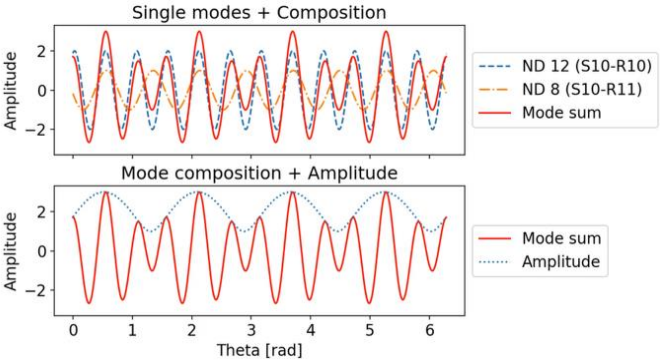

Figure 5.33 - Overlap of two sinusoidal waves with different number of nodal diameter and relative phase φ_1

This latter feature is confirmed when applying the circumferential DFT to the pressure Fourier coefficient in time on the blade

surface. This allows to separate the contribution of the different nodal diameters. In fact, the main contributions that compose the unsteady forces associated to 88X for case B are characterized by ND=8 and ND=12. Figure 5.34 and Figure 5.35 illustrate the unsteady pressure distribution on R11 blade surface relative to ND=8 and ND=12 respectively for the two clocking positions that depart from the baseline. When looking at ND=8 decomposition in Figure 5.34, it is immediately clear that the amplitude distribution is the same on both the pressure and suction sides for the two different clocking positions. Conversely, the phase angle distributions have substantially the same shape but with a constant phase-shift. Note that the ND=8 is generated by the cross interactions between R11 with S10, and R11 with S11. This leads again to an equal distribution of amplitude but a different phase because R11 is not in the same tangential position when switching to different clocking positions.

When looking at ND=12, the amplitude and phase of the decomposed pressure distribution are again practically the same because the disturbance is generated by the interaction between R10 and S10, and R10 and S11 (the slight difference on the SS appears to be relevant only because of the discontinuous transition between -180 and 180). The sum of these two interactions with ND=8 and ND=12, generate again the same unsteady lift distribution on the blade row, but in a different tangential position due to the phase shift of ND=8. Considering that the blade is excited by a single ND at the resonance condition, this implies that clocking has no influence on the forced response assessment of R11. This conclusion has very strong implications on design, as it proves that under an airfoil count similar to case B, R11 clocking does not have an impact on the aeromechanics risk.

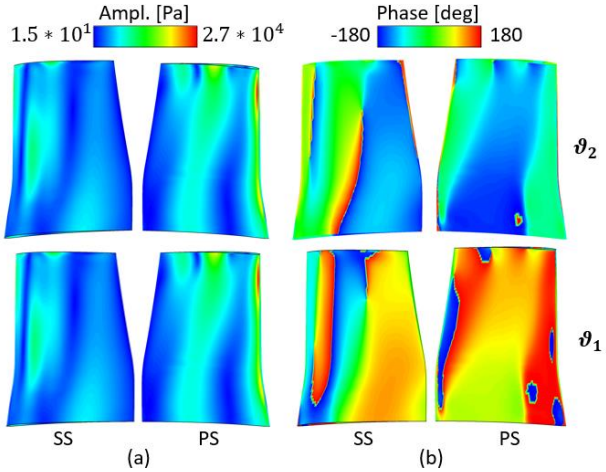

Figure 5.34 - pressure amplitude (a) and phase (b) from time and space decomposition (EO=88X and ND=8) on R11 with Nc=100% with R11 clocking position ϑ_2 (top) and ϑ_1 (bottom)

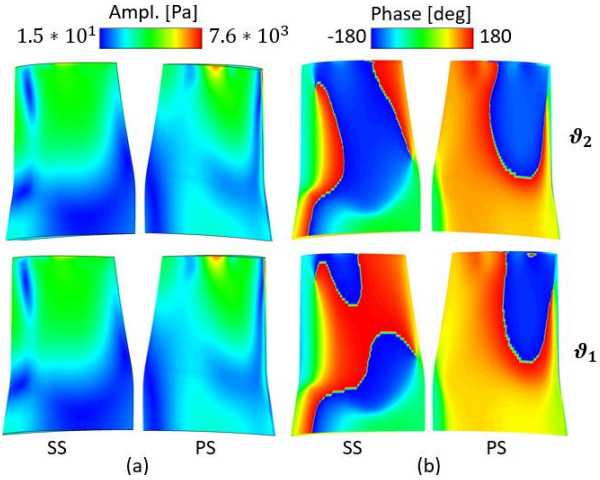

Figure 5.35 - pressure amplitude (a) and phase (b) from time and space decomposition (EO=88X and ND=12) on R11 with Nc=100% with R11 clocking position ϑ_2 (top) and ϑ_1 (bottom)

Nevertheless, it must be reminded how this mechanism is the same that changes the unsteady forces constant value on R11 on case A (see Figure 5.17). The main difference is that in case A the effect of the different contributions cannot be separated because they have the same ND equal to 8.

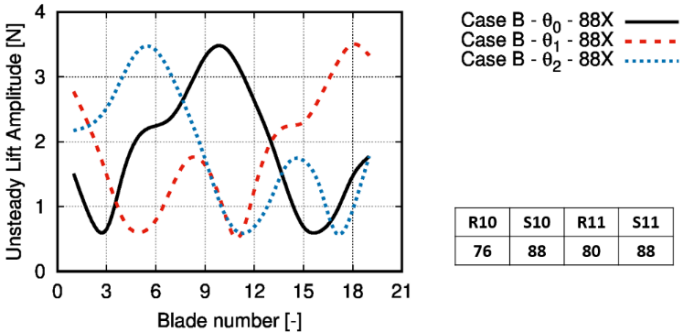

Figure 5.36 - Unsteady lift amplitude on R10 with Nc=100% of case B

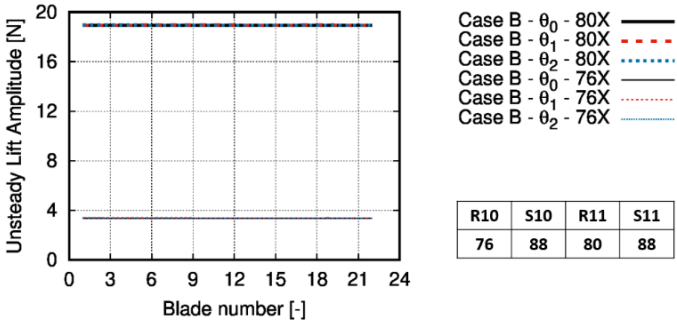

Figure 5.37 - Unsteady lift amplitude on S10 with Nc=100%

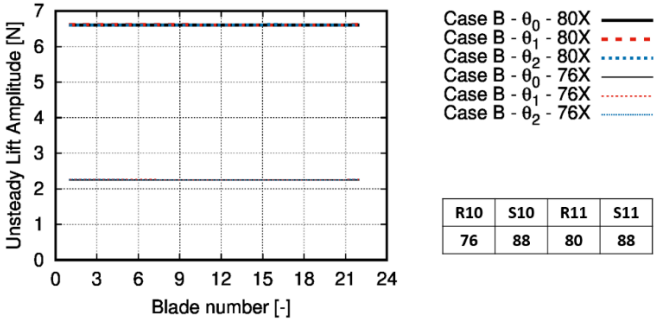

R10	S10	R11	S11
76	88	80	88

Figure 5.38 - Unsteady lift amplitude on S11 with Nc=100%

The contribution due to the interactions between R11-S10 and R11-S11 change the phase distribution with the clocking position while the interactions between R10-S10 and R10-S11 have a constant phase distribution. This leads to a variation of relative phase between the two contributions with the same nodal diameters (ND 8), and consequently their sum gives a different unsteady pressure amplitude. It is now possible to extend the analysis of clocking effect to R10, which is qualitatively the same of R11, as confirmed by the direct comparison of Figure 5.31 and Figure 5.36. The clocking position does not change the unsteady lift trend, but it only shifts its tangential position. The high blade-to-blade variation of the unsteady lift amplitude confirms once again the relevant contribution of Tyler-Sofrin upstream running pressure waves, due to the interaction between S10-R11 and R11-S11. Both stator rows are not influenced by the R11 clocking, as visible from Figure 5.37 and Figure 5.38. The different blade count between R10 and R11 generates two separate blade passing frequencies, 76X and 80X respectively, that are distinct, and this is the reason of their independence from R11 clocking. Instead, in case A, where the rotors did have

the same blade count the two contributions have the same frequency (80X), therefore the clocking position varies the relative phase between the two spinning contributions.

Therefore, the case B results have shown that the clocking position of a blade row with different blade count with respect to the other blade rows in the same frame of reference, has no effect on forced response assessment. Indeed, it can vary the unsteady overall lift distribution of a specific time harmonic, but it has no effect on the split contribution related to a single ND that excite the blade mode-shape at the corresponding nodal diameter. So, as expected, equal or different consecutive rotor blade count solutions react quite differently to clocking and pose different design challenges.

5.5.2.4 Case C - R11 clocking

Case B represents a configuration with equal stator count and different rotor count, while Case C investigates the opposite situation with different stator count and equal rotor count.

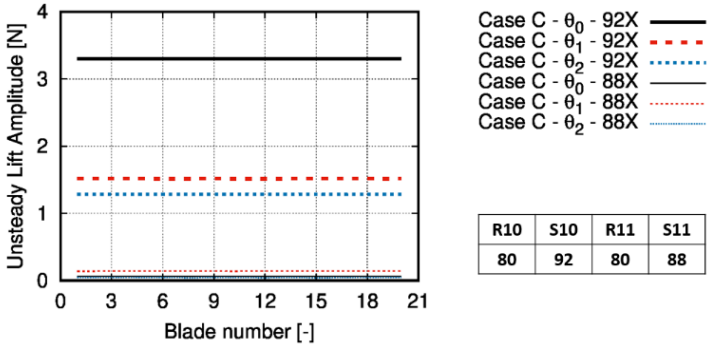

R10	S10	R11	S11
80	92	80	88

Figure 5.39 - Unsteady lift amplitude on R10 with Nc=100%

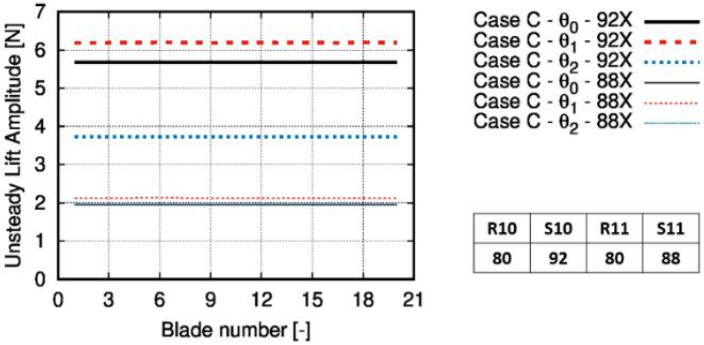

Figure 5.40 - Unsteady lift amplitude on R11 with Nc=100%

In this latter configuration the non-uniform distribution of unsteady lift amplitude is due to different blade count of stator rows. The results discussed in this chapter refer to Nc=100% and investigate the impact of varying the tangential position of R11 that this time is characterized by having the same count of R10. The unsteady lift amplitude on rotor rows show the same trend found in case A, as witnessed by the direct comparison of Figure 5.39 and Figure 5.40 with Figure 5.25 and Figure 5.27 respectively. The unsteady lift amplitude of S10 shows a very weak tangential distortion, hardly visible in Figure 5.41, where the unsteady lift amplitude airfoil-to-airfoil change is very small, despite being composed again of nodal diameters ND=8 (R11-S11) and ND=12 (R10-S10 and S10-R11). This is because the contribution of the upstream running pressure wave with ND=8 generated by the interaction between R11 and S11 is apparently negligible. Nevertheless, the clocking position of R11 changes the unsteady lift amplitude because it modifies the relative phase between R10-S10 and S10-R11 interactions.

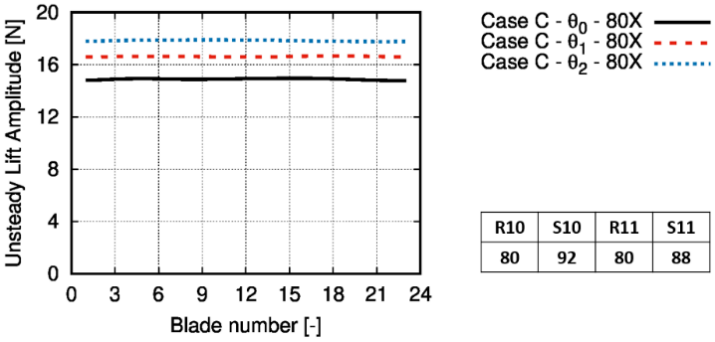

R10	S10	R11	S11
80	92	80	88

Figure 5.41 - Unsteady lift amplitude on S10 with Nc=100%

Figure 5.42 shows the interesting distribution of the unsteady lift amplitude on S11. The different clocking positions have a small impact on the trend, but a relevant effect on the amplitude. This is contrary to what observed on R10, case B, where different clocking positions showed same lift and frequency, but only with a phase shift.

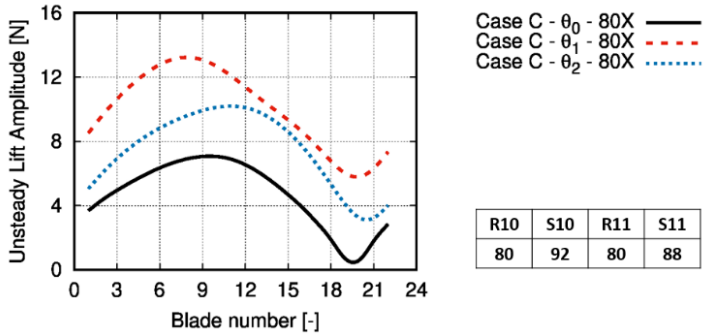

R10	S10	R11	S11
80	92	80	88

Figure 5.42 - Unsteady lift amplitude on S11 with Nc=100%

This interesting effect can be explained by looking at the unsteady pressure distribution on the blade surface (see Figure

5.43 and Figure 5.44 relative to ND=8 and ND=12 respectively).

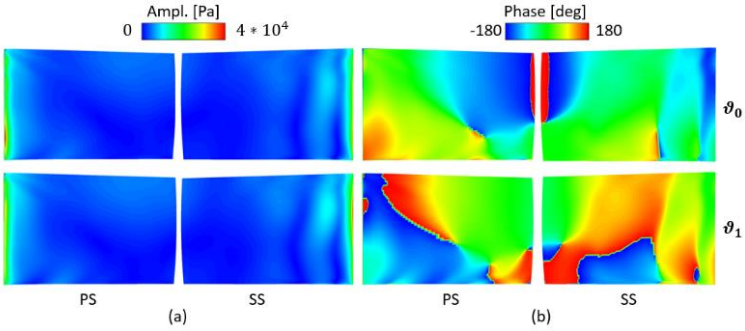

Figure 5.43 - pressure amplitude (a) and phase (b) from time and space decomposition (EO=80X and ND=8) on S11 with Nc=100% with R11 clocking position ϑ_0 (top) and ϑ_1 (bottom)

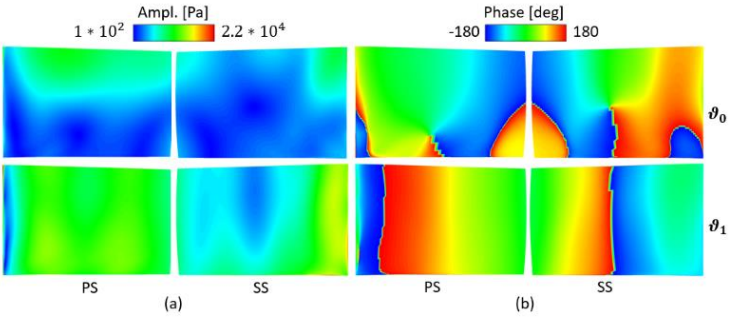

Figure 5.44 - pressure amplitude (a) and phase (b) from time and space decomposition (EO=80X and ND=12) on S11 with Nc=100% with R11 clocking position ϑ_0 (top) and ϑ_1 (bottom)

Figure 5.43 shows that the distribution of ND=8 is very weakly influenced by the clocking position because it is mainly due to R11-S11 interaction (and R10-S11 interaction is negligible). The

phase plot is characterized by a constant phase-shift due to different clocking position of R11 (same behaviour observed in Figure 21). The contribution of ND=12, shown in Figure 5.44, changes in amplitude and phase with clocking because it is composed by the sum of R10-S10 and S10-R11 interactions and again the relative phase varies with the different clocking positions.

The case C results have therefore highlighted that the different relative clocking positions of two consecutive blade rows with the same blade count must be carefully accounted for during the forced response assessment. This has an impact also on the blade in the stationary frame of reference with no common blade count and it affects both classical unsteady interactions and Tyler-Sofrin ones.

5.5.2.5 Case B - S11 clocking

Case B addressed the impact of R10-R11 relative tangential position, although the two rotor rows have different airfoil count. This section starts from the same case B, but it investigates the effect of S11 clocking with S10, that has the same airfoil count. The investigation is carried out at Nc=100%. Figure 5.45 and Figure 5.46 prove that S11 clocking position has a very weak effect on both R10 and S10 unsteady lift amplitude. R10 presents only very slight differences in the pattern distribution due to the variation of the relative phase between S10-R11 and R11-S11 interactions that propagate upstream weakly to R10.

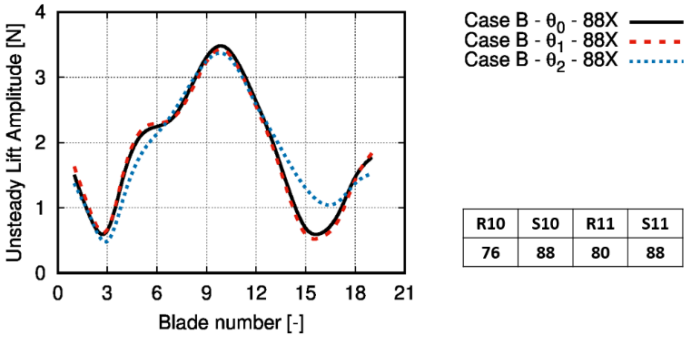

Figure 5.45 - Unsteady lift amplitude on R10 with Nc=100%

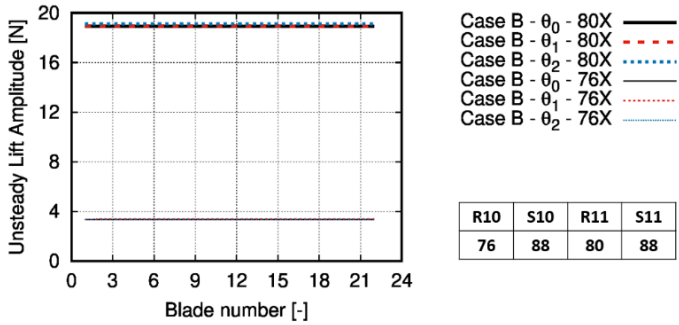

Figure 5.46 - Unsteady lift amplitude on S10 with Nc=100%

S10 does not show relevant variation because, as already seen in previous cases, the upstream running pressure wave due to Tyler-Sofrin interactions between R11 and S11 is negligible with respect to S10-R11 interactions with respect to 80X. Similarly, the 76X driven S10-R11 interaction is as negligible as the R10-S10. As expected, the R11 distribution of unsteady lift amplitude in Figure 5.47 has a trend similar to the one reported in Figure 5.42. The different clocking positions have a slight impact on the trend but a quite relevant effect on the amplitude.

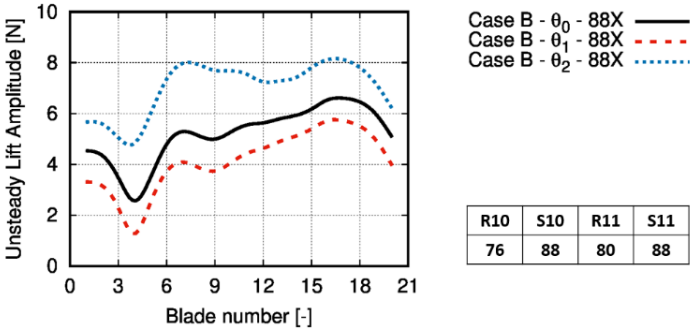

Figure 5.47 - Unsteady lift amplitude on R11 with Nc=100%

The main nodal diameters contributions, 8 and 12, change with the clocking position of S11 (see Figure 5.48 and Figure 5.49). ND=12 shows only slight changes because the R10-S11 interaction is almost negligible with respect to R10-S10 interaction.

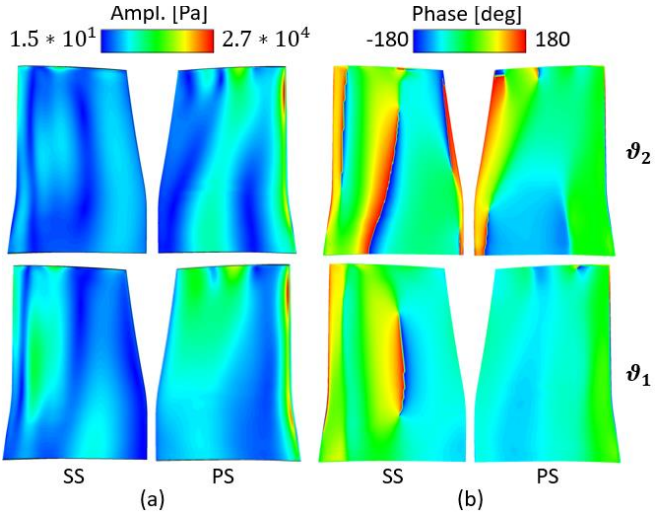

Figure 5.48 - pressure amplitude (a) and phase (b) from time and space decomposition (EO=88X and ND=8) on R11 with Nc=100% with S11 clocking position ϑ_2 (top) and ϑ_1 (bottom)

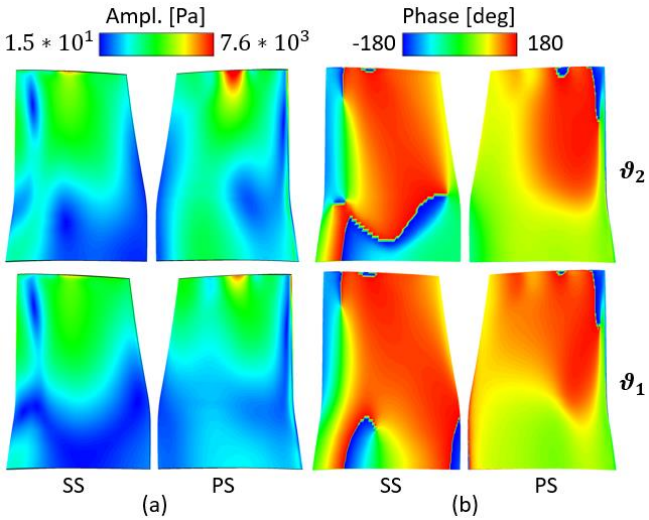

Figure 5.49 - pressure amplitude (a) and phase (b) from time and space decomposition (EO=88X and ND=12) on R11 with Nc=100% with S11 clocking position ϑ_2 (top) and ϑ_1 (bottom)

Finally, to provide a further verification, Figure 5.50 illustrates the unsteady lift amplitude on S11 that depends on the clocking of S11 itself and shows trends similar to case A for the same airfoil row at least for the 80X excitation. Conversely, the ND=8 contribution changes more visibly both in terms of amplitude and phase because it is composed by the interactions S10-R11 and R11-S11 where the relative phase changes with the variation of the S11 tangential position.

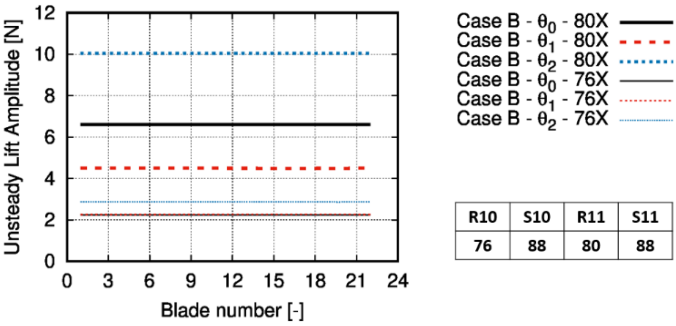

R10	S10	R11	S11
76	88	80	88

Figure 5.50 - Unsteady lift amplitude on S11 with Nc=100%

At the end of this extensive numerical study the following conclusions can be drawn. The case study presented here suggests that clocking effects can be divided into three main categories:

1. **Flat unsteady lift**: This case occurs when the excited blade-row has the same count of the corresponding blade-rows in the same frame of reference so that unsteady forcing generates only waves with common ND (see Figure 5.17).
2. **Modulated unsteady lift with phase shift only**: It occurs when a) the excited blade-row has different count of the corresponding blade-rows in the same frame of reference, b) even in presence of more waves with same ND, the clocking row does not alter the relative phase (see Figure 5.31). In this case clocking has no effect on forced response results.
3. **Modulated unsteady lift with phase and amplitude shift**: This scenario materializes when: a) the excited blade-row has a different count respect to the blade-rows in the same frame of reference; b) the exciting blade-row has the same count to create waves with same ND, c) and the clocking position variation alters

the relative phase of waves with common ND (see Figure 5.42).

The results suggest that clocking impacts the aeromechanics of both rotors and stators. An unsteady forcing that excites a single nodal diameter is affected by the clocking position when it is composed of multiple contributions whose relative phase changes with the clocking position. This latter conclusion is valid for both classical aeromechanical forcing and the ones caused by Tyler-Sofrin interactions.

In summary, equal or different consecutive blade count in same reference frame react differently to clocking and pose both different design challenges and offer different aeromechanics risk mitigation opportunities. In fact, different blade counts produce a larger number of engine orders that can excite the blade, while equal blade count do come with potential clocking issues, that the designer may prevent by avoiding unfortunate clocking positions that may amplify response. Moreover, the Nc=90% and 100% R11 clocking analyses suggest that it may not be possible to identify a unique clocking position that minimizes the unsteady force across the compressor map. Both clocking and operative condition impact the unsteady pressure distributions in terms of amplitudes and phase so that different modes may be triggered across the operating points. An aeromechanic optimum clocking is realistic only for narrow operating ranges (for example a fixed speed gas turbine for power generation) after the most dangerous crossings have been identified.

6 Conclusion

A CFD strategy base on steady and unsteady computations for the aerodynamic and aeromechanic design and verification of axial compressor for gas turbine application has been presented in this PhD thesis. The aim of this work is to significantly increase the accuracy of the numerical predictions while keeping the duration of design cycles acceptable for industrial practice. In fact, this is balanced by the reduction of the number of compressor validation tests that drastically increase design costs and often lead to painful and time-consuming redesigns. The activities have been carried out in the framework of the collaboration between the university research group led by Professor Arnone and the industrial partner Baker Hughes.

The CFD strategy can be briefly summarized in the following steps. The 3D design process starts with steady computations to verify the matching of the stages at the design condition and optimizes other operating conditions with a particular focus to the stall margin zone. The next steps consist in running the unsteady computations on the whole axial compressor with a full-annulus approach. The unsteady runs firstly assess the ADP performance previously derived by steady state results. The next steps consist in the stall margin prediction and forced response analysis. If the stall margin results to be lower than the design specifications, a redesign is performed by steady runs on a single stage with the inlet profile condition taken from time-average quantities extracted from the unsteady computations. This approach allows to redesign the blade based on unsteady

results but using a steady approach that keeps low computational times and costs. Regarding the forced response assessment, the unsteady forcing are extracted from the unsteady computation result and are spatially decomposed in the different contributions with the same frequency, but different circumferential orders. A FEM modal analysis is then performed to predict natural frequencies and mode shape families. The improved use of the Interference diagram allows to evaluate resonance conditions that occurs also at harmonic indices different from the main one. The natural frequencies and mode shape displacements are used to perform aerodynamic damping analyses. Finally, the forced response analysis is computed by means of a dedicated tool based on the modal work theory. The modal work approach ensures extremely short computational times with virtually zero computational cost. If the blade does not satisfy the HCF life assessment and consequently needs a redesign, an unsteady computation on a reduced domain can be performed to update the unsteady pressure perturbation on the blade surface. The reduced computational domain must include all the blade rows that are involved in the generation of the exciting spinning pressure perturbations.

The availability of a reliable data set of a multistage axial compressor that incorporates high-performance features suited for both propulsion and heavy-duty gas turbine was instrumental to validate the CFD strategy. The computational efficiency of the CFD tool allowed to perform multi-stage steady and unsteady computations in a time compatible with design verifications.

The first part of the results focuses on the aerodynamic validation of the steady and unsteady CFD strategy. The simulations proved how the URANS approach is substantially superior to

RANS, as the latter predicted the stall onset around the measured design point, while the former allowed to get much closer to the observed left limit. The comparison with the measured inter-stage stagnation pressure and temperature spanwise profiles confirmed the superiority of the unsteady approach, especially for what concerns the stagnation temperature. Nevertheless, single-stage steady runs performed with inlet conditions extracted from the time-averaged companion multistage URANS analysis show an optimum agreement with the latter one. This result confirms the possibility of a combined use of steady and unsteady simulation for the design iteration. Full multistage URANS may be used to compute a limited number of operating points of interest. These runs provide a set of realistic stage inlet and exit profiles that can be applied to single stage RANS simulations, although the stage geometry modifications should not be large enough to provoke a significant departure from the original inlet profiles.

In the second part, the computational methodology for forced response analysis was successfully applied and validated with the measurements coming from an instrumented rotor blade. The proposed methodology is based on the time-spatial decomposition concept of aerodynamic forcing, inherited by the Tyler-Sofrin theory, that allows to leverage full domain unsteady analysis. The 3D multistage unsteady CFD offers the opportunity to extract the dense and rich spatial harmonic content associated to each Engine Order. It allows to identify possible additional excitation sources with respect to the traditional single stator-rotor unsteady analysis that considers only the contribution of the main interactions. The analysis demonstrated that the spatial content associated to the different time harmonics may be also originated by Tyler-Sofrin acoustic interactions,

usually considered in aeroacoustics analysis only. One of the experimental cases reported in this thesis demonstrates that Tyler-Sofrin acoustic interaction may be strong enough to cause measurable structural response levels. Consequently, an improved use of the interference diagram was proposed to allow the detection of potential additional resonances in the critical design phase knowing the entire forcing spatial content thanks to the proposed decomposition. The results also demonstrated the advantages stemming from a full compressor unsteady CFD simulation that allows capturing all the possible resonances with a forced response coupled CFD/FEA analysis to account for spinning forcing coupled with the corresponding mechanical mode-shapes.

Finally, an extensive numerical study was conducted to evaluate the impact of rotor-rotor and stator-stator clocking position on the forced response results taking advantage of the spatial decomposition theory. The results showed that an unsteady forcing that excites a single nodal diameter is affected by the clocking position when it is composed of multiple contributions whose relative phase changes with the clocking position. Both classical aeromechanical forcing and the ones caused by Tyler-Sofrin interactions are influenced by clocking position. An aeromechanic optimum clocking is realistic only for narrow operating ranges after the most dangerous crossings have been identified.

The steady and unsteady CFD strategy for aerodynamic and aeromechanic design and validation has been validated with a large set of measurement taken from an experimental campaign on an 11-stage industrial axial compressor. The numerical procedure has been proven to be ready and suitable for axial compressor design.

The future work will focus on the development of a single design environment characterized by an integration of the two methods described in the thesis that allows a faster exchange of information between aerodynamic/aeromechanical and mechanical computations.

References

[1] L. H. Smith Jr., "Axial Compressor Aerodesign Evolution at General Electric," *ASME Journal of Turbomachinery,* vol. 124, pp. 321-330, 2002.

[2] C. C. Koch and L. H. Smith, Jr., "Loss Sources and Magnitudes in Axial-Flow Compressors," *ASME Journal of Engineering for Power,* pp. 411-424, July 1976.

[3] A. R. Wadia and B. F. Beacher, "Three-Dimensional Relief in Turbomachinery Blading," *ASME Journal of Turbomachinery,* vol. 112, pp. 587-596, 1990.

[4] M. Righi, V. Pachidis and L. Konozsy, "On the prediction of the reverse flow and rotating stall characteristics of high-speed axial compressors using a three-dimensional trhough flow code," *Aerospace Science and Technology,* 2019.

[5] A. R. Wadia, P. N. Szucs and D. W. Crall, "Inner Workings of Aerodynamic Sweep," *ASME Journal of Turbomachinery,* vol. 120, pp. 671-682, 1998.

[6] W. F. Ng and A. H. Epstein, "Unsteady Losses in Transonic Compressors," *ASME Journal of Engineering fro Gas Turbines and Power,* vol. 107, pp. 345-353, 1985.

[7] C. C. Koch, "Stalling Pressure Rise Capability of Axial Flow Compressor Stages," *ASME Journal of Engineering for Power,* vol. 103, pp. 645-656, 1981.

[8] D. C. Wisler, "Loss Reduction in Axial-Flow Compressors Through Low-Speed Model Testing," *ASME Journal of Engineering for Gas Turbines and Power,* vol. 107, pp. 354-363, 1985.

[9] G. Sovran and E. D. Klomp, Experimentally Determined Optimum Geometries for Rectilinear Diffusers with Rectangualr, Conical or Annular Cross Section, vol. Fluid Mechanics of Internal Flow, Amsterdam: Elsevier Publishing, 1967.

[10] C. Cornelius, T. Biesinger, L. Zori, R. Campregher, P. Galpin and A. Braune, "Efficient Time Resolved Multistage CFD Analysis Applied to Axial Compressors," in *Proceedings of ASME Turbo Expo*, Dusseldorf, Germany, 2014.

[11] L. Cozzi, F. Rubechini, M. Marconcini, A. Arnone, P. Astrua, A. Schneider and A. Silingardi, "Facing the Challenges in CFD Modelling of Multistage Axial Compressors," in *Proceedings of ASME Turbo Expo 2017*, Charlotte, NC, USA.

[12] G. G. Adkins Jr. and L. H. Smith Jr., "Spanwise Mixing in Axial-Flow Turbomachines," *ASME Journal of Engineering for Power,* vol. 104, pp. 97-110, 1982.

[13] L. Cozzi, F. Rubechini, M. Giovannini, M. Marconcini, A. Arnone, A. Schneider and P. Astrua, "Capturting Radial Mixing in Axial Compressors with Computational Fluid Dynamics," *ASME Journal of Turbomachinery,* vol. 141, no. 3, 2019.

[14] M. Hewkin-Smith, G. Pullam, S. D. Grimshaw, E. M. Greitzer and Z. S. Spakowszky, "The Role of Tip Leakage Flow in Spike-Type Rotating Stall Inception," *ASME Journal of Turbomachinery,* vol. 141, 2019.

[15] J. Li, S. Geng, J. Du, H. Zhang e C. Nie, «Circumferentially propagating characteristic dominated by unsteady tip leakage flow in axial flow compressors,» *Aerospace Science and Technology,* vol. 85, pp. 529-543, 2019.

[16] J. V. Taylor and R. J. Miller, "Competing Three-Dimensional Mechanisms in Compressor Flows," *ASME Journal of Turbomachinery,* vol. 139, no. 2, 2017.

[17] J. Leggett, S. Priebe, A. Shabbir, V. Michelassi, R. Sandberg and E. Richardson, "Loss Prediction in an Axial Compressor Cascade at Off-Design Incidences With Free Stream Disturbances Using Large Eddy Simulation," *ASME Journal of Turbomachinery,* vol. 140, no. 7, 2018.

[18] K. Yamada, M. Furukawa, Y. Tamura, S. Saito, A. Matsuoka and K. Nakayama, "Large-Scale Detached-Eddy Simulation Analysis of Stall Inception Process in a Multistage Axial Flow Compressor," *ASME Journal of Turbmachinery,* vol. 139, 2017.

[19] N. Gourdain, "Prediction of the Unsteady Turbulent Flow in an Axial Compressor Stage. Part 1: Comparison of Unsteady RANS and LES with experiments," *Computers & Fluids,* vol. 106, pp. 119-129, 2015.

[20] G. Laskoswski, J. Kopriva, V. Michelassi, S. Shankaran, U. Paliath, R. Bhaskaran, Q. Wang, C. Talnikar, Z.

Wang and F. Jia, "Future Directions of High Fidelity CFD for Aerothermal Turbomchinery Analysis and Design," in *46th AIAA Fluid Dynamics Conference*, Washington, D.C., 2016.

[21] J. D. Denton, "Loss Mechanisms in Turbomachines," in *Proceedings of the ASME 1993 International Gas Turbine and Aeroengine Congress and Exposition*, Cincinnati, Ohio, USA. May 24–27, 1993.

[22] H. Wang, Y. Wu, Y. Wang and S. Deng, "Evolution of the flow instabilities in an axial compressor rotor with large tip clearance: An experimental and URANS study," *Aerospace Science and Technology,* vol. 96, 2020.

[23] Z. Wang, B. Lu, J. Liu and J. Hu, "Numerical simulation of unsteady tip clearance flow in a transonic compressor rotor," *Aerospace Science and Technology,* vol. 72, pp. 193-203, 2018.

[24] N. Gourdain, S. Burguburu, F. Leboeuf and H. Miton, "Numerical simulation of rotating stall in a subsonic compressor," *Aerospace Science and Technology,* vol. 10, pp. 9-18, 2006.

[25] H. Sun, M. Wang, Z. Wang and F. Magagnato, "Numerical investigation of surge prediction in a transonic axial compressor with a hybrid BDF/Harmonic Balance Method," *Aerospace Science and Technology,* vol. 90, pp. 401-409, 2019.

[26] S. Stollenwerk and E. Kuegeler, "Deterministic Stress Modeling for Multistage Compressor Flowfields," in

Proceedings of the ASME Turbo Expo: Power for Land, Sea and Air, San Antonio, TX, USA, 2013.

[27] W. S. Barankievicz e M. D. Hathaway, «Effects of stator indexing on performance in a low speed multistage axial compressor,» in *International Gas Turbine & Aeroengine Congress & Exhibition*, Orlando, FL, 1997.

[28] M. Vahdati, A. I. Sayma, M. Imregun e G. Simpson, «Multibladerow forced response modeling in axial-flow core compressors,» *ASME Journal of Turbomachinery,* vol. 129, pp. 412-420, 2007.

[29] M. Terstegen, C. Sanders, P. Jenschke e H. Shoenenborn, «Rotor-Stator Interactions in a 2.5-Stage Axial Compressor - Part I: Experimental Analysis of Tyler-Sofron Modes,» *ASME Journal of Turbomachinery,* vol. 141, n. October, p. 101002, 2019.

[30] J. M. Tyler e T. G. Sofrin, «Axial flow compressor noise studies,» *SAE Transactions,* vol. 70, pp. 309-332, 1962.

[31] C. Frey, G. Ashcroft, H. P. Kersken e C. Voigt, «A Harmonic balance technique for multistage turbomachinery applications,» in *ASME Turbo Expo*, Dusseldorf, 2014.

[32] C. Sanders, M. Terstegen, P. Jeschke, H. Shoenenborn e J. P. Heners, «Rotor-Stator Interactions in a 2.5-Stage Axial Compressor - Part II: Impact of Aerodynamic Modeling on Forced Response,» *ASME Journal of Turbomachinery,* vol. 141, n. October, p. 101008, 2019.

[33] M. Baumgartner, F. Kameier e J. Hourmouziadis, «Non-Engine Order Blade Vibration in a High Pressure Compressor.,» in *12th International Symposium of Airbreathing Engines*, Melbourne, Australia, 1995.

[34] F. Figaschewsky, A. Kuehhorn e B. Beirow, «Analysis of Mistuned Forced Response in an Axial High-Pressure Compressor Rig with Focus on Tyler-Sofrin Modes,» *The Aeronautical Journal,* vol. 123, n. 1261, pp. 356-377, 2019.

[35] K. L. Gundy-Burlet e D. J. Dorney, «Physics of airfoil clocking in axial compressors,» in *International Gas Turbine & Aeroengine Congress and Exhibition*, Orlando, FL, 1997.

[36] D. J. Dorney, O. P. Sharma e K. L. Gundy-Burlet, «Physics of airfoil clocking in a high-speed axial compressor,» in *International Gas Turbine & Aeroengine Congress & Exhibition*, Stockholm, Sweden, 1989.

[37] M. Y. Layachi e A. Bolcs, «Effect of the axial spacing between rotor and stator with regard to the indexing in an axial compressor,» in *ASME Turbo Expo*, New Orleans, 2001.

[38] A. Arnone, M. Marconcini, A. Scotti Del Greco e E. Spano, «Numerical Investigation of Three-Dimensional Clocking Effects in a Low Pressure Turbine,» *ASME Journal of Turbomachinery,* vol. 126(3), p. 375–384, 2004.

[39] R. Vazquez, D. Torre e A. Serrano, «The effect of airfoil clocking on efficiency and noise of low pressure turbines,»

ASME Journal of Turbomachinery, vol. 136, n. 6, p. 061006, 2014.

[40] P. G. Cizmas e D. J. Dorney, «The influence of clocking on unsteady forces of compressor and turbine blades,» in *ISABE*, Florence, Italy, 1999.

[41] H. Huang, H. T. Yang, G. T. Feng e Z. Wang, «Fully clocking effect in a two-stage compressor,» in *ASME Turbo Expo 2003*, Atlanta, GA, 2003.

[42] G. J. Walker, J. D. Hughes, I. Koehler e W. J. Solomon, «The influence of wake-wake interactions on loss fluctuations of a downstream axial compressor blade row,» *ASME Jounral of Turbomachinery,* vol. 120, n. 4, pp. 695-704, 1997.

[43] F. Chen, Z. Gu, H. Xie e Z. Wang, «Effects of compound-lean stator clocking in a low-speed axial compressor,» *AIAA Journal of Propulsion and Power,* vol. 22, n. 6, pp. 1424-1426, 2006.

[44] H. Jia, G. Xi, L. Mueller, R. Mailach e K. Vogeler, «Unsteady blade loading with clocking in multistage axial compressors, Part 1,» *AIAA Journal of Propulsion and Power,* vol. 26, n. 1, pp. 25-35, 2010.

[45] L. Mueller, R. Mailach, K. Vogeler, H. Jia e G. Xi, «Unsteady blade loading with clocking in multistage axial compressors, Part 2,» *AIAA Journal of proulsion and power,* vol. 26, n. 1, pp. 46-56, 2010.

[46] S. R. Manwaring e D. C. Wisler, «Unsteady aerodynamics and gust response in compressors and turbines,» *ASME Journal ofTurbomachinery,* vol. 115, pp. 724-740, 1993.

[47] S. T. Hsu e A. M. Wo, «Reduction of unsteady blade loading by beneficial use of vortical and potential disturbances in an axial compressor with rotor clocking,» in *International Gas Turbine & Aeroengine Congress & Exhibition*, Orlando, FL, 1997.

[48] L. H. Smith, «Wake dispersion in turbomachines,» *ASME Journal of Basic Engineering,* vol. 88, n. 3, pp. 688-690, 1966.

[49] J. R. Salontay, N. L. Key e R. D. Fulayter, «Investigation of flow physics of vane clocking effects on rotor resonant response,» *AIAA Journal of Propulsion and Power,* vol. 27, n. 5, pp. 1001-1007, 2011.

[50] M. Ricci, R. Pacciani, M. Marconcini, P. Macelloni, S. Cecchi and C. Bettini, "Computational Fluid Dynamics-Based Throughflow Analysis of Transonic Flows in Steam Turbines," *ASME Journal of Turbomachinery,* vol. 141, pp. 111005-7, 2019.

[51] J. F. Simon and O. Léonard, "A Throughflow Analysis Tool Based on the Navier-Stokes Equations," in *Proceedings ETC6*, Lille, France, 2005,Mar. 7–11,pp. 7–11.

[52] D. Pasquale, G. Persico and S. Rebay, "Optimization of Turbomachinery Flow Surfaces Applying a CFD-Based

Throughflow Method," *ASME Journal of Turbomachinery,* vol. 136(3), p. 031013, 2013.

[53] S. Lieblein, F. C. Schwenk and R. L. Broderick, "Diffusion Factor for Estimating Losses and Limiting Blade Loadings in Axial Flow Compressor Blade Elements," NACA RM E53D01, 1953.

[54] S. Lieblein, "Incidence and Deviation-Angle Correlations for Compressor Cascades," *Journal of Basic Engineering,* vol. 82, pp. 575-587, 1960.

[55] B. Zeitschrift, "Das verhalten von tragflügelgittern in axialverdichtern und im windkanal," *BWK Zeitschrift,* vol. 5, no. 10, pp. 333-337, 1953.

[56] N. Cumpsty, Compressor Aerodynamics, Singapore: Addison Wesley Longman Limited, 2004.

[57] C. Freeman, "Effect of tip clearance flow on compressor stability and engine performance," Von Karman Institute for Fluid Dynamics, Lecture Series 1985-0, 1985.

[58] I. Day, "Surge, and 75 Years of Research," *ASME Journal of Turbomachinery,* Vols. 138(1),011001, 2016.

[59] H. Saravanamuttoo, H. Cohen and G. Rogers, Gas Turbine Theory 5th edition, Pearson Education, 2013.

[60] Y. C. Fung, An introduction to the theory of aeroelasticity, Courier Dover Publications, 2008.

[61] T. H. Fransson, "Basic introduction to aeroelasticity," *Lecture series at Von Karman Institute for fluid dynamics,* no. 5:B1–B16,, 1999.

[62] A. R. Collar, "The expanding domain of aeroelasticity," *The Aeronautical Journal,* vol. 50(428), p. 613–636, 1946..

[63] M. F. Platzer and F. O. Carta, Manual on aeroelasticity in axial-flow turbomachines. volume 2. structural dynamics, Technical report, Advisory Group for Aerospace Research and Development Neuilly-sur-Seine (France), 1988..

[64] H. Försching, "Aeroelastic stability of cascades in turbomachinery," *Progress in Aerospace Sciences,* vol. 30(3), p. 213–266, 1994.

[65] T. H. Fransson, Aeroelasticity in axial flow turbomachines, Technical report, Von Karman Institute for Fluid Dynamics, 1999.

[66] W. Ning, S. Moffatt, Y. Li and R. G. Wells, "Blade forced response prediction for industrial gas turbines: Part 2—verification and application," *ASME Turbo Expo 2003, collocated with the 2003 International Joint Power Generation Conference,* no. American Society, pp. 415-422, 2003.

[67] L. S. Lynn and D. Burns, Forced vibration and flutter design methodology, Indianapolis, IN (USA): Technical report, Detroit Diesel, 1988..

[68] S. J. Wildheim, "Excitation of rotationally periodic structures," *Journal of Applied Mechanics,* vol. 46(4), p. 878–882, 1979.

[69] S. J. Wildheim, "Excitation of rotating circumferentially periodic structures," *Journal of Sound and Vibration,* vol. 75(3), p. 397–416, 1981.

[70] L. Pinelli, F. Poli, E. Di Grazia, A. Arnone e D. Torzo, «A Comprehensive Numerical Study of Tone Noise Emissions in a Multistage Cold Flow Rig,» in *19th AIAA/CEAS Aeroacoustics Conference*, Berlin, Germany, 2013.

[71] F. Vanti, Development of an Automatic Procedure Development of an Automatic Procedure Axial Turbomachines, Phd Thesis, University of Florence, 2019.

[72] T. Nicholas and J. R. Zuiker, "On the use of the Goodmandiagram for high cycle fatigue design," *International Journal of Fracture,* Vols. 80(2-3), p. 219–235, 1996.

[73] M. H. Herman Shen, "Reliability assessment of high cycle fatigue design of gas turbine blades using the probabilistic Goodman diagram," *International journal of fatigue,* vol. 21(7), p. 699–708, 1999.

[74] Y. El-Aini, R. DeLaneuville, A. Stoner and V. Capece, "High cycle fatigue of turbomachinery components-industry perspective.," *In 33rd Joint Propulsion Conference and Exhibit,* p. 3365, 1997.

[75] A. Arnone, “Viscous Analysis of Three-Dimensional Rotor Flow Using a Multigrid Method,” *ASME Journal of Turbomachinery,* vol. 116, no. 3, pp. 435-445, 1994.

[76] A. Arnone, "Multigrid Methods for Turbomachinery Navier-Stokes Calculations," in *Solution Techniques for Large--Scale CFD Problems*, 1995.

[77] B. S. Baldwin and H. Lomax, "Thin Layer Approximation and Algebraic Model for Separated Turbulent Flows," *AIAA paper 78--257,* 1978.

[78] D. Degani and L. B. Schiff, "Computation of Turbulent Supersonic Flows Around Pointed Bodies Having Crossflow Separation," *Journal of Computational Physics,* vol. 66, pp. 173-196, 1986.

[79] A. Arnone and R. Pacciani, "IGV-Rotor Interaction Analysis in a Transonic Compressor Using the Navier--Stokes Equations," *ASME Journal of Turbomachinery,* vol. 120, pp. 143-155, 1 1998.

[80] P. R. Spalart and S. R. Allmaras, "A One-equation Turbulence Model for Aerodynamic Flows," *AIAA Paper 92-0439,* 1 1992.

[81] P. R. Spalart and M. Shur, "On the Sensitization of Turbulence Models to Rotation and Curvature," *Aerospace Science and Technology,* vol. 1, pp. 297-302, 1997.

[82] D. C. Wilcox, Turbulence Modeling for CFD, 2nd ed., DCW Ind. Inc., La Cañada, CA, USA, 1998.

[83] F. R. Menter, "Two-Equations Eddy Viscosity Turbulence Models for Engineering Applications," *AIAA J.,* vol. 32, pp. 1598-1605, 8 1994.

[84] D. C. Wilcox, "Formulation of the k-ω Turbulence Model Revisited," *#AIAAJ#,* vol. 46, pp. 2823-2838, 11 2008.

[85] A. Jameson, W. Schmidt and E. Turkel, "Numerical Solutions of the Euler Equations by Finite Volume Methods Using Runge--Kutta Time--Stepping Schemes," *AIAA paper 81--1259,* 1981.

[86] R. H. Ni, "A Multiple-Grid Scheme for Solving the Euler Equations," *AIAA paper 81-1025,* 1981.

[87] D. Holmes and S. Tong, "A Three-Dimensional Euler Solver for Turbomachinery Blade Rows," *ASME J. Eng. Gas Turbines Power,* vol. 117, no. 2, pp. 258-264, 1985.

[88] R. C. Swanson and E. Turkel, "On Central-Difference and Upwind Schemes," *Journal of Computational Physics,* vol. 101, pp. 292-306, 1992.

[89] L. Martinelli and A. Jameson, "Validation of a Multigrid Method for Reynolds Averaged Equations," *AIAA paper 88--0414,* 1988.

[90] R. C. Swanson and E. Turkel, "Artificial Dissipation and Central Difference Schemes for the Euler and Navier--Stokes Equations," *AIAA paper 87--1107--CP,* 1987.

[91] M. Arora and P. L. Roe, "A Well-Behaved TVD Limiter for High-Resolution Calculations of Unsteady Flow,"

Journal of Computational Physics, vol. 132, pp. 3-11, 1997.

[92] A. Arnone, M. S. Liou and L. A. Povinelli, "Integration of Navier-Stokes Equations Using Dual Time Stepping and a Multigrid Method," *AIAA Journal,* vol. 33, pp. 985-990, 6 1995.

[93] A. Lerat, "Une Classe de Schemas aux Differences Implicites Pour les Systemes Hyperboliques de Lois de Conservation," *Comptes Rendus Hebdomadaires des Seances de l'Academic des Sciences, Series A: Sciences Mathematiques,* vol. 288A, 1979.

[94] A. Jameson, "The Evolution of Computational Methods in Aerodynamics," *J. Appl. Mech.,* vol. 50, 1983.

[95] M. Raw, "Robustness of coupled algebraic multigrid for the Navier-Stokes equations.," *In 34th Aerospace sciences meeting and exhibit,* p. 297, 1996.

[96] G. Wittum, "The use of fast solvers in computational fluid dynamics," in *In Proceedings of the Eighth GAMM-Conference on Numerical Methods in Fluid Mechanics*, Springer, pages 574–581, 1990.

[97] M. Giovannini, M. Marconcini, A. Arnone and A. Dominguez, "A Hybrid Parallelization Strategy of a CFD Code for Turbomachinery Applications," in *11th European Turbomachinery Conference, paper ETC2015-188*, Madrid, 2015.

[98] L. Pinelli, F. Poli, J. Bellucci, M. Giovannini and A. Arnone, "Evaluation of fast numerical methods for

turbomachinery blade flutter analysis," in *In 14th International Symposium on Unsteady Aerodynamics, Aeroacoustics and Aeroelasticity of Turbomachines*, 2015.

[99] F. Vanti, L. Pinelli, F. Poli and A. Arnone, "Aeroelastic investigation of turbine blade assemblies: Cluster system and mistuned rows," in *In 12th European Conference on Turbomachinery Fluid Dynamics & Thermodynamics ETC12*, 2017.

[100] F. Poli, A. Arnone, L. Pinelli and C. Schipani, "A timeaccurate 3D method for turbomachinery blade flutter analysis," 2009.

[101] L. Peruzzi, Aeromechanical characterization strategy for high pressure steam turbines, University of Florence: PhD thesis, 2017.

[102] P. Barreca, L. Pinelli, F. Vanti and A. Arnone, Aeroelastic investigation of a transonic compressor rotor with multirow effects, Associazione Termotecnica Italiana: In 73rd Conference of the Italian Thermal Machines Engineering Association (ATI 2018), 2018.

[103] S. Biagiotti, L. Pinelli, F. Poli, F. Vanti and R. Pacciani, "Numerical study of flutter stabilization in low pressure turbine rotor with intentional mistuning," *Energy Procedia,* vol. 148, pp. 98-105, 2018.

[104] F. Vanti, L. Pinelli, A. Agnolucci and A. Arnone, "An integrated numerical procedure for flutter and forced response assessment of turbomachinery blade-rows," in *In*

European Conference on Turbomachinery Fluid dynamics and Thermodynamics, 2019.

[105] L. Pinelli, V. F. A. Arnone, B. B. Beßling and D. Vogt, "Influence of tip shroud modeling on the flutter stability of a low pressure turbine rotor," in *In ASME Turbo Expo 2019: Turbomachinery Technical Conference and Exposition*, American Society of Mechanical Engineers, 2019.

[106] J. L. Steger and R. L. Sorenson, "Automatic Mesh Point Clustering Near a Boundary in Grid Generation with Elliptic Partial Differential Equations," *Journal of Computational Phisycs,* vol. 33, no. 12, pp. 405-410, 1979.

[107] A. P. Saxer and M. B. Giles, "Quasi-Three-Dimensional Nonreflecting Boundary Conditions for Euler Equations Calculations," *Journal of Propulsion and Power,* vol. 2, pp. 263-271, 1993.

[108] C. Burberi, G. Erika, L. Pinelli and M. Marconcini, "Validation of an URANS approach for direct and indirect noise assessment in a high pressure turbine stage," *ATI 2018, Energy Procedia 148,* no. EGYPRO34337, pp. 130-137.

[109] F. O. Carta, "Coupled blade-disk-shroud flutter instabilities in turbojet engine rotors," *Journal of Engineering for Power,* vol. 89(3), p. 419–426, 1967.

[110] C. Burberi, V. Michelassi, A. Scotti del Greco, S. Lorusso, L. Tapinassi, M. Marconcini e R. Pacciani, «Validation of Steady and Unsteady CFD strategies in the Design of

Axial Compressors for Gas Turbine Engines,» *Aerospace Science and Technology,* vol. 107, n. 12, p. 106307, 2020.

[111] «PGT25 Aeroderivative Gas Turbine,» Baker Hughes, [Online]. Available: https://www.bhge.com/pgt25.

[112] L. Pinelli, C. Burberi, M. Ignesti, V. Michelassi, L. Tapinassi, A. Abati e R. Pacciani, «Spatial Decomposition of Aerodynamic Forcing nd Interference Diagram - Part I: Theory and Aeromechanic Validation on an Industrial Axial Compressor,» *Proceedings of ASME Turbo Expo 2021,* Virtual on-line, 2021, GT2021-59514.

[113] C. Burberi, L. Pinelli, M. Ignesti, V. Michelassi, L. Tapinassi, S. Lorusso and M. Marconcini, "Spatial Decomposition of Aerodynamic Forcing and Interference DIagram - Part II: The Effects of Clocking on Aeromechanic Assesment," *Proceedings of ASME Turbo Expo 2021,* Virtual on-line, 2021, GT2021-59511.

[114] H. D. Akolekar, J. Weatheritt, N. Hutchins, R. D. Sandberg, G. Laskowski and V. Michelassi, "Development and Use of Machine-Learnt Algebraic Reynolds Stress Models for Enhanced Prediction of Wake Mixing in Low Pressure Turbines," in *Proceedings of ASME Turbo Expo 2018*, Oslo, Norway, 2018.

[115] L. Cozzi, F. Rubechini, M. Giovannini, M. Marconcini, A. Arnone, A. Schneider and P. Astrua, "Capturing Radial Mixing in Axial Compressors With CFD," in *Proceedings of ASME Turbo Expo 2018: Turbomachinery*

Technical Conference and Exposition, Oslo, Norway, 2018.

[116] L. Cozzi, F. Rubechini, M. Marconcini, A. Arnone, P. Astrua, A. Schneider and A. Silingardi, "Facing the Challenges in CFD Modelling of Multistage Axial Compressors," in *Proceedings of ASME Turbo Expo 2017: Turbomachinery Technical Conference and Exposition*, Charlotte, NC, USA, 2017.

[117] S. Saito, K. Yamada, M. Furukawa, K. Watanabe, A. Matsuoka and N. Niwa, "Flow Structure and Unsteady Behavior of Hub-Corner Separation in a Stator Cascade of a Multi-Stage Transonic Axial Compressor," in *Proceedings of ASME Turbo Expo 2018*, Oslo, Norway, 2018.

[118] J. Weatheritt and R. Sandberg, "A novel evolutionary algorithm applied to algebraic modifications of the RANS stress-strain relationship," *Weatheritt, J., & Sandberg, R. (2016). A novel evolutionary algorithm applied to algebraic modifications of Journal of Computational Physics,* vol. 325, pp. 22-37, 2016.

[119] L. H. Smith Jr., «Axial Compressor Aerodesign Evolution at General Electric,» *ASME Journal of Turbomachinery,* vol. 124, pp. 321-330, 2002.

[120] C. C. Koch e L. H. Smith, Jr., «Loss Sources and Magnitudes in Axial-Flow Compressors,» *ASME Journal of Engineering for Power,* pp. 411-424, July 1976.

[121] A. R. Wadia e B. F. Beacher, «Three-Dimensional Relief in Turbomachinery Blading,» *ASME Journal of Turbomachinery,* vol. 112, pp. 587-596, 1990.

[122] M. Righi, V. Pachidis e L. Konozsy, «On the prediction of the reverse flow and rotating stall characteristics of high-speed axial compressors using a three-dimensional trhough flow code,» *Aerospace Science and Technology,* 2019.

[123] A. R. Wadia, P. N. Szucs e D. W. Crall, «Inner Workings of Aerodynamic Sweep,» *ASME Journal of Turbomachinery,* vol. 120, pp. 671-682, 1998.

[124] W. F. Ng e A. H. Epstein, «Unsteady Losses in Transonic Compressors,» *ASME Journal of Engineering fro Gas Turbines and Power,* vol. 107, pp. 345-353, 1985.

[125] C. C. Koch, «Stalling Pressure Rise Capability of Axial Flow Compressor Stages,» *ASME Journal of Engineering for Power,* vol. 103, pp. 645-656, 1981.

[126] D. C. Wisler, «Loss Reduction in Axial-Flow Compressors Through Low-Speed Model Testing,» *ASME Journal of Engineering for Gas Turbines and Power,* vol. 107, pp. 354-363, 1985.

[127] G. Sovran e E. D. Klomp, Experimentally Determined Optimum Geometries for Rectilinear Diffusers with Rectangualr, Conical or Annular Cross Section, vol. Fluid Mechanics of Internal Flow, Amsterdam: Elsevier Publishing, 1967.

[128] C. Cornelius, T. Biesinger, L. Zori, R. Campregher, P. Galpin e A. Braune, «Efficient Time Resolved Multistage CFD Analysis Applied to Axial Compressors,» in *Proceedings of ASME Turbo Expo*, Dusseldorf, Germany, 2014.

[129] L. Cozzi, F. Rubechini, M. Marconcini, A. Arnone, P. Astrua, A. Schneider e A. Silingardi, «Facing the Challenges in CFD Modelling of Multistage Axial Compressors,» in *Proceedings of ASME Turbo Expo 2017*, Charlotte, NC, USA.

[130] G. G. Adkins Jr. e L. H. Smith Jr., «Spanwise Mixing in Axial-Flow Turbomachines,» *ASME Journal of Engineering for Power,* vol. 104, pp. 97-110, 1982.

[131] L. Cozzi, F. Rubechini, M. Giovannini, M. Marconcini, A. Arnone, A. Schneider e P. Astrua, «Capturting Radial Mixing in Axial Compressors with Computational Fluid Dynamics,» *ASME Journal of Turbomachinery,* vol. 141, n. 3, 2019.

[132] M. Hewkin-Smith, G. Pullam, S. D. Grimshaw, E. M. Greitzer e Z. S. Spakowszky, «The Role of Tip Leakage Flow in Spike-Type Rotating Stall Inception,» *ASME Journal of Turbomachinery,* vol. 141, 2019.

[133] J. V. Taylor e R. J. Miller, «Competing Three-Dimensional Mechanisms in Compressor Flows,» *ASME Journal of Turbomachinery,* vol. 139, n. 2, 2017.

[134] J. Leggett, S. Priebe, A. Shabbir, V. Michelassi, R. Sandberg e E. Richardson, «Loss Prediction in an Axial Compressor Cascade at Off-Design Incidences With Free

Stream Disturbances Using Large Eddy Simulation,» *ASME Journal of Turbomachinery,* vol. 140, n. 7, 2018.

[135] K. Yamada, M. Furukawa, Y. Tamura, S. Saito, A. Matsuoka e K. Nakayama, «Large-Scale Detached-Eddy Simulation Analysis of Stall Inception Process in a Multistage Axial Flow Compressor,» *ASME Journal of Turbmachinery,* vol. 139, 2017.

[136] N. Gourdain, «Prediction of the Unsteady Turbulent Flow in an Axial Compressor Stage. Part 1: Comparison of Unsteady RANS and LES with experiments,» *Computers & Fluids,* vol. 106, pp. 119-129, 2015.

[137] G. Laskoswski, J. Kopriva, V. Michelassi, S. Shankaran, U. Paliath, R. Bhaskaran, Q. Wang, C. Talnikar, Z. Wang e F. Jia, «Future Directions of High Fidelity CFD for Aerothermal Turbomchinery Analysis and Design,» in *46th AIAA Fluid Dynamics Conference*, Washington, D.C., 2016.

[138] J. D. Denton, «Loss Mechanisms in Turbomachines,» in *Proceedings of the ASME 1993 International Gas Turbine and Aeroengine Congress and Exposition*, Cincinnati, Ohio, USA. May 24–27, 1993.

[139] H. Wang, Y. Wu, Y. Wang e S. Deng, «Evolution of the flow instabilities in an axial compressor rotor with large tip clearance: An experimental and URANS study,» *Aerospace Science and Technology,* vol. 96, 2020.

[140] Z. Wang, B. Lu, J. Liu e J. Hu, «Numerical simulation of unsteady tip clearance flow in a transonic compressor

rotor,» *Aerospace Science and Technology,* vol. 72, pp. 193-203, 2018.

[141] N. Gourdain, S. Burguburu, F. Leboeuf e H. Miton, «Numerical simulation of rotating stall in a subsonic compressor,» *Aerospace Science and Technology,* vol. 10, pp. 9-18, 2006.

[142] H. Sun, M. Wang, Z. Wang e F. Magagnato, «Numerical investigation of surge prediction in a transonic axial compressor with a hybrid BDF/Harmonic Balance Method,» *Aerospace Science and Technology,* vol. 90, pp. 401-409, 2019.

[143] S. Stollenwerk e E. Kuegeler, «Deterministic Stress Modeling for Multistage Compressor Flowfields,» in *Proceedings of the ASME Turbo Expo: Power for Land, Sea and Air*, San Antonio, TX, USA, 2013.

[144] A. Brandt, "Multi-Level Adaptive Computations in Fluid Dynamics," *AIAA paper 79-1455,* 1979.

[145] “PGT25 Aeroderivative Gas Turbine,” Baker Hughes, [Online]. Available: https://www.bhge.com/pgt25.

[146] P. Boncinelli, F. Rubechini, A. Arnone, M. Cecconi and C. Cortese, "Real Gas Effects in Turbomachinery Flows: a CFD Model for Fast Computations," *ASME paper 2003--GT--38101,* 2003.

[147] D. Espinal, H. Im and G. Zha, “Full-Annulus Simulation of Nonsynchronous Blade Vibration Excitation of an

Axial Compressor," *ASME Journal of Turbomachinery,* vol. 140, 2018.

[148] R. Pacciani, M. Marconcini and A. Arnone, "Comparison of the AUSM+-up and Other Advection Schemes for Turbomachinery Applications.," *Shock Waves,* vol. 29, no. 5, 2019.

[149] J. K. Ramsey., Nasa aeroelasticity handbook volume 2: design guides part 2, 2006.